THE UNIVERSITY OF CHICAGO

DEVELOPMENT OF FUNCTIONAL METAL-ORGANIC MATERIALS FOR OXYGEN SENSING AND CATALYSIS

A DISSERTATION SUBMITTED TO

THE FACULTY OF THE DIVISION OF THE PHYSICAL SCIENCES

IN CANDIDACY FOR THE DEGREE OF

DOCTOR OF PHILOSOPHY

DEPARTMENT OF CHEMISTRY

BY

RUOYU XU

CHICAGO, ILLINOIS

JUNE 2018

TABLE OF CONTENTS

LIST OF SCHEMES

LIST OF TABLES

LIST OF FIGURES

LIST OF ABBREVIATIONS

^{1}MLCT	singlet metal-to-ligand charge transfer
2D	2-dimensional
3D	3-dimensional
^{3}MLCT	triplet metal-to-ligand charge transfer
A^3	aldehyde-alkyne-amine
AcOH	acetic acid
ATRP	atom-transfer radical polymerization
BET	Brunauer-Emmett-Teller
BINAP	2,2'-bis(diphenylphosphino)-1,1'-binaphthyl
BINOL	1,1'-bi-2-naphthol
BMA	benzyl methacrylate
BTB	benzene 1,3,5-tri(benzoate)
bpdc	biphenyldicarboxylate
bpydc	2,2'-bipyridine-5,5'-dicarboxylic
bpy	2,2'-bipyridine
CLSM	confocal laser scanning microscopy
CPK	Corey-Pauling-Koltun (CPK) model, space filling model

DIC	differential interface contract
DIPEA	diisopropylethylamine
DMA	dimethylacetamide
DMAP	4-dimethylaminopyridine
DMF	dimethylformamide
DLS	dynamic light scattering
DMSO	dimethyl sulfoxide
EBP	ethyl α-bromophenylacetate
ee	enantiomeric excess
EPR	electron paramagnetic resonance
fcu	face-centered cubic unit
GPC	gel permeation chromatography
H_3BPY	4',6'-bis(4-benzoic acid)-(2,2'-bipyridine)-5-carboxylic acid
hcp	hexagonal-close-packed
H_2DBP	5,15-di(p-benzoato)porphyrin
H_2DBP-Pt	platinum-5,15-di(p-benzoato)porphyrin
HPLC	high performance liquid chromatography
H_2QPDC-NH_2	amino-quaterphenyldicarboxylate

HBSS	Hank's Balanced Salt Solution
ICP-MS	inductively coupled plasma mass spectrometry
K_{SV}	Stern-Völmer constant
LC	liquid chromatography
MeCN	acetonitrile
MMA	methyl methacrylate
M-nMOF	a mixed-ligand nMOF constructed from Hf SBU and QPDC-NH_2/DBP-Pt
MOF	metal-organic framework
MOL	metal-organic layer
MS	mass spectroscopy
nMOF	nanoscale metal-organic framework
NMR	nuclear magnetic resonance
OTf	trifluoromethanesulfonate
PDI	polydispersity index
PEBBLES	probes encapsulated by biologically localized embedding
PMT	photomultiplier tube
POM	polyoxometalate
ppy	phenylpyridine

PtNP	platinum nanoparticle
PXRD	powder X-ray diffraction
QY	quantum yield
R^2	goodness-to-fit merit
RITC	Rhodamine-B isothiocyanate
R-nMOF	M-nMOF modified with RITC
R-QPDC	QPDC-NH_2 modified with RITC
r.t., RT	room temperature
salen	N,N'-bis(salicylidene)ethylenediamine
SBU	secondary building unit
SET	single electron transfer
SCE	saturated calomel electrode
*t*BuMA	*t*-butyl methacrylate
TEM	transmission electron microscopy
TFA	trifluoroacetic acid
THF	tetrahydrofuran
TGA	thermogravimetric analysis
TLC	thin-layer chromatography

TON	turnover number
TsCl	4-toluenesulfonyl chloride
UFF	universal force field
UiO	University of Oslo (Universitetet i Oslo)
UV-vis	ultra violet and visible

ABSTRACT

Ruoyu Xu: Development of Functional Metal-Organic Materials for Oxygen Sensing and Catalysis

Under the Direction of Professor Wenbin Lin

Metal-organic frameworks (MOFs) are an emerging class of hybrid molecular materials with extended structures constructed from inorganic metal nodes/ions interconnected with multidentate organic linkers. They have been explored in a broad range of applications owing to their modular nature. However, MOFs suffer from restricted diffusion of substrates and products through relatively small channels. To overcome diffusional limitation, our group recently reduced the thickness of one dimension of MOFs to a monolayer to afford a new class of hybrid materials, metal-organic layers (MOLs). This dissertation focuses on the development of new MOFs and MOLs for sensing and catalytic applications.

The first part (Chapter 1) of this dissertation focuses on rational design of MOFs for oxygen sensing. We developed a novel strategy of using mixed ligands of very different chemical nature to construct functional MOFs. Using this method, we synthesized a phosphorescence/fluorescence dual-emissive nanoscale metal-organic framework (nMOF) as an intracellular oxygen sensor. The nMOF contains a Pt(II)-porphyrin ligand as an O_2-sensitive probe and a Rhodamine-B isothiocyanate (RITC) ligand as an O_2-insensitive reference probe, and exhibits good crystallinity, high stability, and excellent ratiometric luminescence response to O_2 partial pressure. *In vitro* experiments confirmed the applicability of this nMOF as an intracellular O_2 biosensor.

The second part (Chapter 2-4) of the dissertation reports the synthesis of functional MOLs as novel single-site solid catalysts for a variety of organic transformations. MOLs overcome substrate size and diffusion limitations often seen in MOFs owing to their unique monolayer

structures. We demonstrated the superior performance of MOLs over MOFs in many catalytic reactions. In Chapter 2, we incorporated $Ru(bpy)_3^{2+}$ photosensitizer into BPY-MOL via post-synthetic metalation to afford photoactive RuBPY-MOL. RuBPY-MOL exhibits higher efficacy than RuUiO-67 in multicomponent photoreactions such as intramolecular and crossed [2+2] photocyclization of bis(enones) and photocatalytic Meerwein addition reactions. In Chapter 3, we report the synthesis of IrBPY-MOL containing cyclometalated iridium complex. IrBPY-MOL was an efficient catalyst for photopolymerization of methyl methacrylate (MMA), benzyl methacrylate (BnMA) and *tert*-butyl methacrylate (*t*BuMA). The resulting polymers possessed high-number-average molar masses and low polydispersity indices. We also showed that IrBPY-MOL significantly outperformed IrUiO-69 MOF. In Chapter 4, we immobilized enantiopure pybox ligand onto the SBUs of MOLs through ligand exchange. The resultant pybox-MOLs functioned as heterogeneous asymmetric catalysts of A^3-coupling reaction (aldehyde-alkyne-amine) in good yields and high enantioselectivities.

ACKNOWLEDGMENTS

Working as a PhD student at University of Chicago was a wonderful and challenging experience. In all these years, I am fortunate to receive direct or indirect help from a number of people, to whom I am greatly indebted. Without the precious support of these personalities, the completion of this dissertation would have never been possible.

First and foremost, I would like to thank my advisor, Professor Wenbin Lin for his constant direction, support, encouragement and constructive criticism throughout the time of my doctorate study. He is a model to me out there not only for his immense knowledge, creative ideas, and insightful opinions, but also his strong motivation, internal passion, pure love, total devotion to science and rigorous manner of research. I saw on him the hardcore “scientist spirit” which is gradually fading away in modern society, and I am lucky to have such an advisor by my side, providing me the freedom to pursue research topics which interest me, guiding and influencing me through instructive discussions. It is a priceless fortune to me during my doctorate research as well as my future career.

I would like to thank my committee members, Professor Richard Jordan and Professor John Anderson, for the time reviewing my dissertation and the advices on my defense. It is my great honor to present my work before such distinguished scientist.

I would like to thank Dr. Kuangda Lu, for his help and mentoring at the beginning when I joined the lab. I would like to thank Dr. Youfu Wang, Dr. Yuanyuan Zhu, Dr. Xiaopin Duan and Dr. Tasha Drake for the collaborations and beneficial discussions on my dissertation work. I would like to thank Dr. Nathan Thacker, an experience organic synthesis chemist, for his instructions and support in organic synthesis. I would like to thank Dr. Takahiro Sawano, Dr. Kuntel Manna, Dr. Teng Zhang, Dr. Zekai Lin, Dan Micheroni, Pengfei Ji, Guangxu Lan, Kaiyuan Ni, Wenbo Han, Zhe Li for helpful discussions, without which it would have taken me much longer time to overcome some of the difficulties. I would like to thank all Lin group members, past and present, for the support, encouragement and friendship.

Additionally, I would like to thank Professor Luping Yu for the support of the polymerization project, and Dr. Zhengxu Cai for the help with GPC. I would like to thank Prof. John Anderson and his group members for their help and advice on EPR experiments. I would like to thank Dr. Alex Filatov for the help on PXRD, Dr. Antoni Jurkiewicz for the help on NMR, Dr. Qin Chang for the help on MS, Dr. Yimei Wang for the help on TEM and Dr. Qiti Guo for the help with the MRSEC instruments. It is my great honor to work with all these excellent professors, staffs and students.

I would like to express my sincere gratitude to my previous roommates, An Shi, Dr. Yufeng Zhang and Dr. Huihui Chen, who took care of me like families during my struggle with Crohn's disease in 2015. I also would like to thank Dr. Qiti Guo, Dr. Youfu Wang, Dr. Kuangda Lu, Dr. Teng Zhang, Dr. Bozhi Tian, Dr. Yuanwen Jiang and many others who helped me survive this rock bottom of my PhD time. I owed you a great deal. I would like to thank my doctor, Dr. Sakuraba Atsushi, for the upmost care received from him over the past yars.

My sincere thanks also goes to my formal advisor, Prof. Bozhi Tian, for his mentoring at the beginning of my graduate study and continuous care about me. I would also like to thank my "good buddy", Zongan Wang, simply for his accompany and friendship; and Lu Li, my girlfriend, for her understanding, support and love.

Finally, I would like to thank my parents for their unconditional trust, timely encouragement, and endless patience. It was their love and trust that raised me up and encouraged me to move forward and face challenges fearlessly. This work is dedicated to them.

CHAPTER 1. Nanoscale Metal-Organic Frameworks for Ratiometric Oxygen Sensing in Live Cells

1.1 Introduction

Metal-organic frameworks (MOFs), also known as porous coordination polymers or porous coordination networks,[1] are coordination polymers with open framework structures that contain void spaces upon removing trapped solvent or templating molecules.[2] The first coordination polymer dates back to 1700s, when the synthetic pigment commonly known as Prussian Blue was in use, whose structure was later determined by X-ray diffraction to be an infinite Fe(II)-CN-Fe(III) network.[3] Numerous coordination polymers were synthesized in the next two centuries, but the term "metal-organic framework" was introduced by Omar Yaghi in 1995[4] after the pioneering work by Robson and others in 1980's and the synthesis of a number of MOFs in early 1990s.[5-8] Since then, MOFs have received widespread interest and become a topical research area in the chemistry and materials communities over the past twenty years.[9-12] Currently, MOFs refer to porous crystalline materials that are constructed from metal ions or clusters (also known as secondary building blocks, SBUs) and organic bridging ligands to form one-, two-, or three-dimensional structures. The organic linkers mostly based on carboxylates, N-donor groups, or phosphonates, are enormously diverse and have a variety of configurations. The vast number of metal ions/clusters and organic linkers as well as their diverse assemblies have led to more than 20,000 MOFs reported to date.[13]

MOF applications in various fields have been explored, including but not limited to gas storage and separation,[14-18] nonlinear optics,[19-21] ferroelectricity,[22-24] conductivity / semiconductivity,[25-28] magnetism,[29,30] luminescence,[31-33] chemical sensing,[31,34,35] catalysis,[36-39] biomedical imaging,[40-42] photodynamic therapy,[42-44] drug delivery[45-47] and energy storage.[48,49] The wide applications of MOF is owing to their versatility as well as tunability. As a designable and tailorable material, MOFs can be functionalized with a number of strategies including constructing frameworks with functional ligands or metal clusters, postsynthetic exchange of ligands or metal ions,[50-52] postsynthetic modification of organic ligands or metal clusters,[53-55] and embedding useful molecules within the pores, including organometallic molecules[56-58], metal nanoparticles,[13,59,60] enzymes[61-63] and others.[64-66] Despite all these interesting properties, compared with other industrially important materials such as zeolites and organic polymers, MOFs are constructed with relatively labile coordination bonds between metals and ligands, which has restricted MOFs' practical applications in many areas.[67-70] The synthesis of highly stable MOFs is still a challenge.

Among all the MOFs reported to date, zirconium-based MOFs have gained increasing interest since the discovery of UiO (Universitetet i Oslo) MOFs in 2008[71] due to their unprecedented stability, especially hydrothermal stability compared to other reported MOFs.[72-75] UiO MOFs comprise 12-connected Zr-oxo clusters $Zr_6(\mu_3\text{-}O)_4(\mu_3\text{-}OH)_4(CO_2)_{12}$ and adopt very high symmetry space group $Fm\bar{3}m$ (face center cubic, **Figure 1-1a,c**). Due to high charge density and bond polarization, there is a strong affinity between Zr(IV) and carboxylate O atoms. This is in accordance with Pearson's hard/soft acid/base concept.[76] Zr(IV) is considered hard acid and carboxylate is considered hard base, therefore their binding is considered strong. As a result, Zr-oxo cluster-based MOFs exhibit good stability in aqueous media, even in acidic conditions. Due to lanthanide contraction, the size and chemical properties of hafnium and zirconium are very similar. They can form clusters with identical structures[77] and share similar physical and chemical properties. In this chapter, I will describe the synthesis of a Hf-based MOF for *in vitro* oxygen sensing. The Hf MOF is stable enough in biological conditions for the reasons mentioned above.

Most reported M-MOFs (M = Zr/Hf) feature 12-,[71,78,79] 10-,[79] 8-,[80-82] or 6-[83] connected M_6O_8 (M = Zr/Hf) clusters as nodes, coordinated to carboxylate-terminated organic linkers. There are rare reports on Zr_8O_6-cluster based MOFs.[84] Very recently, a new MOF structure comprising linear dicarboxylate linker and condensed "double cluster" $M_{12}(\mu_3\text{-O})_8(\mu_3\text{-OH})_8(\mu_2\text{-OH})_6$ (M=Zr/Hf) was reported (**hcp**, **Fig 1-1b,d**).[85,86] The M_{12} cluster can be viewed as a fusion of two M_6 octahedra via six bridging μ_2-OH groups. The ratiometric sensing nMOFs in this chapter adopt this structure.

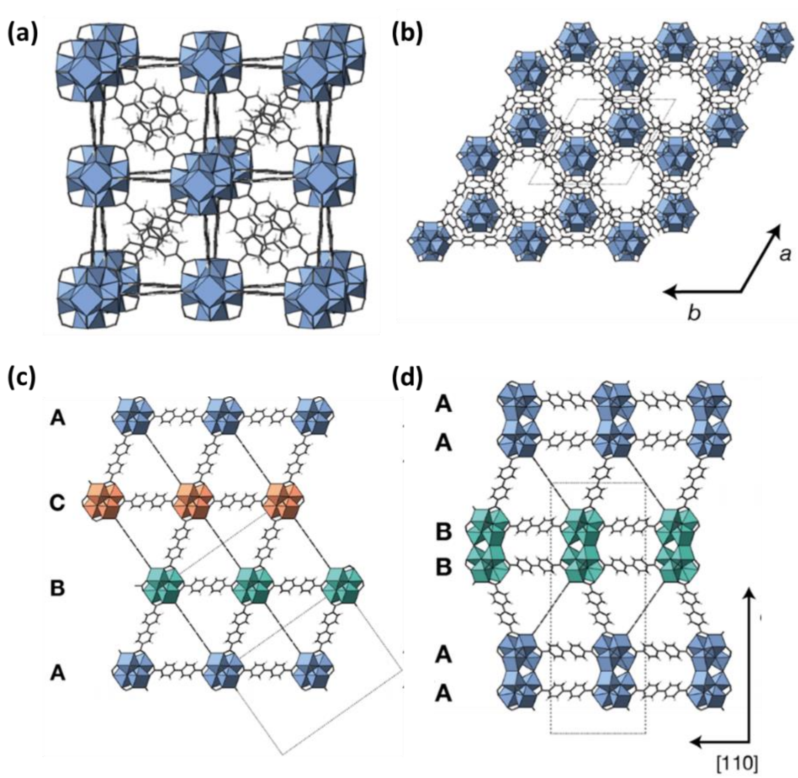

Figure 1-1. Crystal structure of **fcu** UiO-67 and **hcp** UiO-67. **(a) fcu** UiO-67 viewed along the [001] direction. **(b) hcp** UiO-67 viewed along the [001] direction. **(c) fcu** UiO-67 viewed along the [10$\bar{1}$] direction highlighting the "ABC" stacking sequence. **(d) hcp** UiO-67 viewed along the [100] direction, highlighting the "ABBA" stacking sequence. Adapted with permission *from J. Am. Chem. Soc*, **2017**, *139*, 5397-5404. Copyright 2017 American Chemical Society.

Nanoscale MOFs (nMOF) refer to MOFs with dimensions reduced down to nanometer scales. Their sizes can be tuned during solvothermal synthesis by carefully controlling temperature, concentration, solvent components, time and other factors to be compatible with intended biological applications. They have recently been used for small molecule sensing[87-89] and biomedical imaging.[41,90-93] nMOFs exhibit several characteristics that make them ideal nanomaterials for biological and biomedical applications. First, nMOFs have good crystallinity and structural tunability, which allow synthetic elaborations for specific applications. Second, nMOFs are highly porous, which allows them to accommodate high loadings of imaging/therapeutic agents, to quickly transport small molecules (i.e., drugs, analytes), and to prevent dye self-quenching. Third, nMOFs do not suffer from agent leaching due to covalent bonding. Fourth, nMOFs are intrinsically biodegradable in the long term due to their relatively labile metal−ligand bonds.[94] For example, we have recently used a fluorescent nMOF for real-time intracellular pH sensing[90] and a porphyrin-based nMOF in photodynamic therapy[43].

Oxygen (O_2) is a vital component in aerobic respiration that provides metabolic energy to cells. Hypoxia - a reduction in normal levels of O_2 - is related to various diseases,[95] including vascular disease, pulmonary disease, and cancer.[96] For instance, sustained hypoxia in a growing tumor can result in a more aggressive phenotype.[97] Monitoring and quantifying O_2 levels in living cells are thus of great importance for cancer diagnosis, tumor pathophysiology assessment, and evaluation of the therapeutic effects of anticancer treatments. O_2 tension can be detected and measured by several methods, including polarographic O_2 needle electrodes,[98] immunohistochemical staining,[99] positron emission tomography imaging,[100] magnetic resonance imaging,[101,102] and photoluminescence imaging.[103-108] Because of their high sensitivity and outstanding spatial resolution, photoluminescence-based techniques provide particularly powerful tools for sensing O_2 in live cells. Ratiometric sensing, which uses an O_2-insensitive reference and an O_2-sensitive probe to measure emission ratios at two different wavelengths, can compensate for signal changes caused by disturbances from the external environment, such as light scattering and fluctuations in the excitation source,[109] allowing for accurate measurements of O_2 concentrations. Since Kopelman and co-workers first developed PEBBLEs (probes encapsulated by biologically localized embedding) containing a cyanine dye standard and a Pt-porphyrin phosphor for ratiometric O_2 sensing,[110] a number of polymeric nanoparticles,[105,107] silica gels,[111] and quantum dots[112] have emerged as promising ratiometric O_2 sensors.

In this chapter, I will report our efforts on the design of a ratiometric sensing nMOF (R-nMOF), which bears both O_2-independent and -sensitive ligands, and thus serves as an excellent ratiometric O_2 sensor. The nMOF skeleton was constructed from Hf_{12} clusters and a mixed ligand of Pt-5,15-di(p-benzoato)porphyrin (H_2DBP-Pt), which emits bright phosphorescence and is O_2-sensitive, and amino-quaterphenyldicarboxylate (H_2QPDC-NH_2), which can be readily conjugated with fluorescent Rhodamine-B isothiocyanate (RITC) to emit at a different wavelength in an O_2-independent manner. R-nMOF showed a broad response range and good detection accuracy as a ratiometric oxygen sensor in live cells.

1.2. Results and Discussion

1.2.1. Synthesis and Characterization of M-nMOF and R-nMOF

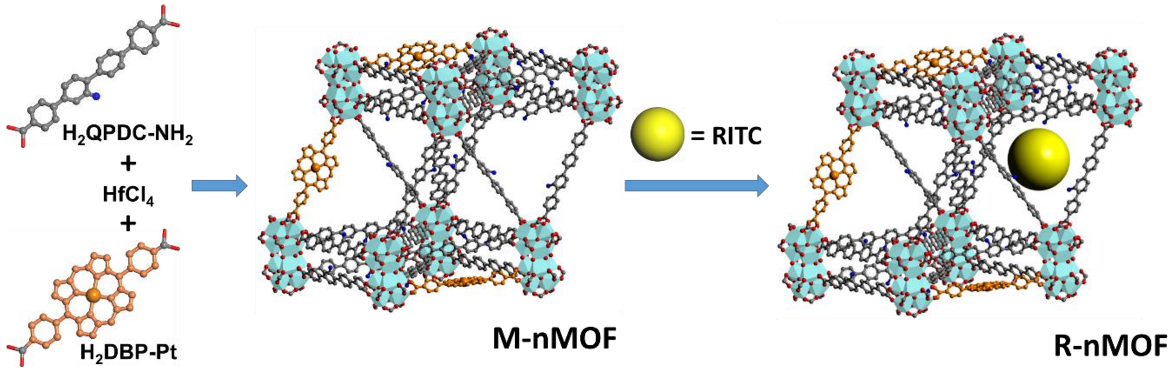

Figure 1-2. Synthesis of mixed-ligand M-nMOF and its postsynthetic modification to afford R-nMOF.

The strategy to construct R-nMOF is shown in **Figure 1-2**. Amino-quaterphenyldicarboxylic acid ($H_2QPDC-NH_2$) and Pt(II)-5,15-di(p-benzoato)porphyrin (H_2DBP-Pt) are similar in length so they can form mixed ligand MOFs. First, they were mixed with $HfCl_4$ in DMF under solvothermal conditions to afford the mixed-ligand MOF (M-nMOF), which was then reacted with Rhodmamine-isothiocyanate (RITC) by forming the thiourea linkage between -NH_2 and –NCS. Different feeding of RITC can result in R-nMOF with different Rhodamine loading, R-nMOF-1 and R-nMOF-2, with the loading ratio 0.6 mol% and 1.6 mol%, respectively (see Methods and Experimental Details). The conjugation of RITC to the ligand ($H_2QPDC-NH_2$) in R-nMOF was confirmed by mass spectrometry. RITC-attached ligands (R-QPDC, exact mass = 909.2) were observed as shown in **Figure 1-3**.

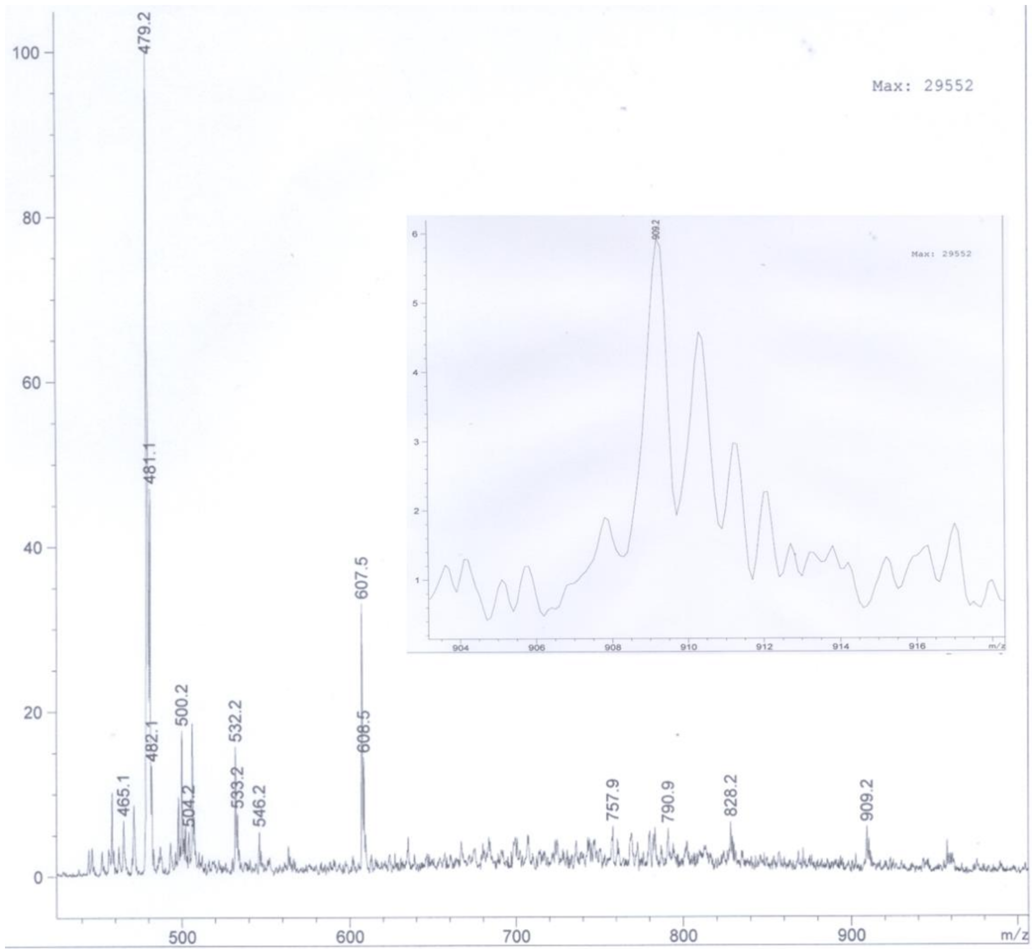

Figure 1-3. Mass spectrum of digested R-nMOF. R-nMOF was digested with HF in methanol. The sample was delivered with methanol. Reprinted with permission from *J. Am. Chem. Soc.*, **2016**, *138*, 2158–2164. Copyright 2016 American Chemical Society.

Powder X-ray diffraction (PXRD) and transmission electron microscopy (TEM) were utilized to confirm the structure and morphology of M-nMOF and R-nMOF. TEM revealed hexagonal plate morphology of M-nMOF with a diameter of ∼200 nm and a thickness of ∼30 nm (**Figure 1-4b**). PXRD, high-resolution TEM, and fast Fourier transform patterns showed that M-nMOF displayed good crystallinity (**Figures 1-4a, 4c**). The distance between adjacent SBUs was measured to be ~2.26 nm by TEM (**Figure 1-4c**), consistent with the distance of 2.18 nm calculated from the PXRD data. TEM images and PXRD patterns also showed that R-nMOF retained the plate-like morphology and the crystallinity of M-nMOF (**Figure 1-4a, 4d**). R-nMOF structure was reported in a recent paper,[86] comprising $Hf_{12}(\mu_3\text{-}O)_8(\mu_3\text{-}OH)_8(\mu_2\text{-}OH)_6$ SBUs and **hcp** topology (**Figure 1-4b,d**).

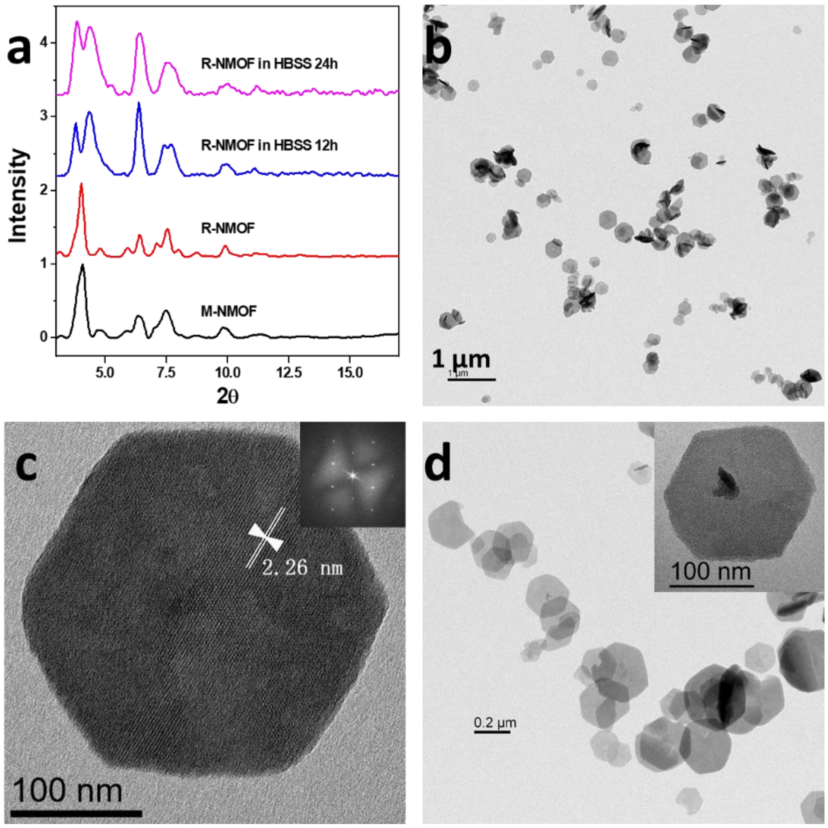

Figure 1-4. Structure and morphology of mixed ligand M-nMOF and R-nMOF. (a) PXRD patterns of M-nMOF, as-synthesized R-nMOF and R-nMOF after incubation in HBSS for 12 h and 24 h. (b) TEM, and (c) high-resolution TEM (inset: fast Fourier transform patterns) of M-nMOF. (d) TEM images of R-nMOF. Reprinted with permission from *J. Am. Chem. Soc.*, **2016**, *138*, 2158–2164. Copyright 2016 American Chemical Society.

The particle sizes of M-nMOF and R-nMOF were determined by dynamic light scattering (DLS, **Figure 1-5, 1-6**). The size of R-nMOF is slightly larger than the M-nMOF.

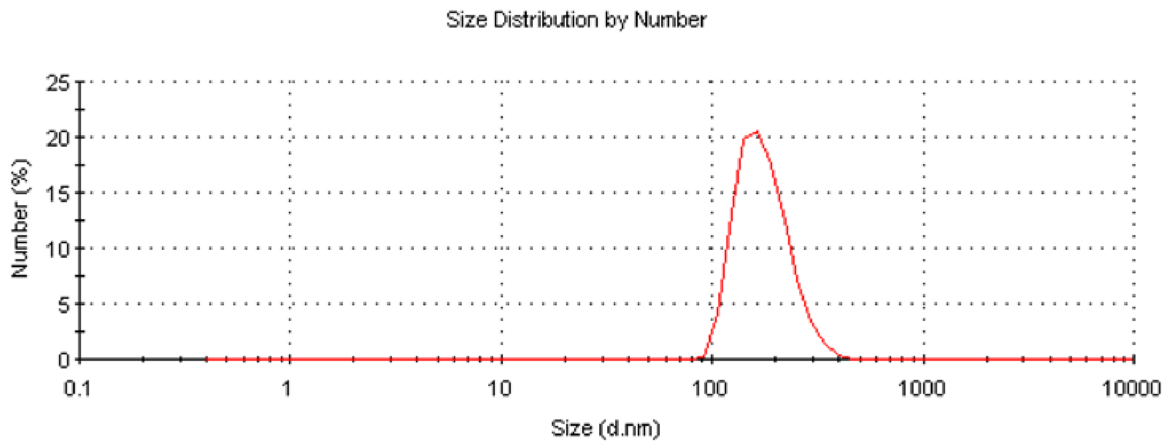

Figure 1-5. DLS measurement showing the particle size of M-nMOF. The average diameter of M-nMOF is 177.8 nm with PDI = 0.064. Reprinted with permission from *J. Am. Chem. Soc.*, **2016**, *138*, 2158–2164. Copyright 2016 American Chemical Society.

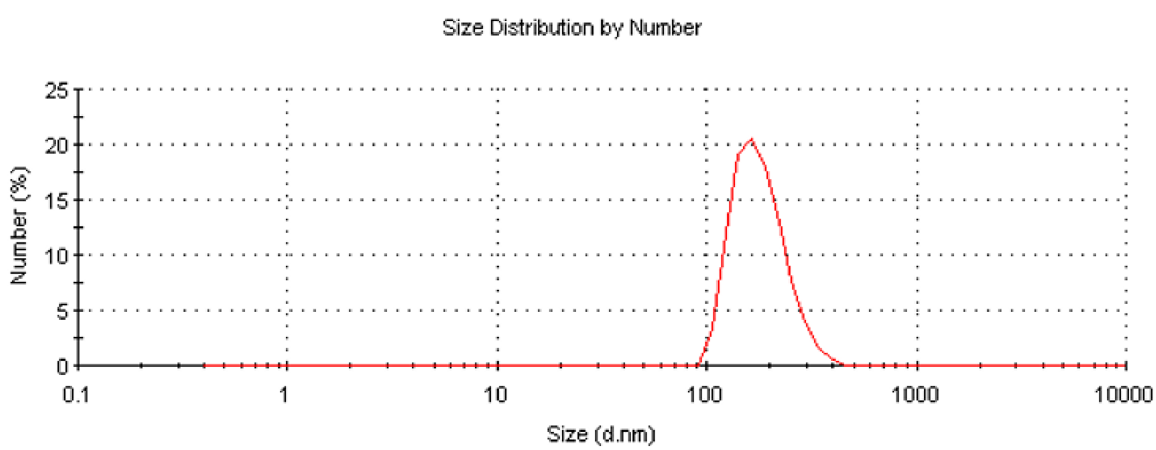

Figure 1-6. DLS measurement showing the particle size of R-nMOF. The average diameter of R-nMOF is 181.8 nm with PDI = 0.079. Reprinted with permission from *J. Am. Chem. Soc.*, **2016**, *138*, 2158–2164. Copyright 2016 American Chemical Society.

Dye release assay was performed by incubating R-nMOF in Hank's Balanced Salt Solution (HBSS) for 24 h. The H_2DBP-Pt and Rhodamine-B released from R-NMOF in HBSS was detected by UV-vis spectra of the supernatant (**Figure 1-7**). The result showed negligible dye release after incubation in HBSS for 24h.

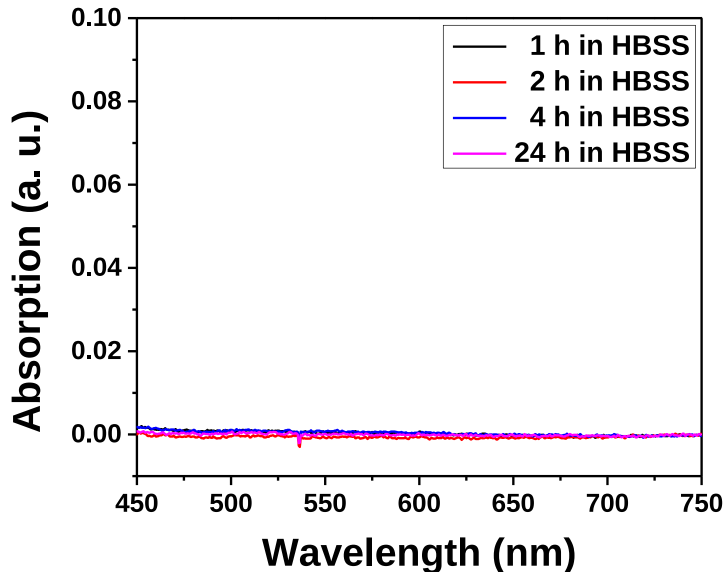

Figure 1-7. Release profile of H_2DBP-Pt and Rhodamine B from R-nMOF in HBSS after different incubation times. Reprinted with permission from *J. Am. Chem. Soc.*, **2016**, *138*, 2158–2164. Copyright 2016 American Chemical Society.

To test the structure stability in HBSS, R-nMOF was incubated in HBSS at room temperature for 1 h, 4 h, and 24 h. The crystallinity and morphology of HBSS-treated R-nMOF was measured by PXRD and TEM. After 24 h incubation, the first peak with highest intensity at ~4^{o} in the PXRD pattern was split into two peaks (**Figure 1-4a**), which likely arises from minor structure distortion or defects during incubation. TEM imaging indicated the preservation of lattice fringes (**Figure 1-8**, **1-9**). These results suggest adequate stability for oxygen sensing in the media.

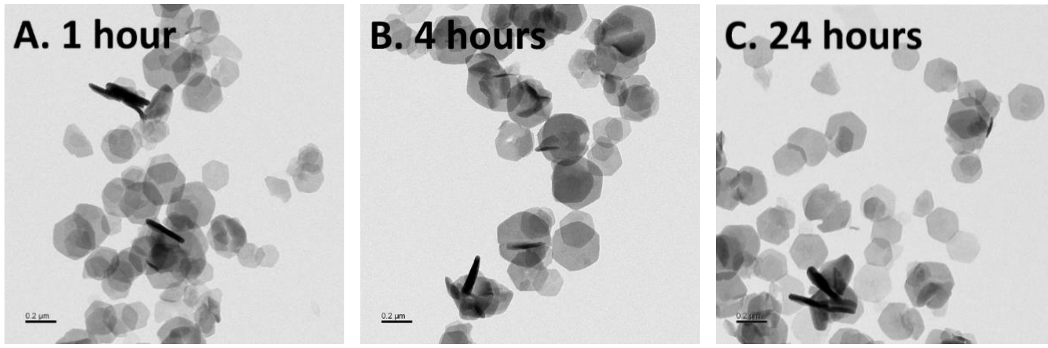

Figure 1-8. TEM images of R-nMOF after incubation in HBSS for 1 h, 4 h, and 24 h. Reprinted with permission from *J. Am. Chem. Soc.*, **2016**, *138*, 2158–2164. Copyright 2016 American Chemical Society.

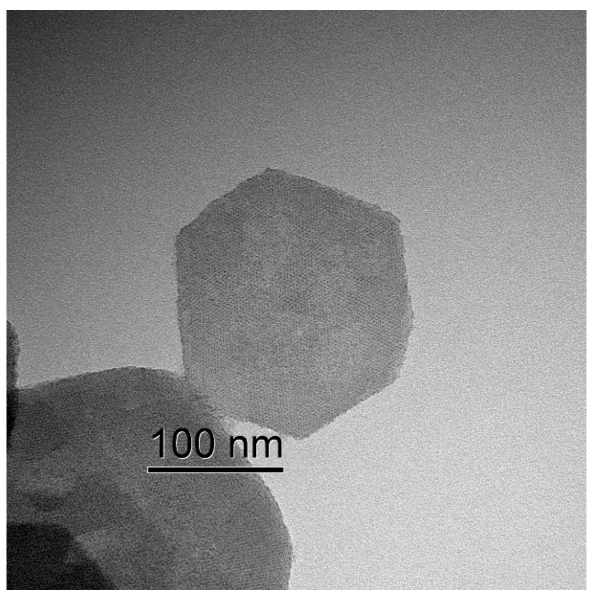

Figure 1-9. High-resolution TEM image of R-nMOF after incubation in HBSS for 24 h. Reprinted with permission from *J. Am. Chem. Soc.*, **2016**, *138*, 2158–2164. Copyright 2016 American Chemical Society.

1.2.2. Photophysics of M-nMOF and R-nMOF

The UV-vis absorption spectrum (UV-2401PC, Shimadzu, Japan) of M-nMOF is shown in **Figure 1-10**. The two characteristic Q-bands of DBP-Pt indicated that there is negligible platinum leaching during the growth of M-nMOF.

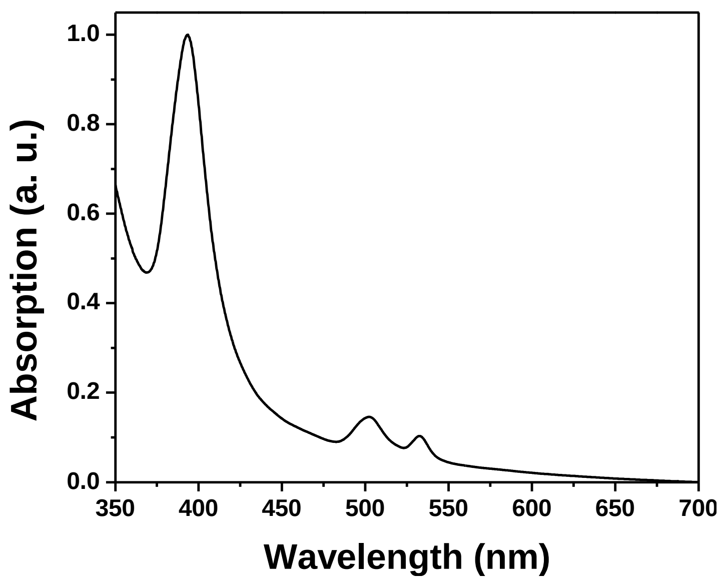

Figure 1-10. UV-vis absorption spectrum of M-nMOF in DMF. Reprinted with permission from *J. Am. Chem. Soc.*, **2016**, *138*, 2158–2164. Copyright 2016 American Chemical Society.

Inductively coupled plasma‒mass spectrometry (ICP-MS, Agilent 7700X) was used to determine Hf and Pt concentration of digested R-nMOF samples. We used UV-vis spectroscopy to quantify Rhodamine-B loading in R-nMOF. The UV-vis spectra of RITC under different concentrations and the standard calibration curve were shown in **Figure 1-11.** We chose the absorption peak of Rhodamine-B-NCS (566 nm) to quantify the loadings of Rhodamine-B.

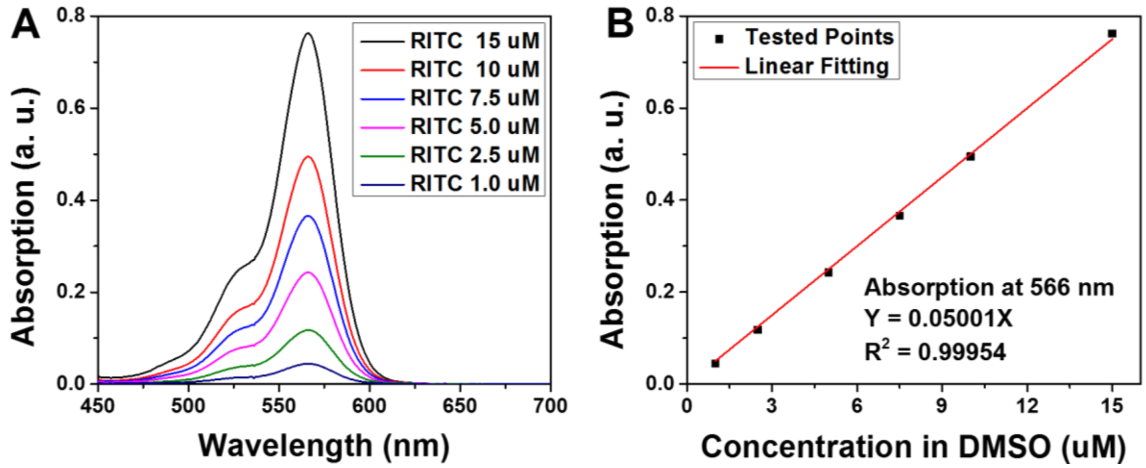

Figure 1-11. (A) UV-vis absorption spectra of RITC at different concentrations in DMSO and (B) the relationship between the absorption at 566 nm and the concentration. Reprinted with permission from *J. Am. Chem. Soc.*, **2016**, *138*, 2158–2164. Copyright 2016 American Chemical Society.

150 μg R-nMOF-1 suspension in 1.5 mL DMSO was digested by adding 4 μL HF. The UV-vis absorption of digested R-NMOF-1 in DMSO was presented as **Figure 1-12**. The loadings of RITC in R-nMOF-1 was determined to be 0.6 mol%. Similarly, RITC loading in R-nMOF-2 was 1.6 mol%.

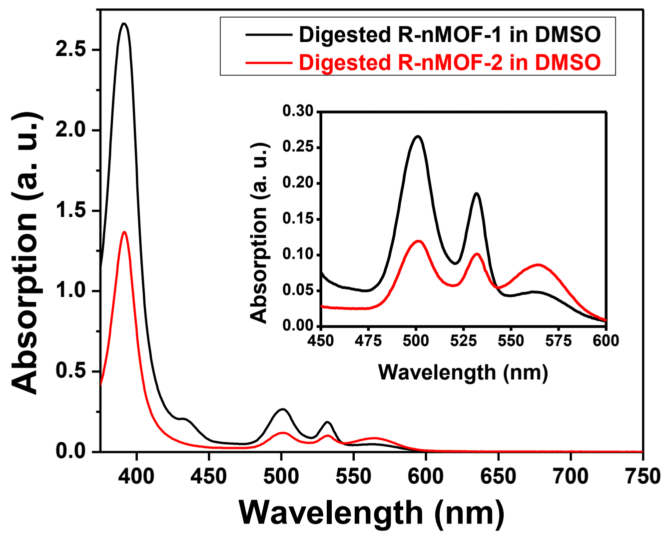

Figure 1-12. Absorption spectra of digested R-nMOF in DMSO. Reprinted with permission from *J. Am. Chem. Soc.*, **2016**, *138*, 2158–2164. Copyright 2016 American Chemical Society.

The UV-vis spectra of H_2DBP-Pt and RITC were obtained in DMSO on a spectrometer and shown in **Figure 1-13**. The emissions of H_2DBP-Pt and RITC were measured in MeOH on a fluorimeter (RF-5301PC) with excitations of 391 nm and 514 nm, respectively.

Pt-porphyrin itself is a bright phosphorescent dye with a long-lived triplet state at ambient temperature, and its phosphorescence intensity is highly dependent on O_2 concentration, making it an ideal choice as an O_2-sensitive probe in ratiometric O_2 sensing.[105-107,110] From **Figure 1-13**, we see a few advantages of selecting Rhodamine-B as a reference dye: (1) Absorption of Rhodamine-B and H_2DBP-Pt at 500-540 nm allows for the simultaneous excitation of both dyes; (2) The non-overlap of Rhodamine-B fluorescence (570 nm) and H_2DBP-Pt phosphorescence (630 nm) facilitates ratiometric luminescence quantifications; (3) The negligible overlap between H_2DBP-Pt emission and Rhodamine-B absorption indicates minimal energy transfer from H_2DBP-

Pt to Rhodamine-B; (4) Emissions of both dyes at relatively long wavelengths (> 570 nm) minimize background autofluorescence from live cells; and (5) The pH-independent fluorescence of Rhodamine-B at pH > 6 prevents disturbance due to cellular pH changes.[113]

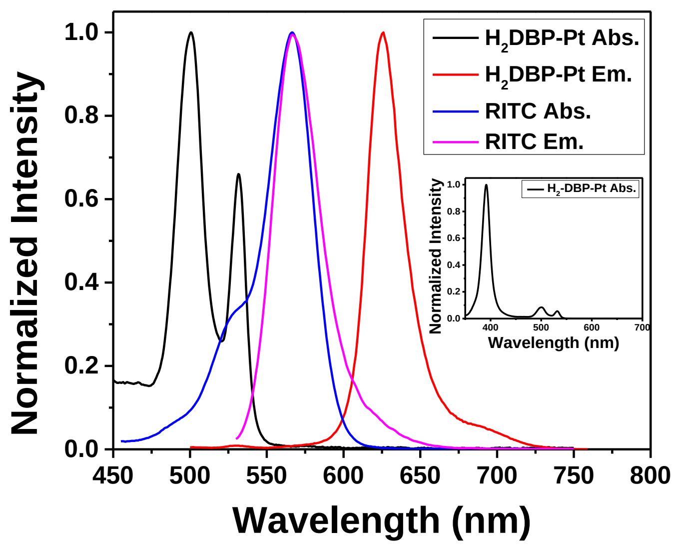

Figure 1-13. Absorption (in DMSO) and emission (in MeOH) spectra of H_2DBP-Pt and RITC. Reprinted with permission from *J. Am. Chem. Soc.*, **2016**, *138*, 2158–2164. Copyright 2016 American Chemical Society.

The lack of energy transfer from H_2DBP-Pt to Rhodamine-B was also confirmed by the presence of only characteristic H_2DBP-Pt phosphorescence, but not RITC fluorescence upon exciting R-nMOF at 391 nm (corresponding to H_2DBP-Pt Soret band, **Figure 1-14**). These results validated ratiometric quantification using a single excitation and simultaneous detection of RITC fluorescence and H_2DBP-Pt phosphorescence.

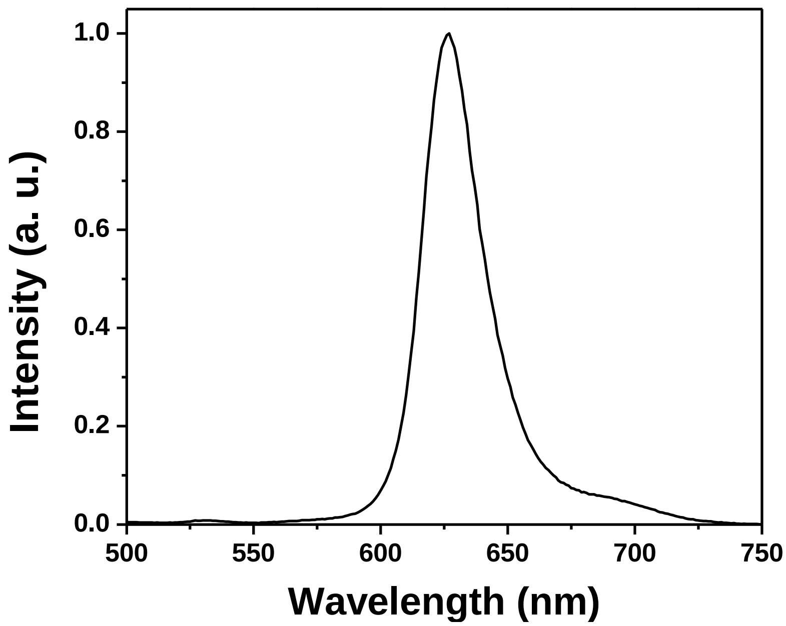

Figure 1-14. The emission of R-nMOF-1 in MeOH (excited at 391 nm). Reprinted with permission from *J. Am. Chem. Soc.*, **2016**, *138*, 2158–2164. Copyright 2016 American Chemical Society.

Ratiometric sensing was first carried out using R-nMOF-1 by fluorimetry with a 514 nm excitation light source in order to match the laser in confocal laser scanning microscopy (CLSM). Under nitrogen-saturated atmosphere (pO_2 = 0 mmHg), R-nMOF-1 showed a strong emission at 630 nm from DBP-Pt and a weak emission at 570 nm attributed to RITC (**Figure 1-15a**). As pO_2 gradually increased to aerated atmosphere (pO_2 = 160 mmHg), the RITC fluorescence remained unchanged, while the DBP-Pt phosphorescence decreased significantly as expected. We quantitatively analyzed oxygen quenching by fitting the data to the Stern-Völmer equation, [114,115]

$$\frac{{R_I}^0}{R_I} = 1 + K_{SV} p_{O_2} \qquad (1\text{-}1)$$

where K_{SV} is the Stern-Völmer constant, and $R_I^0 = I_P^0/I_F^0$ and $R_I = I_P/I_F$ are the ratio of phosphorescence intensity to fluorescence intensity in the absence and presence of oxygen, respectively. R_I^0/R_I showed a good linear relationship with respect to pO_2 up to 80 mmHg (**Figure**

1-15b). Beyond this point, the ratio deviated from the Stern-Völmer plot. Such a deviation was also observed in previous reports[116,117] and is probably related to the complicated dynamics involved in the MOF structure. Fortunately, pO_2 in biological tissues is typical below 70 mmHg (except in arterial blood).[118] Within this range, the intensity ratio fitted well to the Stern-Völmer equation with K_{SV} = 0.015 mmHg^{-1}.

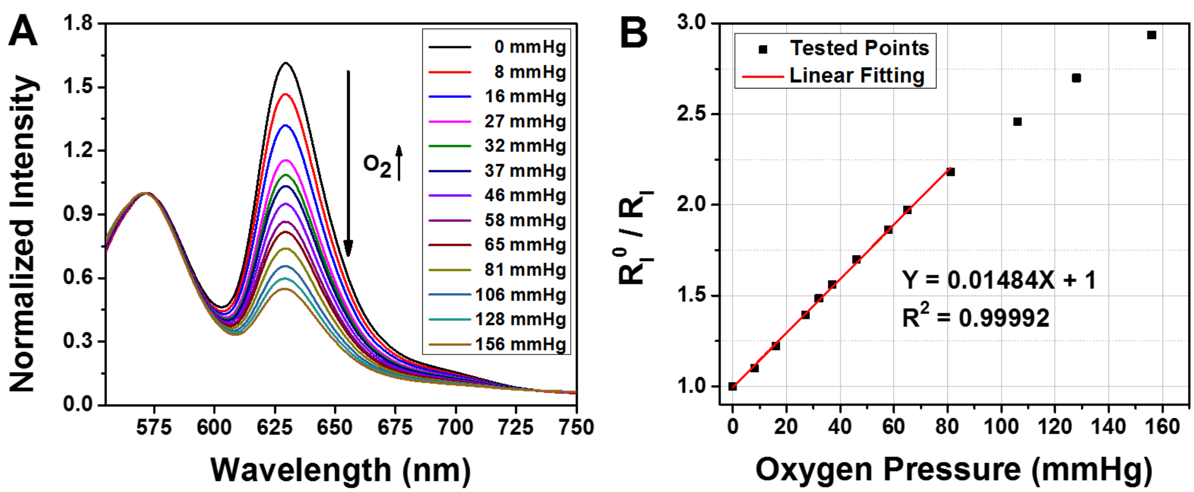

Figure 1-15. (A) Luminescence spectra of R-nMOF-1 under different oxygen partial pressures and (B) R_I^0/R_I as function of pO_2 ranging from 0 mmHg to 160 mmHg. Reprinted with permission from *J. Am. Chem. Soc.*, **2016**, *138*, 2158–2164. Copyright 2016 American Chemical Society.

We also conducted the oxygen quenching assay by fluorimetry with R-nMOF-2 (**Figure 1-16**). It is noteworthy that when RITC loading is high in R-nMOF-2, the Rhodamine-B fluorescence peak has non-negligible overlap with DBP-Pt phosphorescence peak, so R_I^0/R_I will deviate from Stern-Völmer relation (**Figure 1-16b** is different from **Figure 1-15b**). This spectral overlap may also contribute to the non-linear part of **Figure 1-15b** under high oxygen pressure regime (80-160 mmHg range).

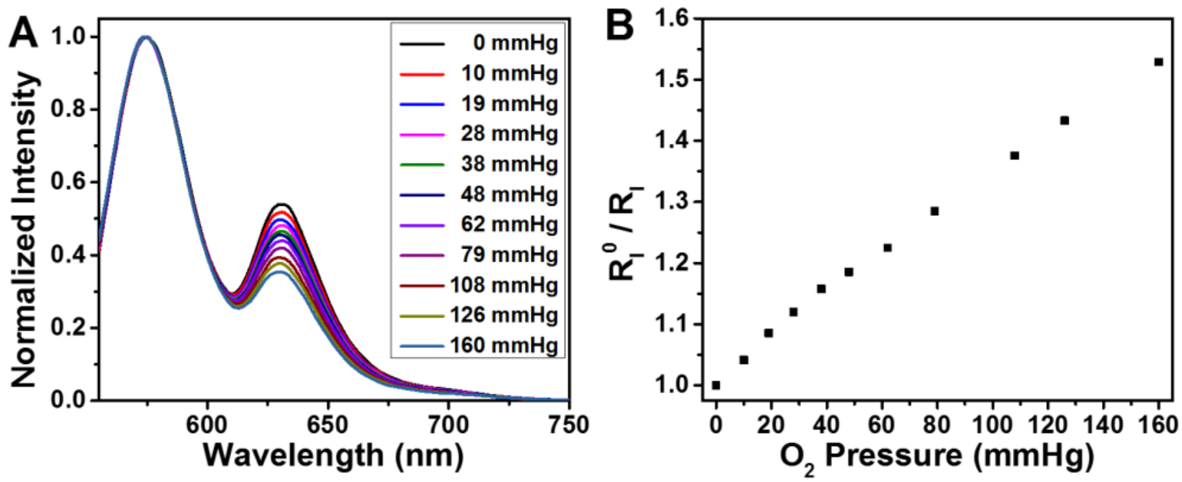

Figure 1-16. (A) Luminescence spectra of R-nMOF-2 under different oxygen partial pressures and (B) R_I^0/R_I as function of pO_2 ranging from 0 mmHg to 160 mmHg. Reprinted with permission from *J. Am. Chem. Soc.*, **2016**, *138*, 2158–2164. Copyright 2016 American Chemical Society.

To further confirm the validity of ratiometric measurements using R-nMOF, the phosphorescence lifetime of R-nMOF-1 in HBSS buffer was measured under different pO_2 (**Figure 1-17a**). The data were fitted by bi-exponential decay. The amplitude weighted lifetime τ (28.1 μs) in a deoxygenated (0 mmHg) atmosphere steadily decreased as pO_2 increased and reached 7.54 μs in an aerated atmosphere (160 mmHg). The lifetime was fitted according to equation **1-2** (**Figure 1-17b**):

$$\frac{\tau^0}{\tau} = 1 + K_{SV} p_{O_2} \tag{1-2}$$

where τ^0 and τ are weighted lifetimes in the absence and presence of oxygen, respectively. The obtained $K_{SV} = 0.017\ mmHg^{-1}$ is similar to the ratiometric measurement result, which indicates negligible static quenching of R-nMOF-1.

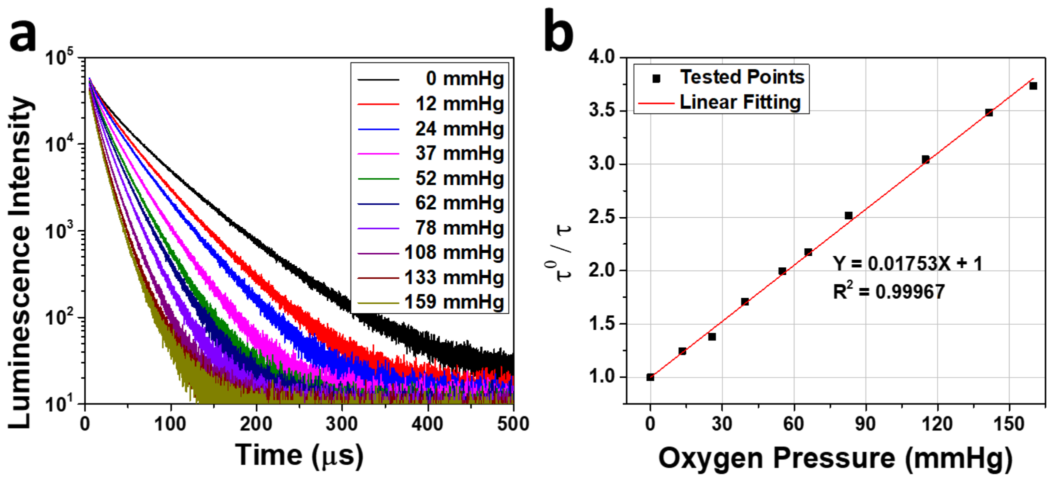

Figure 1-17. (a) Phosphorescent decays (λ_{ex} = 405 nm) of R-nMOF-1 in HBSS buffer under various oxygen partial pressures. (b) τ^0/τ as function of $p\mathrm{o}_2$ ranging from 0 mmHg to 160 mmHg. Reprinted with permission from *J. Am. Chem. Soc.*, **2016**, *138*, 2158–2164. Copyright 2016 American Chemical Society.

Next we tested the validity of the ratiometric sensors by CLSM. R-nMOF-2 was dispersed in HBSS buffer and subjected to CLSM imaging under different pO_2. Upon excitation with a 514 nm Argon laser, signals in the range of 620-660 nm and 540-580 nm were collected in two separate channels (**Figure 1-18**) and analyzed by ImageJ to quantify the intensity ratios, referred as I_P/I_F. Notably, the I_P/I_F - pO_2 curve (**Figure 1-19**) deviates from that obtained by fluorimetry (**Figure 1-15** and **1-16**), which is reasonable given that the process of collecting photoluminescence on a CLSM is much more complicated than using a fluorimeter. Many factors besides pO_2, such as laser power and dwell time can influence the absolute and relative intensities of phosphorescence/fluorescence.[119] We also noticed that the phosphorescence component was more prominent under CLSM with our instrument settings, so we used R-nMOF-2 with a higher RITC loading for CLSM experiments. The I_P/I_F - pO_2 curves obtained by CLSM are highly reproducible

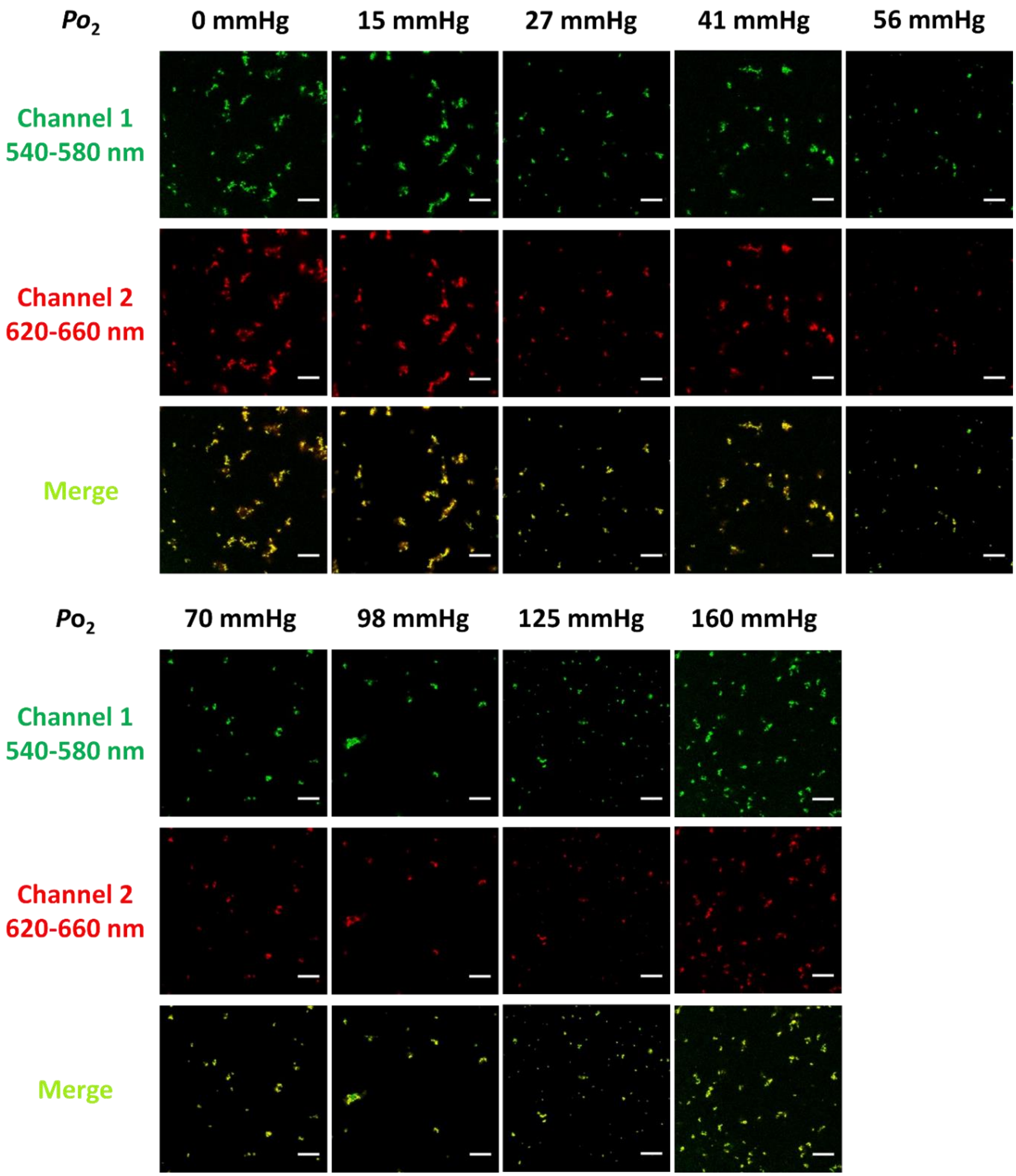

Figure 1-18. Images of R-nMOF-2 dispersed in HBSS with a series of pO_2 acquired by CLSM using 514 nm excitation, and two-channel collection. Bar: 10 μm. Reprinted with permission from *J. Am. Chem. Soc.*, **2016**, *138*, 2158–2164. Copyright 2016 American Chemical Society.

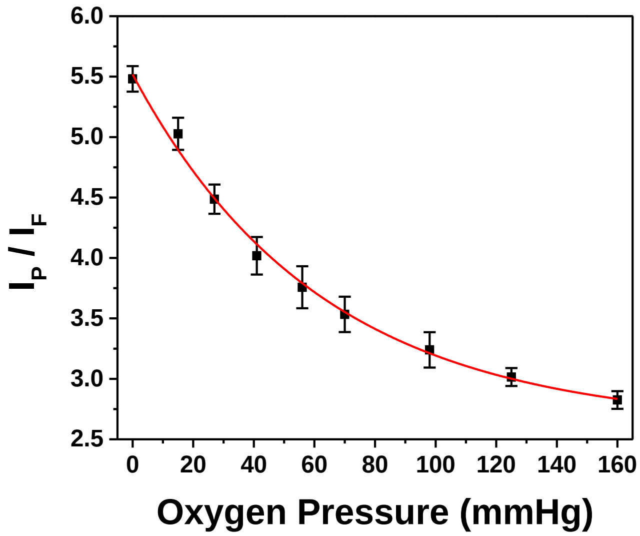

Figure 1-19. Calibration curve of the phosphorescence/fluorescence intensity of R-nMOF-2 on CLSM under different oxygen partial pressures. Reprinted with permission from *J. Am. Chem. Soc.*, **2016**, *138*, 2158–2164. Copyright 2016 American Chemical Society.

with the I_P/I_F ratio gradually decreasing as pO_2 increases, and are fitted with a rational function (Formula **1-3**):

$$y = \frac{I_P}{I_F} = \frac{kP_{O_2}+b}{P_{O_2}+c} \qquad (1\text{-}3)$$

where y is the intensity ratio of phosphorescence to fluorescence, k, b and c are fitting parameters. The fitted equation is thus derived as:

$$y = \frac{1.544P_{O_2}+398.8}{P_{O_2}+71.77}, \quad R^2 = 0.993 \qquad (1\text{-}4)$$

This equation serves as a standard curve for intracellular pO_2 measurements.

1.2.3. *In-vitro* assay

We chose mouse colon carcinoma CT26 cells for *in vitro* imaging because they show little background autofluorescence under our measurement conditions. The cellular uptake of R-nMOF-2 in CT26 cells was first investigated by incubating CT26 cells with 15 μg/mL R-nMOF-2 for different times. Time-dependent endocytosis was quantified by ICP-MS and shown in **Figure 1-20**. Efficient cellular uptake (~2.5 pg/cell) was observed after a 2 h incubation, which indicates feasibility for intracellular pO_2 measurements.

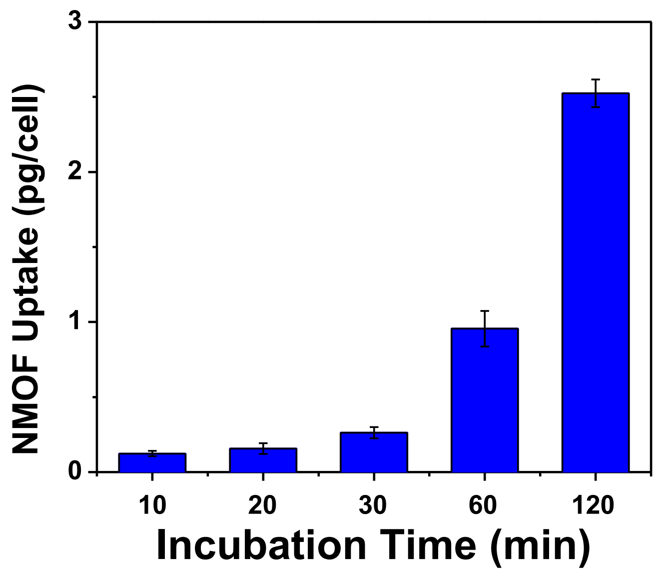

Figure 1-20. Time-dependent cellular uptake of R-nMOF-2 in CT26 cells determined by ICP-MS. Reprinted with permission from *J. Am. Chem. Soc.*, **2016**, *138*, 2158–2164. Copyright 2016 American Chemical Society.

We also investigated the cytotoxicity of T26 cells by treating the cells with different concentrations of R-nMOF-2 for 72 h and examining cell viability afterwards. R-nMOF-2 showed low cytotoxicity on CT26 cells with over 90% cell viability at concentration lower than 50 μg/mL

(**Figure 1-21**). The concentration used for cellular uptake and imaging was 30 μg/mL, less than 50 μg/mL. In addition, the cells were only incubated with R-nMOF-2 for 2 h for cellular uptake and imaging, so the cells should be in good health during the experiments.

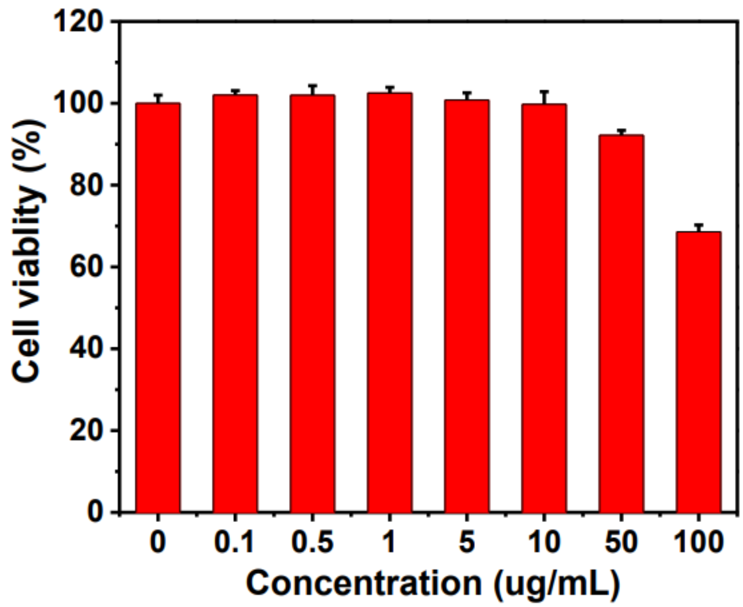

Figure 1-21. Cytotoxicity of R-nMOF-2 in CT26 cells. Reprinted with permission from *J. Am. Chem. Soc.*, **2016**, *138*, 2158–2164. Copyright 2016 American Chemical Society.

Finally we used R-nMOF-2 to examine cellular O_2 levels. CT26 cells were incubated with R-nMOF-2 for 2 h. The culturing media were then exchanged to HBSS buffer with different pO_2 in a sealed chamber, and cells were incubated for another 15 min to ensure efficient oxygen exchange across cell plasma membranes. CLSM settings were identical to those used for the calibration curve. We tested three different pO_2 conditions: 4 mmHg, 32 mmHg, and 160 mmHg, which represent hypoxia, normoxia and aerated conditions, respectively. The phosphorescence/fluorescence intensity ratios of R-nMOF-2 were shown by pseudocolor images in **Figure 1-22**. Different channels of cellular uptake of R-nMOF-2 captured by CLSM are shown in **Figure 1-23**. The I_P/I_F values of internalized R-nMOF-2 analyzed by ImageJ were 5.29 ± 0.12, 4.45 ± 0.09, and 2.80 ± 0.06, respectively. According to Formula 1-3,

$$P_{O_2} = \frac{b-cy}{y-k} \tag{1-5}$$

$$dP_{O_2} = \frac{kc-b}{(y-k)^2} \tag{1-6}$$

Using the fitting data b = 398.8 mmHg, c = 71.77 mmHg, k = 1.544,

Insert y = 5.29, $dy = 0.12$ into Formula 1-5 and 1-6 respectively, we get $P_{O_2} =$ 5.1 mmHg, $dP_{O_2} =$ 2.5 mmHg;

Similarly, when $\frac{I_P}{I_F} = 4.45 \pm 0.09$, $P_{O_2} = 27.3 \pm$ 3.1 mmHg;

when $\frac{I_P}{I_F} = 2.80 \pm 0.06$, $P_{O_2} = 158 \pm$ 11 mmHg.

These resulting pO_2 values, 5.1 ± 2.5, 27.3 ± 3.1, and 158 ± 11 mmHg, matched well with the preset pO_2 values in the chamber. The data suggest a broad detection range and good accuracy of R-nMOF as an intracellular oxygen sensor.

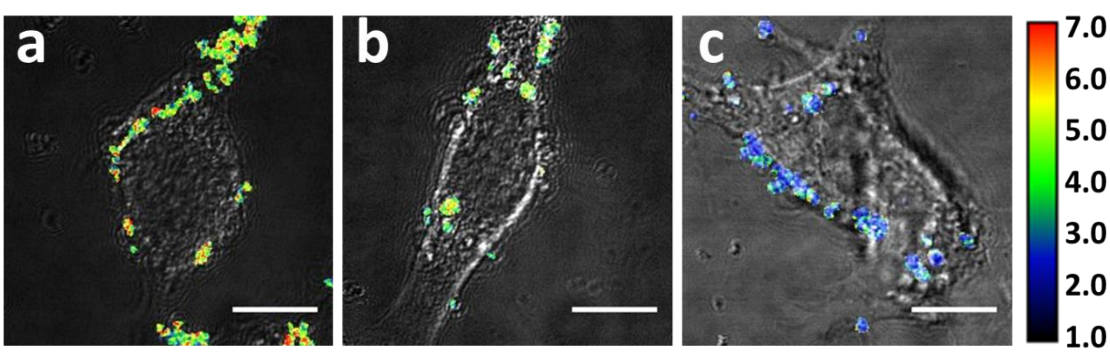

Figure 1-22. Ratiometric luminescence imaging (λ_{ex} = 514 nm) of CT26 cells after incubation with R-nMOF-2 under (a) hypoxia (4 mmHg), (b) normoxia (32 mmHg), and (c) aerated (160

mmHg) conditions. Bar: 10 μm. Reprinted with permission from *J. Am. Chem. Soc.*, 2016, *138*, 2158–2164. Copyright 2016 American Chemical Society.

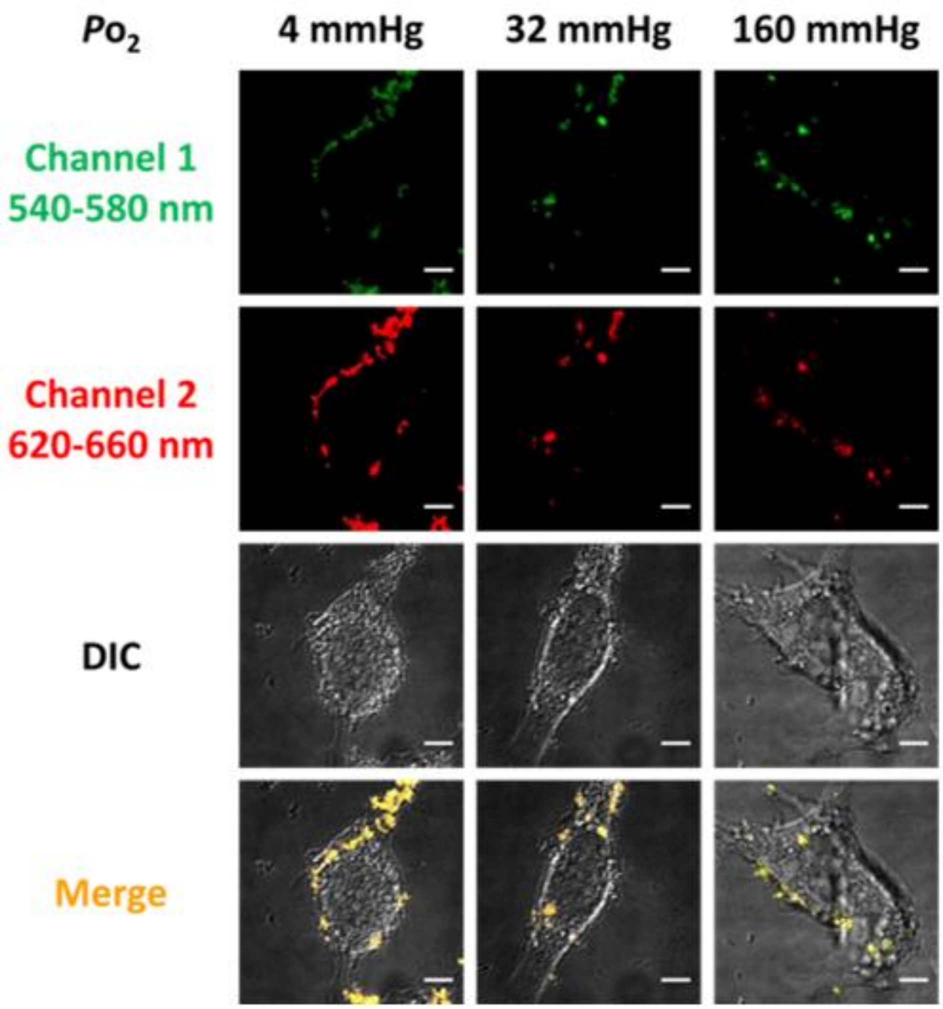

Figure 1-23. Channel 1 (540-580 nm), Channel 2 (620-660 nm), and DIC images of live cells under hypoxia (4 mmHg), normoxia (32 mmHg), and aerated conditions (160 mmHg) after incubation with R-nMOF-2. Bar: 5 μm. Reprinted with permission from *J. Am. Chem. Soc.*, **2016**, *138*, 2158–2164. Copyright 2016 American Chemical Society.

We also tested photoluminescence stability of the R-nMOF system. After incubation for 1-4 hours and washing with HBSS three times, R-nMOF-2 in CT26 cells were tested under CLSM in air and the results were summarized in **Figure 1-24**. The phosphorescence/fluorescence intensity ratio of R-nMOF remains stable 4 hours after cellular uptake.

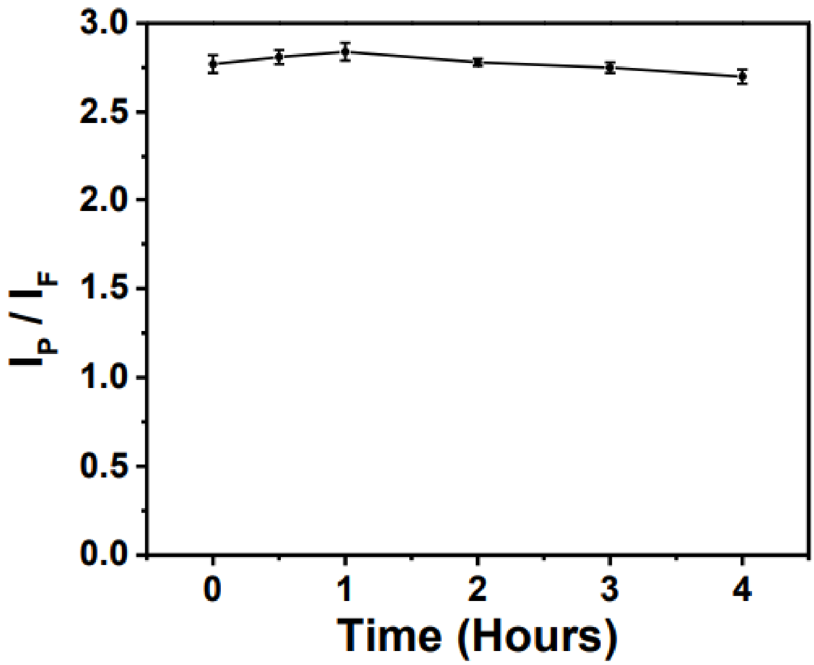

Figure 1-24. Time-lapse phosphorescence/fluorescence ratio of R-nMOF-2 in CT26 cells in air on CLSM. Reprinted with permission from *J. Am. Chem. Soc.*, **2016**, *138*, 2158–2164. Copyright 2016 American Chemical Society.

1.3. Conclusion

In this work, we have rationally designed and synthesized the first stable, crystalline, porous, and dual-emissive R-nMOFs for ratiometric sensing of intracellular oxygen in live cells. R-nMOF was synthesized by mixing two ligands with similar length but very different chemical structure followed by postsynthetic modification. Importantly, the ratio of RITC and DBP-Pt in R-nMOF can be tuned by changing the feed ratio during hydrothermal synthesis and postsynthetic modification. RITC and DBP-Pt can be excited simultaneously and there is minimal energy transfer and emission overlap, which ensures the validity for ratiometric oxygen sensing. The phosphorescence/fluorescence ratio and phosphorescence lifetime are in good accordance with the Stern-Völmer equation. *In vitro* assays under CLSM demonstrate a broad detection range and good accuracy of R-nMOF as an intracellular oxygen sensor. This study should inspire the design of new nMOFs for sensing other biologically important analytes by taking advantage of the synthetic tunability and versatility as well as other unique attributes of nMOFs.

1.4. Methods and Experimental Details

1.4.1 Synthesis and Characterization of ligands

Amino-quaterphenyldicarboxylic acid ($H_2QPDC-NH_2$) was synthesized as shown in **Scheme 1-1**.

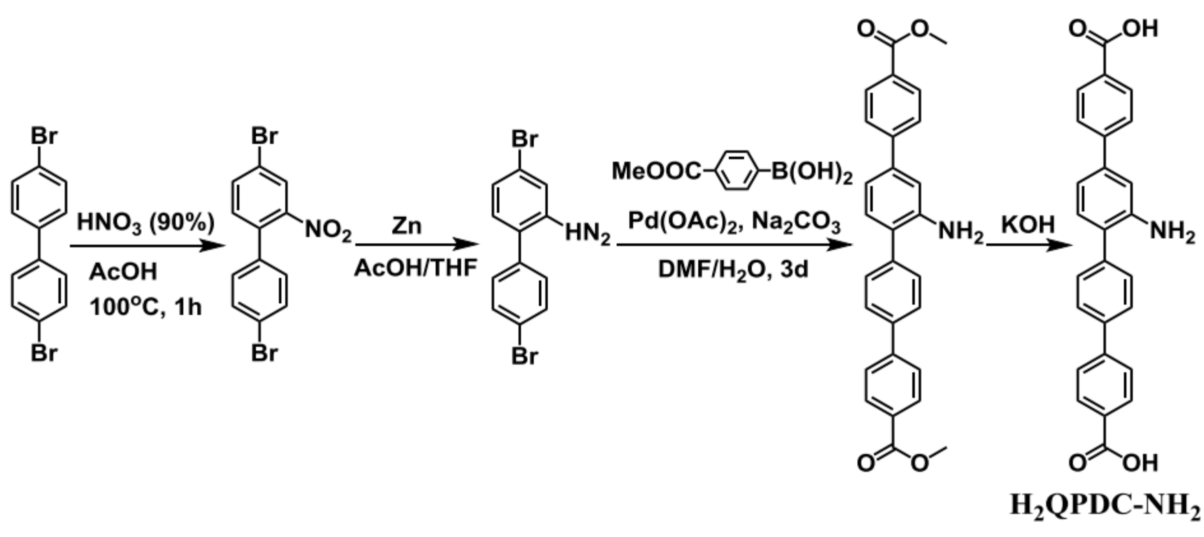

Scheme 1-1. Synthesis of $H_2QPDC-NH_2$. Reprinted with permission from *J. Am. Chem. Soc.*, **2016**, *138*, 2158–2164. Copyright 2016 American Chemical Society.

2-Amino-4,4'-dibromobiphenyl. To a solution of 2-nitro-4,4'-dibromobiphenyl (5.00 g, 14.0 mmol) in THF (40 mL) was added Zn powder (9.16 g, 140 mmol) and acetic acid (8.01 mL, 140 mmol). The reaction mixture was stirred at RT for 24 h. CH_2Cl_2 (100 mL) was added, and the Zn powder was removed by filtration through celite. The filtrate was washed with water (2×25 mL), Na_2CO_3 (satd) (25 mL), and brine (25 mL). The organic extract was dried over $MgSO_4$ and filtered. After evaporation of the solvent, the residue was subjected to flash column chromatography on silica gel (10:90 CH_2Cl_2/hexanes to 50:50 CH_2Cl_2/hexanes as eluent) affording 2-amino-4,4'-dibromobiphenyl (3.78 g, 11.6 mmol, 82.5% yield) as a colorless solid. ^{1}H NMR (500 MHz, CDCl3): δ 7.57 (d, J = 6.5 Hz, 2H), 7.28 (d, J = 6.5 Hz, 2 H), 6.93-6.91 (m, 3H), 3.87 (bs, 2H); 13C NMR (125 MHz, $CDCl_3$): δ 137.30, 132.15, 131.55, 130.65, 125.20, 122.42, 121.72, 121.67, 118.28; ESI-MS: calcd. for $[M]^+$ 324.9; found 324.9.

Methyl Amino-quaterphenyldicarboxylic ester (Me_2QPDC-NH_2). 2-amino-4,4'-dibromo-1,1'-biphenyl (3.00 g, 9.17 mmol) and methyl-4-carboxylphenyl boronic acid (4.95 g, 27.5 mmol) were charged to a 2-neck RB flask fitted with a reflux condenser, and then DMF (82.8 mL) was added. The solution was degassed by freeze-pump-thaw twice, and palladium(II) acetate (103 mg, 0.458 mmol) was added. The solution was degassed further for 30 minutes by sparging N_2. Na_2CO_3•H_2O (4.65 g, 33.6 mmol) dissolved in deionized water (50 mL) then degassed by freeze-pump-thaw (5x) was added under N_2. The reaction mixture was then heated under N_2 at 70 °C for 72 h. The solution was cooled to room temperature, and the crude reaction mixture was concentrated by rotary evaporation. The remaining solid was then added a 1:1 mixture of $CHCl_3$/H_2O (250 mL total volume) and stirred for 1 hour. The organic layer was isolated with a separatory funnel, and the aqueous was further extracted with chloroform (3×100 mL). The combined organic extracts were dried with $MgSO_4$, and the volatiles were removed in vacuo. The remaining solids were purified by column chromatography using chloroform as the eluent, affording $Me_2QPDC-NH_2$ as a pale yellow solid (1.78 g, 4.07 mmol, 44% yield). ^1H NMR (500 MHz, CDCl3): δ 8.10 (dd, *J* = 10.5, 9.5 Hz, 4H), 7.94 (d, *J* = 8.0 Hz, 2 H), 7.90 (d, *J* = 8.5 Hz, 2H), 7.82 (d, *J* = 8.5 Hz, 2H), 7.66 (d, *J* = 8.5 Hz, 2H), 7.23 (d, *J* = 8.0 Hz, 1H), 7.21 (d, *J* = 2.0 Hz, 1H), 7.07 (dd, *J* = 1.5, 7.2 Hz, 1H), 5.13 (bs, 2H), 3.93 (s, 3H), 3.92 (s, 3H); ESI-MS: calcd. for $[M+H]^+$ 438.2; found 438.1.

Amino-quaterphenyldicarboxylic acid ($H_2QPDC-NH_2$). A suspension of $Me_2QPDC-NH_2$ (1.40 g, 3.20 mmol) in THF (220 mL) was heated to 40 °C. A solution of KOH (23.3 g, 414 mmol) dissolved in MeOH (80 mL) was then added, and the reaction mixture was stirred at 40 °C for 16 h. The suspension was cooled to room temperature, and the resulting precipitate was collected by centrifugation. The solid was washed with dry THF (20 mL) and re-collected by centrifugation. The solid was suspended in THF (20 mL) and trifluoroacetic acid (5 mL) was slowly added and stirred for 1.5 h at room temperature. H_2O (15 mL) was then added, and the yellow solid was isolated by centrifugation. The collected yellow solid was first washed with THF (10 mL), then Et_2O (10 mL), then dried in vacuo to obtain $H_2QPDC-NH_2$ as a yellow powder (1.31 g, 2.75 mmol, 85.9% yield). ^1H NMR (500 MHz, DMSO-d6): δ 13.0 (bs, 2H), 8.10- 8.06 (m, 4H), 7.89 (dd, *J* = 12.5, 11 Hz, 4H), 7.78 (d, *J* = 8.5 Hz, 2H), 7.65 (d, *J* = 8.0 Hz, 2H), 7.21-7.20 (m, 2H), 7.05 (d, *J* = 7.5 Hz, 1H), 5.16 (bs, 2H); 13C NMR (125 MHz, CDCl3): δ 167.66, 167.63, 146.23, 145.11,144.39, 139.65, 139.57, 137.87, 131.27, 130.53, 130.42, 130.06, 129.91, 129.72, 127.80, 127.11, 126.94, 125.54, 116.03, 114.17; ESI-MS: calcd. for $[M+H]^+$ 410.1, found 410.0.

Pt(II)-5,15-di(p-benzoato)porphyrin ($H_2DBP-Pt$) was synthesized as shown in **Scheme 1-2**. Me_2DBP was synthesized according to our previous report.[43]

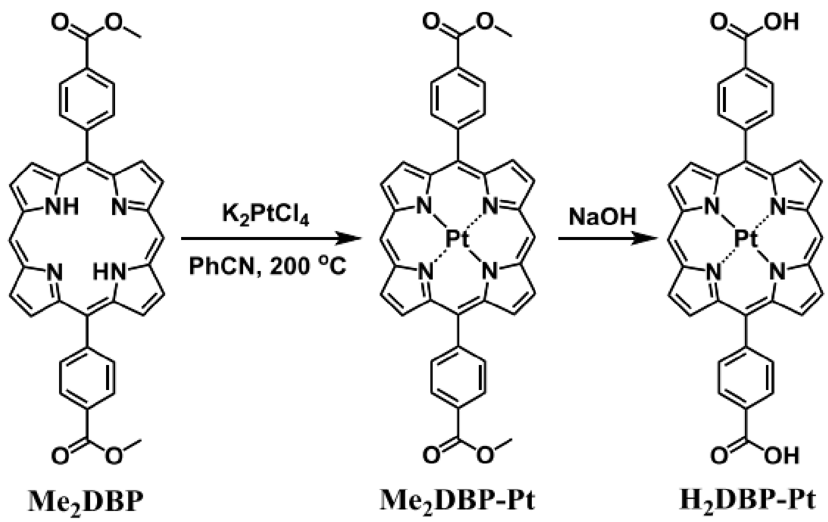

Scheme 1-2. Synthesis of H_2DBP-Pt. Reprinted with permission from *J. Am. Chem. Soc.*, **2016**, *138*, 2158–2164. Copyright 2016 American Chemical Society.

Me_2DBP-Pt was prepared by refluxing K_2PtCl_4 (300 mg, 720 μmol) and 5,15-di(p-methylbenzoato)porphyrin (Me_2DBP) (210 mg, 360 μmol) in benzonitrile (130 mL) in a sand bath for 24 h. After cooling to room temperature, benzonitrile was removed under reduced pressure. The crude product was purified by silica gel column chromatography with methylene chloride as eluent to afford a deep red product. Yield: 190 mg, 246 μmol, 68 %. The ^{1}H NMR spectrum of Me_2DBP-Pt is shown in **Figure 1-25**. ^{1}H-NMR (500 MHz, Chloroform-d, ppm): δ = 10.21 (s, 2H), 9.26 (d, 4H), 8.90 (d, 4H), 8.48 (d, 4H), 8.31 (d, 4H), 4.14 (s, 6H). ESI-MS for Me_2DBP-Pt ($C_{36}H_{24}N_4O_4Pt$) $[M+H]^+$: calcd. 772.1; found: 772.1.

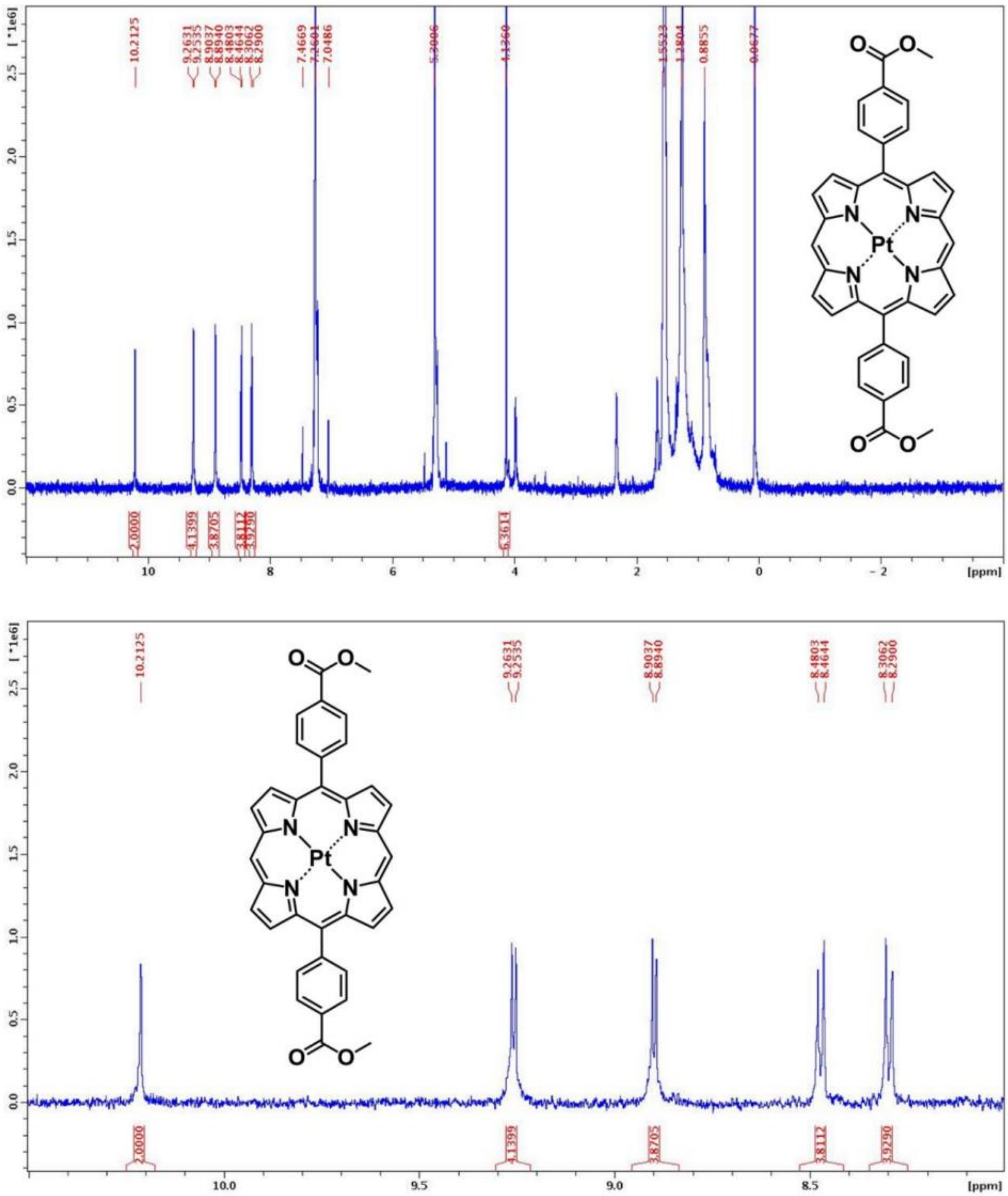

Figure 1-25. ^{1}H NMR spectrum of Me_2DBP-Pt. Reprinted with permission from *J. Am. Chem. Soc.*, **2016**, *138*, 2158–2164. Copyright 2016 American Chemical Society.

H_2DBP-Pt was prepared by refluxing Me_2DBP-Pt (190 mg, 246 μmol) in a mixture of tetrahydrofuran (THF, 15 mL), methanol (15 mL), and an aqueous solution of potassium hydroxide (5 mL, 2 M) for 12 h. After cooling to room temperature, most of the solvent was removed by rotary evaporation before the solution was acidified to pH < 3 with hydrochloric acid. The red product was obtained by filtration and washed with water and ether and then dried under a vacuum. Yield: 178 mg, 240 μmol, 98 %. The ^{1}H NMR spectrum of H_2DBP-Pt is shown in **Figure 1-26**. ^{1}H NMR (500 MHz, DMSO-d^6, ppm): δ =13.35 (s, 2H), 10.60 (s, 2H), 9.54 (d, 4H), 8.90 (d, 4H), 8.42 (d, 4H), 8.36 (d, 4H). ESI-MS for H_2DBP-Pt ($C_{34}H_{20}N_4O_4Pt$) $[M+H]^+$: calcd. 744.1; found: 744.1.

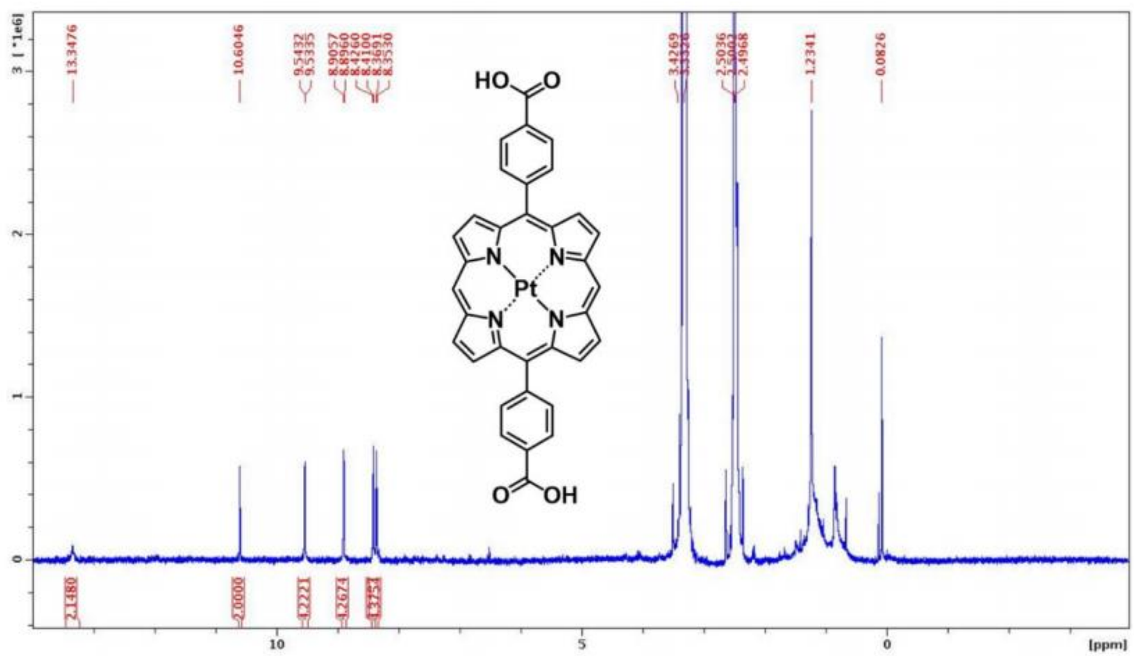

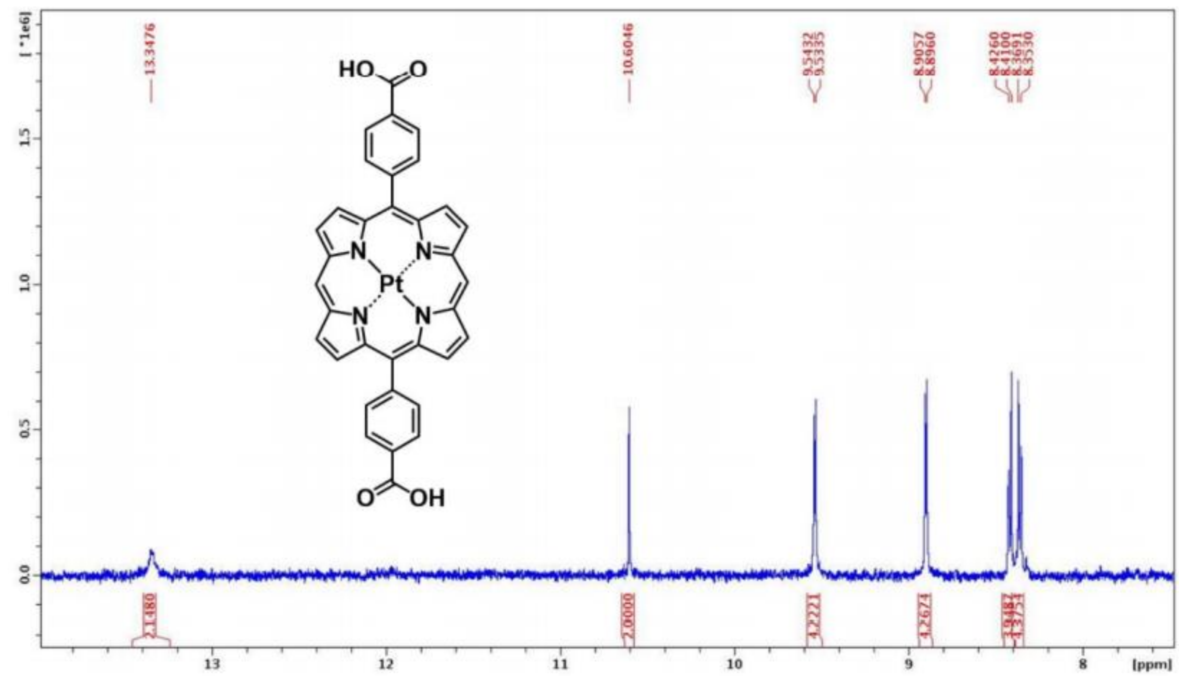

Figure 1-26. ^{1}H NMR spectrum of H_2DBP-Pt. Reprinted with permission from *J. Am. Chem. Soc.*, **2016**, *138*, 2158–2164. Copyright 2016 American Chemical Society.

1.4.2 Experimental Details

Synthesis of M-nMOF: H_2QPDC-NH_2 (20.5 mg, 50 μmol) and H_2DBP-Pt (7.44 mg, 10 μmol) were mixed with 1 mL AcOH and 19 mL dimethylformamide (DMF) solution of $HfCl_4$ (19.2 mg, 60 μmol), and the mixture was kept in an 80 °C oven for 4 days. The product was collected by centrifugation and washed with DMF and ethanol, yielding M-NMOF as an orange powder.

Synthesis of R-nMOF: A methanol solution of Rhodamine-B-Isothiocyanate (RITC, 1 mM) was added to 2.0 mg of M-nMOF suspended in 0.5 mL methanol. The mixture was stirred gently at room temperature in the dark for 3 h to afford Rhodamine-B-conjugated M-nMOFs (R-nMOF). 40 μL/150 μL RITC solution were used to afford R-nMOF-1/R-nMOF-2. The product was collected by centrifugation and washed with ethanol, yielding R-nMOF as a red powder. R-nMOF was saved in ethanol as a stock solution for further use.

Digestion for ICP-MS: 150 μL R-NMOF (~1 mg/mL) suspension in ethanol was added into 6 mL HNO_3/HF/HCl (18:1:1 v/v/v), which was then digested at 170 °C for 20 min (MARS 6, OneTouch) to ensure complete porphyrin digestion. The resulting digestion solution was diluted with water. Hf and Pt concentration was then obtained by ICP-MS and the molar ratio of Pt:Hf = 6.2:93.8.

Mass spectrometry: MS was performed on Agilent 1100 LC/MSD with ESI and APCI ion sources. R-NMOF in ethanol was digested with HF solution in methanol. The sample was delivered with methanol.

Powder X-ray diffraction (PXRD): The PXRD patterns of NMOF samples were collected on a Bruker D8 Venture, dual microsource (Cu and Mo) diffractometer with a CMOS detector. Cu Kα radiation was used. The PXRD patterns were processed with the APEX 2 package using a PILOT plug-in.

Dye release measurements: 100 μg R-nMOF was incubated in 1mL HBSS. After incubating for 1 h, 2 h, 4 h, and 24 h, the suspension was subjected to centrifugation at 13,000 rpm for 15 min. 0.6 mL of the supernatant was collected and another 0.6 mL of fresh HBSS was added. The supernatant was diluted to 1.2 mL and used for UV-vis spectra measurement

Quantum yields measurements: The quantum yields of R-nMOF-1 and R-nMOF-2 were measured in HBSS using Rhodamine-B as standard (QY = 0.31 in water excited at 514 nm).[120] The quantum yield of the R-nMOF-1 and R-nMOF-2 in HBSS was calculated according to the following equation:

$$\Phi = \Phi_r * \frac{A_r}{I_r} * \frac{I}{A} * \frac{{n_r}^2}{n^2} \tag{1-7}$$

where Φ is the quantum yield, *I* is the measured integrated emission intensity, n is the refractive index (1.333 for water), and A is the optical density. The subscript "r" refers to the reference fluorophore of known quantum yield. In order to minimize reabsorption effects, the absorbencies in the 10 mm fluorescence cuvette were kept under 0.1 at the related excitation wavelengths. The quantum yields of R-nMOF-1 and R-nMOF-2 are 0.08 and 0.15, respectively (excited at 514 nm).

Fluorescence measurements: Emission spectra of R-nMOF-1 and R-nMOF-2 in HBSS under different pO_2 were obtained on a fluorimeter (RF-5301PC). A cuvette containing 3 mL R-nMOF-1 or R-nMOF-2 (10 μg/mL) suspension was placed in a glove box. The oxygen concentration in the glove box was adjusted by controlling the flow rate of air and nitrogen, and monitored by a commercial oxygen sensor (YSI ProODO 626279). The R-nMOF-1 or R-nMOF-2 suspension was bubbled with pipette for 5 min to reach equilibrium. The cuvette was then capped and subjected to emission measurements on fluorimeter (Fluorolog-3, Horiba, Japan).

Lifetime measurements: The phosphorescence decay of R-nMOF-1 in HBSS under different oxygen concentrations was measured with ChromsBH lifetime fluorimeter (ISS, Inc.). A 405 nm laser was used as the excitation source, and time-lapse 641±37 nm emission intensity was monitored on microsecond scale. A capped cuvette was used to hold the sample, and the sample preparation was similar to that in fluorescence measurement. The phosphorescence decay curves were fitted by exponential decay.

CLSM imaging of R-nMOF: The phosphorescence/fluorescence responses to pO_2 ranging from 0 mmHg to 160 mmHg of R-nMOF-2 in HBSS solution were evaluated by confocal laser scanning microscopy (CLSM, Leica SP5 II, Integrated Microscopy Core Facility at the University of

Chicago). 15 μL of R-nMOF-2 (1 mg/mL) was dispersed in 1 mL HBSS and transferred to glove box at a preset oxygen partial pressure. The suspension was bubbled for 5 min to reach equilibrium and added to a glass-bottom petri dish (No. 1.5, uncoated glass, MatTek Corporation), which was covered with another inverted petri dish and sealed with parafilm. The sample was then observed under confocal microscope. Images were collected using Leica SP5 II microscope equipped with 100X, 1.4 oil objective, PMT detector, and transmitted light detector with differential interference contrast (DIC). A 514 nm laser was used as the excitation source. 540-580 nm and 620-660 nm luminescence signals were collected in two different channels. The laser scanning frequency was set to 8 Hz with line scan mode (line average = 1). Images were obtained in the format of 256×256 pixel. The intensity ratio of R-nMOF-2 in the two channels were analyzed by ImageJ (**Figure 1-20**). 3-8 samples were tested under each condition to give the standard deviation of pO_2.

Cytotoxicity measurement: CT26 cells were seeded on a 96-well plate at a density of 2×103 cells per well. After overnight incubation, the cells were treated with different concentrations of R-nMOF-2 for 72 h. At the end of the incubation period, cell viability was measured by (3-(4,5-dimethylthiazol-2-yl)-5-(3-carboxymethoxyphenyl)-2-(4-sulfophenyl)-2H-tetrazolium) (MTS) assay (Promega, Madison, WI) according to the manufacturer's instructions.

Cellular uptake: CT26 cells were seeded on a 6-well plate at 1×10^6 cells per well and cultured for 24 h. 30 μL R-nMOF-2 (2 mg/mL) were added to each well. After incubation for 10 min, 20 min, 30 min, 60 min, and 120 min, cell media were discarded. The cells were washed with HBSS three times, and counted with hemocytometer. The cells were then centrifuged at 3,000 rpm for 5 min, and the cell pellet was digested with 100 μL HNO_3/HF (9:1 v/v). After 24 h, the digestion was diluted with water and subjected to ICP-MS to determine the Hf concentration. Three parallel experiments were conducted for each time point. Results were expressed as the amount of R-nMOF-2 calculated from the Hf concentration associated with one cell.

Live cell imaging: CT26 cells were seeded on a glass-bottom petri dish at a density of 1×10^6 cells/well and cultured for 24 h. 30 μL R-nMOF-2 (2 mg/mL) was then added and the cells were cultured for another 2 h. The cell media were discarded, and the cells were washed with HBSS three times and sealed in the petri dish under different pO_2 using the method described in CLSM imaging. Images were collected using Leica SP5 II microscope equipped with 100×, 1.4 oil objective, PMT detector, and transmitted light detector with differential interference contrast (DIC). The laser scanning frequency was set to 8 Hz with line scan mode (line average = 1). Images were obtained in the format of 256×256 pixel. Cells were imaged in three channels to yield three images: (1) exciting at 514 nm and collecting at 540-580 nm; (2) exciting at 514 nm and collecting at 620-660 nm; (3) DIC (**Figure 1-23**). The data were process by ImageJ and the intensity ratio of R-NMOF-2 in Channel 1/Channel 2 was obtained. Using the standard curve under CLSM as reference, the oxygen partial pressure can be calculated. 3-8 samples were tested under each condition to give the standard deviation.

1.5 References

(1) Batten Stuart, R.; Champness Neil, R.; Chen, X.-M.; Garcia-Martinez, J.; Kitagawa, S.; Öhrström, L.; O'Keeffe, M.; Paik Suh, M.; Reedijk, J. In *Pure Appl. Chem.* 2013; Vol. 85, p 1715.

(2) Batten, S. R.; Champness, N. R.; Chen, X.-M.; Garcia-Martinez, J.; Kitagawa, S.; Ohrstrom, L.; O'Keeffe, M.; Suh, M. P.; Reedijk, J. Coordination polymers, metal-organic frameworks and the need for terminology guidelines. *CrystEngComm.* **2012**, *14*, 3001-3004.

(3) Buser, H. J.; Schwarzenbach, D.; Petter, W.; Ludi, A. The crystal structure of Prussian Blue: $Fe_4[Fe(CN)_6]_3.xH_2O$. *Inorg. Chem.* **1977**, *16*, 2704-2710.

(4) Yaghi, O. M.; Li, G.; Li, H. Selective binding and removal of guests in a microporous metal–organic framework. *Nature*. **1995**, *378*, 703.

(5) Gable, R. W.; Hoskins, B. F.; Robson, R. Synthesis and structure of $[NMe_4][CuPt(CN)_4]$: an infinite three-dimensional framework related to PtS which generates intersecting hexagonal channels of large cross section. *J. Chem. Soc., Chem. Commun.* **1990**, 762-763.

(6) Hoskins, B. F.; Robson, R. Infinite polymeric frameworks consisting of three dimensionally linked rod-like segments. *J. Am. Chem. Soc.* **1989**, *111*, 5962-5964.

(7) Abrahams, B. F.; Hoskins, B. F.; Robson, R. A honeycomb form of cadmium cyanide. A new type of 3D arrangement of interconnected rods generating infinite linear channels of large hexagonal cross-section. *J. Chem. Soc., Chem. Commun.* **1990**, 60-61.

(8) Gable, R. W.; Hoskins, B. F.; Robson, R. A new type of interpenetration involving enmeshed independent square grid sheets. The structure of diaquabis-(4,4[prime or minute]-bipyridine)zinc hexafluorosilicate. *J. Chem. Soc., Chem. Commun.* **1990**, 1677-1678.

(9) Wang, C.; Liu, D.; Lin, W. Metal–Organic Frameworks as A Tunable Platform for Designing Functional Molecular Materials. *J. Am. Chem. Soc.* **2013**, *135*, 13222-13234.

(10) Zhou, H.-C.; Long, J. R.; Yaghi, O. M. Introduction to Metal–Organic Frameworks. *Chem. Rev.* **2012**, *112*, 673-674.

(11) Long, J. R.; Yaghi, O. M. The pervasive chemistry of metal-organic frameworks. *Chem. Soc. Rev.* **2009**, *38*, 1213-1214.

(12) Cui, Y.; Li, B.; He, H.; Zhou, W.; Chen, B.; Qian, G. Metal–Organic Frameworks as Platforms for Functional Materials. *Acc. Chem. Res.* **2016**, *49*, 483-493.

(13) Yang, Q.; Xu, Q.; Jiang, H.-L. Metal-organic frameworks meet metal nanoparticles: synergistic effect for enhanced catalysis. *Chem. Soc. Rev.* **2017**, *46*, 4774-4808.

(14) Eddaoudi, M.; Kim, J.; Rosi, N.; Vodak, D.; Wachter, J.; Keeffe, M.; Yaghi, O. M. Systematic Design of Pore Size and Functionality in Isoreticular MOFs and Their Application in Methane Storage. *Science.* **2002**, *295*, 469-472.

(15) Suh, M. P.; Park, H. J.; Prasad, T. K.; Lim, D.-W. Hydrogen Storage in Metal–Organic Frameworks. *Chem. Rev.* **2012**, *112*, 782-835.

(16) Li, B.; Wen, H.-M.; Wang, H.; Wu, H.; Tyagi, M.; Yildirim, T.; Zhou, W.; Chen, B. A Porous Metal–Organic Framework with Dynamic Pyrimidine Groups Exhibiting Record High Methane Storage Working Capacity. *J. Am. Chem. Soc.* **2014**, *136*, 6207-6210.

(17) Hu, T.-L.; Wang, H.; Li, B.; Krishna, R.; Wu, H.; Zhou, W.; Zhao, Y.; Han, Y.; Wang, X.; Zhu, W.; Yao, Z.; Xiang, S.; Chen, B. Microporous metal–organic framework with dual functionalities for highly efficient removal of acetylene from ethylene/acetylene mixtures. *Nat. Comm.* **2015**, *6*, 7328.

(18) Xiang, S.; He, Y.; Zhang, Z.; Wu, H.; Zhou, W.; Krishna, R.; Chen, B. Microporous metal-organic framework with potential for carbon dioxide capture at ambient conditions. *Nat. Comm.* **2012**, *3*, 954.

(19) Evans, O. R.; Lin, W. Crystal Engineering of NLO Materials Based on Metal−Organic Coordination Networks. *Acc. Chem. Res.* **2002**, *35*, 511-522.

(20) Wang, C.; Zhang, T.; Lin, W. Rational Synthesis of Noncentrosymmetric Metal–Organic Frameworks for Second-Order Nonlinear Optics. *Chem. Rev.* **2012**, *112*, 1084-1104.

(21) Mingabudinova, L. R.; Vinogradov, V. V.; Milichko, V. A.; Hey-Hawkins, E.; Vinogradov, A. V. Metal-organic frameworks as competitive materials for non-linear optics. *Chem. Soc. Rev.* **2016**, *45*, 5408-5431.

(22) Jain, P.; Ramachandran, V.; Clark, R. J.; Zhou, H. D.; Toby, B. H.; Dalal, N. S.; Kroto, H. W.; Cheetham, A. K. Multiferroic Behavior Associated with an Order−Disorder Hydrogen Bonding Transition in Metal−Organic Frameworks (MOFs) with the Perovskite ABX_3 Architecture. *J. Am. Chem. Soc.* **2009**, *131*, 13625-13627.

(23) Zhang, W.; Xiong, R.-G. Ferroelectric Metal–Organic Frameworks. *Chem. Rev.* **2012**, *112*, 1163-1195.

(24) Mon, M.; Ferrando-Soria, J.; Verdaguer, M.; Train, C.; Paillard, C.; Dkhil, B.; Versace, C.; Bruno, R.; Armentano, D.; Pardo, E. Postsynthetic Approach for the Rational Design of Chiral Ferroelectric Metal–Organic Frameworks. *J. Am. Chem. Soc.* **2017**, *139*, 8098-8101.

(25) Talin, A. A.; Centrone, A.; Ford, A. C.; Foster, M. E.; Stavila, V.; Haney, P.; Kinney, R. A.; Szalai, V.; El Gabaly, F.; Yoon, H. P.; Léonard, F.; Allendorf, M. D. Tunable Electrical Conductivity in Metal-Organic Framework Thin-Film Devices. *Science.* **2014**, *343*, 66-69.

(26) Wu, G.; Huang, J.; Zang, Y.; He, J.; Xu, G. Porous Field-Effect Transistors Based on a Semiconductive Metal–Organic Framework. *J. Am. Chem. Soc.* **2017**, *139*, 1360-1363.

(27) Sheberla, D.; Bachman, J. C.; Elias, J. S.; Sun, C.-J.; Shao-Horn, Y.; Dincă, M. Conductive MOF electrodes for stable supercapacitors with high areal capacitance. *Nat. Mater.* **2016**, *16*, 220-224.

(28) Rubio-Giménez, V.; Galbiati, M.; Castells-Gil, J.; Almora-Barrios, N.; Navarro-Sánchez, J.; Escorcia-Ariza, G.; Mattera, M.; Arnold, T.; Rawle, J.; Tatay, S.; Coronado, E.; Martí-Gastaldo, C. Bottom-Up Fabrication of Semiconductive Metal–Organic Framework Ultrathin Films. *Adv. Mater.* **2018**, *30*, 1704291.

(29) Zhao, X.; Liu, S.; Tang, Z.; Niu, H.; Cai, Y.; Meng, W.; Wu, F.; Giesy, J. P. Synthesis of magnetic metal-organic framework (MOF) for efficient removal of organic dyes from water. *Sci. Rep.* **2015**, *5*, 11849.

(30) Kurmoo, M. Magnetic metal-organic frameworks. *Chem. Soc. Rev.* **2009**, *38*, 1353-1379.

(31) Lustig, W. P.; Mukherjee, S.; Rudd, N. D.; Desai, A. V.; Li, J.; Ghosh, S. K. Metal-organic frameworks: functional luminescent and photonic materials for sensing applications. *Chem. Soc. Rev.* **2017**, *46*, 3242-3285.

(32) Cui, Y.; Yue, Y.; Qian, G.; Chen, B. Luminescent Functional Metal–Organic Frameworks. *Chem. Rev.* **2012**, *112*, 1126-1162.

(33) Zhang, C.; Wang, B.; Li, W.; Huang, S.; Kong, L.; Li, Z.; Li, L. Conversion of invisible metal-organic frameworks to luminescent perovskite nanocrystals for confidential information encryption and decryption. *Nat. Commun.* **2017**, *8*, 1138.

(34) Kreno, L. E.; Leong, K.; Farha, O. K.; Allendorf, M.; Van Duyne, R. P.; Hupp, J. T. Metal–Organic Framework Materials as Chemical Sensors. *Chem. Rev.* **2012**, *112*, 1105-1125.

(35) Yi, F.-Y.; Chen, D.; Wu, M.-K.; Han, L.; Jiang, H.-L. Chemical Sensors Based on Metal–Organic Frameworks. *ChemPlusChem.* **2016**, *81*, 675-690.

(36) Huang, Y.-B.; Liang, J.; Wang, X.-S.; Cao, R. Multifunctional metal-organic framework catalysts: synergistic catalysis and tandem reactions. *Chem. Soc. Rev.* **2017**, *46*, 126-157.

(37) Liu, J.; Chen, L.; Cui, H.; Zhang, J.; Zhang, L.; Su, C.-Y. Applications of metal-organic frameworks in heterogeneous supramolecular catalysis. *Chem. Soc. Rev.* **2014**, *43*, 6011-6061.

(38) Manna, K.; Ji, P.; Lin, Z.; Greene, F. X.; Urban, A.; Thacker, N. C.; Lin, W. Chemoselective single-site Earth-abundant metal catalysts at metal–organic framework nodes. *Nat. Commun.* **2016**, *7*, 12610.

(39) Ji, P.; Sawano, T.; Lin, Z.; Urban, A.; Boures, D.; Lin, W. Cerium-Hydride Secondary Building Units in a Porous Metal–Organic Framework for Catalytic Hydroboration and Hydrophosphination. *J. Am. Chem. Soc.* **2016**, *138*, 14860-14863.

(40) Della Rocca, J.; Liu, D.; Lin, W. Nanoscale Metal–Organic Frameworks for Biomedical Imaging and Drug Delivery. *Acc. Chem. Res.* **2011**, *44*, 957-968.

(41) Foucault-Collet, A.; Gogick, K. A.; White, K. A.; Villette, S.; Pallier, A.; Collet, G.; Kieda, C.; Li, T.; Geib, S. J.; Rosi, N. L.; Petoud, S. Lanthanide near infrared imaging in living cells with Yb3+ nano metal organic frameworks. *Proc. Natl. Acad. Sci. U.S.A.* **2013**, *110*, 17199-17204.

(42) Lu, K.; He, C.; Guo, N.; Chan, C.; Ni, K.; Weichselbaum, R. R.; Lin, W. Chlorin-Based Nanoscale Metal–Organic Framework Systemically Rejects Colorectal Cancers via Synergistic Photodynamic Therapy and Checkpoint Blockade Immunotherapy. *J. Am. Chem. Soc.* **2016**, *138*, 12502-12510.

(43) Lu, K.; He, C.; Lin, W. Nanoscale Metal–Organic Framework for Highly Effective Photodynamic Therapy of Resistant Head and Neck Cancer. *J. Am. Chem. Soc.* **2014**, *136*, 16712-16715.

(44) Lismont, M.; Dreesen, L.; Wuttke, S. Metal-Organic Framework Nanoparticles in Photodynamic Therapy: Current Status and Perspectives. *Adv. Funct. Mater.* **2017**, *27*, 1606314.

(45) Wu, M.-X.; Yang, Y.-W. Metal–Organic Framework (MOF)-Based Drug/Cargo Delivery and Cancer Therapy. *Adv. Mater.* **2017**, *29*, 1606134.

(46) Abánades Lázaro, I.; Haddad, S.; Sacca, S.; Orellana-Tavra, C.; Fairen-Jimenez, D.; Forgan, R. S. Selective Surface PEGylation of UiO-66 Nanoparticles for Enhanced Stability, Cell Uptake, and pH-Responsive Drug Delivery. *Chem.* **2017**, *2*, 561-578.

(47) Zhuang, J.; Kuo, C.-H.; Chou, L.-Y.; Liu, D.-Y.; Weerapana, E.; Tsung, C.-K. Optimized Metal–Organic-Framework Nanospheres for Drug Delivery: Evaluation of Small-Molecule Encapsulation. *ACS Nano.* **2014**, *8*, 2812-2819.

(48) Wang, L.; Han, Y.; Feng, X.; Zhou, J.; Qi, P.; Wang, B. Metal–organic frameworks for energy storage: Batteries and supercapacitors. *Coord. Chem. Rev.* **2016**, *307*, 361-381.

(49) Liang, Z.; Qu, C.; Guo, W.; Zou, R.; Xu, Q. Pristine Metal–Organic Frameworks and their Composites for Energy Storage and Conversion. *Adv. Mater.*, 1702891-n/a.

(50) Deria, P.; Mondloch, J. E.; Karagiaridi, O.; Bury, W.; Hupp, J. T.; Farha, O. K. Beyond post-synthesis modification: evolution of metal-organic frameworks via building block replacement. *Chem. Soc. Rev.* **2014**, *43*, 5896-5912.

(51) Noori, Y.; Akhbari, K. Post-synthetic ion-exchange process in nanoporous metal-organic frameworks; an effective way for modulating their structures and properties. *RSC Adv.* **2017**, *7*, 1782-1808.

(52) Kim, M.; Cahill, J. F.; Fei, H.; Prather, K. A.; Cohen, S. M. Postsynthetic Ligand and Cation Exchange in Robust Metal–Organic Frameworks. *J. Am. Chem. Soc.* **2012**, *134*, 18082-18088.

(53) Tanabe, K. K.; Cohen, S. M. Postsynthetic modification of metal-organic frameworks-a progress report. *Chem. Soc. Rev.* **2011**, *40*, 498-519.

(54) Garibay, S. J.; Wang, Z.; Tanabe, K. K.; Cohen, S. M. Postsynthetic Modification: A Versatile Approach Toward Multifunctional Metal-Organic Frameworks. *Inorg. Chem.* **2009**, *48*, 7341-7349.

(55) Li, B.; Zhang, Y.; Ma, D.; Li, L.; Li, G.; Li, G.; Shi, Z.; Feng, S. A strategy toward constructing a bifunctionalized MOF catalyst: post-synthetic modification of MOFs on organic ligands and coordinatively unsaturated metal sites. *Chem. Commun.* **2012**, *48*, 6151-6153.

(56) Li, B.; Zhang, Y.; Ma, D.; Ma, T.; Shi, Z.; Ma, S. Metal-Cation-Directed de Novo Assembly of a Functionalized Guest Molecule in the Nanospace of a Metal–Organic Framework. *J. Am. Chem. Soc.* **2014**, *136*, 1202-1205.

(57) Zhang, Z.; Zhang, L.; Wojtas, L.; Nugent, P.; Eddaoudi, M.; Zaworotko, M. J. Templated Synthesis, Postsynthetic Metal Exchange, and Properties of a Porphyrin-Encapsulating Metal–Organic Material. *J. Am. Chem. Soc.* **2012**, *134*, 924-927.

(58) Zhang, Z.; Wojtas, L.; Eddaoudi, M.; Zaworotko, M. J. Stepwise Transformation of the Molecular Building Blocks in a Porphyrin-Encapsulating Metal–Organic Material. *J. Am. Chem. Soc.* **2013**, *135*, 5982-5985.

(59) Wang, C.; deKrafft, K. E.; Lin, W. Pt Nanoparticles@Photoactive Metal–Organic Frameworks: Efficient Hydrogen Evolution via Synergistic Photoexcitation and Electron Injection. *J. Am. Chem. Soc.* **2012**, *134*, 7211-7214.

(60) Moon, H. R.; Lim, D.-W.; Suh, M. P. Fabrication of metal nanoparticles in metal-organic frameworks. *Chem. Soc. Rev.* **2013**, *42*, 1807-1824.

(61) Lian, X.; Fang, Y.; Joseph, E.; Wang, Q.; Li, J.; Banerjee, S.; Lollar, C.; Wang, X.; Zhou, H.-C. Enzyme-MOF (metal-organic framework) composites. *Chem. Soc. Rev.* **2017**, *46*, 3386-3401.

(62) Chen, Y.; Han, S.; Li, X.; Zhang, Z.; Ma, S. Why Does Enzyme Not Leach from Metal–Organic Frameworks (MOFs)? Unveiling the Interactions between an Enzyme Molecule and a MOF. *Inorg. Chem.* **2014**, *53*, 10006-10008.

(63) Xu, R.; Wang, Y.; Duan, X.; Lu, K.; Micheroni, D.; Hu, A.; Lin, W. Nanoscale Metal–Organic Frameworks for Ratiometric Oxygen Sensing in Live Cells. *J. Am. Chem. Soc.* **2016**, *138*, 2158-2161.

(64) Kong, X.-J.; Lin, Z.; Zhang, Z.-M.; Zhang, T.; Lin, W. Hierarchical Integration of Photosensitizing Metal–Organic Frameworks and Nickel-Containing Polyoxometalates for Efficient Visible-Light-Driven Hydrogen Evolution. *Angew. Chem. Int. Ed.* **2016**, *55*, 6411-6416.

(65) Zhang, Z.-M.; Zhang, T.; Wang, C.; Lin, Z.; Long, L.-S.; Lin, W. Photosensitizing Metal–Organic Framework Enabling Visible-Light-Driven Proton Reduction by a Wells–Dawson-Type Polyoxometalate. *J. Am. Chem. Soc.* **2015**, *137*, 3197-3200.

(66) He, C.; Lu, K.; Liu, D.; Lin, W. Nanoscale Metal–Organic Frameworks for the Co-Delivery of Cisplatin and Pooled siRNAs to Enhance Therapeutic Efficacy in Drug-Resistant Ovarian Cancer Cells. *J. Am. Chem. Soc.* **2014**, *136*, 5181-5184.

(67) Canivet, J.; Fateeva, A.; Guo, Y.; Coasne, B.; Farrusseng, D. Water adsorption in MOFs: fundamentals and applications. *Chem. Soc. Rev.* **2014**, *43*, 5594-5617.

(68) Gascon, J.; Kapteijn, F. Metal-Organic Framework Membranes—High Potential, Bright Future? *Angew. Chem. Int. Ed.* **2010**, *49*, 1530-1532.

(69) Zhang, L.; Hu, Y. H. Strong Effects of Higher-Valent Cations on the Structure of the Zeolitic Zn(2-methylimidazole)2 Framework (ZIF-8). *J. Phys. Chem. C.* **2011**, *115*, 7967-7971.

(70) Kizzie, A. C.; Wong-Foy, A. G.; Matzger, A. J. Effect of Humidity on the Performance of Microporous Coordination Polymers as Adsorbents for CO2 Capture. *Langmuir.* **2011**, *27*, 6368-6373.

(71) Cavka, J. H.; Jakobsen, S.; Olsbye, U.; Guillou, N.; Lamberti, C.; Bordiga, S.; Lillerud, K. P. A New Zirconium Inorganic Building Brick Forming Metal Organic Frameworks with Exceptional Stability. *J. Am. Chem. Soc.* **2008**, *130*, 13850-13851.

(72) Kandiah, M.; Nilsen, M. H.; Usseglio, S.; Jakobsen, S.; Olsbye, U.; Tilset, M.; Larabi, C.; Quadrelli, E. A.; Bonino, F.; Lillerud, K. P. Synthesis and Stability of Tagged UiO-66 Zr-MOFs. *Chem. Mater.* **2010**, *22*, 6632-6640.

(73) DeCoste, J. B.; Peterson, G. W.; Jasuja, H.; Glover, T. G.; Huang, Y.-g.; Walton, K. S. Stability and degradation mechanisms of metal-organic frameworks containing the $Zr_6O_4(OH)_4$ secondary building unit. *J. Mater. Chem. A.* **2013**, *1*, 5642-5650.

(74) Liu, X.; Demir, N. K.; Wu, Z.; Li, K. Highly Water-Stable Zirconium Metal–Organic Framework UiO-66 Membranes Supported on Alumina Hollow Fibers for Desalination. *J. Am. Chem. Soc.* **2015**, *137*, 6999-7002.

(75) Valenzano, L.; Civalleri, B.; Chavan, S.; Bordiga, S.; Nilsen, M. H.; Jakobsen, S.; Lillerud, K. P.; Lamberti, C. Disclosing the Complex Structure of UiO-66 Metal Organic Framework: A Synergic Combination of Experiment and Theory. *Chem. Mater.* **2011**, *23*, 1700-1718.

(76) Pearson, R. G. Hard and Soft Acids and Bases. *J. Am. Chem. Soc.* **1963**, *85*, 3533-3539.

(77) Klet, R. C.; Liu, Y.; Wang, T. C.; Hupp, J. T.; Farha, O. K. Evaluation of Bronsted acidity and proton topology in Zr- and Hf-based metal-organic frameworks using potentiometric acid-base titration. *J. Mater. Chem. A.* **2016**, *4*, 1479-1485.

(78) Furukawa, H.; Gándara, F.; Zhang, Y.-B.; Jiang, J.; Queen, W. L.; Hudson, M. R.; Yaghi, O. M. Water Adsorption in Porous Metal–Organic Frameworks and Related Materials. *J. Am. Chem. Soc.* **2014**, *136*, 4369-4381.

(79) Jiang, H.-L.; Feng, D.; Liu, T.-F.; Li, J.-R.; Zhou, H.-C. Pore Surface Engineering with Controlled Loadings of Functional Groups via Click Chemistry in Highly Stable Metal–Organic Frameworks. *J. Am. Chem. Soc.* **2012**, *134*, 14690-14693.

(80) Yuan, S.; Lu, W.; Chen, Y.-P.; Zhang, Q.; Liu, T.-F.; Feng, D.; Wang, X.; Qin, J.; Zhou, H.-C. Sequential Linker Installation: Precise Placement of Functional Groups in Multivariate Metal–Organic Frameworks. *J. Am. Chem. Soc.* **2015**, *137*, 3177-3180.

(81) Bon, V.; Senkovska, I.; Baburin, I. A.; Kaskel, S. Zr- and Hf-Based Metal–Organic Frameworks: Tracking Down the Polymorphism. *Cryst. Growth Des.* **2013**, *13*, 1231-1237.

(82) Bon, V.; Senkovskyy, V.; Senkovska, I.; Kaskel, S. Zr(iv) and Hf(iv) based metal-organic frameworks with reo-topology. *Chem. Commun.* **2012**, *48*, 8407-8409.

(83) Feng, D.; Chung, W.-C.; Wei, Z.; Gu, Z.-Y.; Jiang, H.-L.; Chen, Y.-P.; Darensbourg, D. J.; Zhou, H.-C. Construction of Ultrastable Porphyrin Zr Metal–Organic Frameworks through Linker Elimination. *J. Am. Chem. Soc.* **2013**, *135*, 17105-17110.

(84) Feng, D.; Jiang, H.-L.; Chen, Y.-P.; Gu, Z.-Y.; Wei, Z.; Zhou, H.-C. Metal–Organic Frameworks Based on Previously Unknown Zr_8/Hf_8 Cubic Clusters. *Inorg. Chem.* **2013**, *52*, 12661-12667.

(85) Cliffe, M. J.; Castillo-Martínez, E.; Wu, Y.; Lee, J.; Forse, A. C.; Firth, F. C. N.; Moghadam, P. Z.; Fairen-Jimenez, D.; Gaultois, M. W.; Hill, J. A.; Magdysyuk, O. V.; Slater, B.; Goodwin, A. L.; Grey, C. P. Metal–Organic Nanosheets Formed via Defect-Mediated Transformation of a Hafnium Metal–Organic Framework. *J. Am. Chem. Soc.* **2017**, *139*, 5397-5404.

(86) Dai, R.; Peng, F.; Ji, P.; Lu, K.; Wang, C.; Sun, J.; Lin, W. Electron Crystallography Reveals Atomic Structures of Metal–Organic Nanoplates with $M_{12}(\mu_3\text{-O})_8(\mu_3\text{-OH})_8(\mu_2\text{-OH})_6$ (M = Zr, Hf) Secondary Building Units. *Inorg. Chem.* **2017**, *56*, 8128-8134.

(87) Yang, W.; Feng, J.; Song, S.; Zhang, H. Microwave-Assisted Modular Fabrication of Nanoscale Luminescent Metal-Organic Framework for Molecular Sensing. *ChemPhysChem.* **2012**, *13*, 2734-2738.

(88) Suresh, V. M.; Chatterjee, S.; Modak, R.; Tiwari, V.; Patel, A. B.; Kundu, T. K.; Maji, T. K. Oligo(p-phenyleneethynylene)-Derived Porous Luminescent Nanoscale Coordination Polymer of GdIII: Bimodal Imaging and Nitroaromatic Sensing. *J. Phys. Chem. C.* **2014**, *118*, 12241-12249.

(89) Wu, P.; Wang, J.; He, C.; Zhang, X.; Wang, Y.; Liu, T.; Duan, C. Luminescent Metal-Organic Frameworks for Selectively Sensing Nitric Oxide in an Aqueous Solution and in Living Cells. *Adv. Funct. Mater.* **2012**, *22*, 1698-1703.

(90) He, C.; Lu, K.; Lin, W. Nanoscale Metal–Organic Frameworks for Real-Time Intracellular pH Sensing in Live Cells. *J. Am. Chem. Soc.* **2014**, *136*, 12253-12256.

(91) Taylor, K. M. L.; Rieter, W. J.; Lin, W. Manganese-Based Nanoscale Metal−Organic Frameworks for Magnetic Resonance Imaging. *J. Am. Chem. Soc.* **2008**, *130*, 14358-14359.

(92) deKrafft, K. E.; Xie, Z.; Cao, G.; Tran, S.; Ma, L.; Zhou, O. Z.; Lin, W. Iodinated Nanoscale Coordination Polymers as Potential Contrast Agents for Computed Tomography. *Angew. Chem. Int. Ed.* **2009**, *48*, 9901-9904.

(93) Hatakeyama, W.; Sanchez, T. J.; Rowe, M. D.; Serkova, N. J.; Liberatore, M. W.; Boyes, S. G. Synthesis of Gadolinium Nanoscale Metal−Organic Framework with Hydrotropes: Manipulation of Particle Size and Magnetic Resonance Imaging Capability. *ACS Appl. Mater. Interfaces.* **2011**, *3*, 1502-1510.

(94) McKinlay, A. C.; Morris, R. E.; Horcajada, P.; Férey, G.; Gref, R.; Couvreur, P.; Serre, C. BioMOFs: Metal–Organic Frameworks for Biological and Medical Applications. *Angew. Chem. Int. Ed.* **2010**, *49*, 6260-6266.

(95) Ikeda, E. Cellular response to tissue hypoxia and its involvement in disease progression. *Pathology International.* **2005**, *55*, 603-610.

(96) Harris, A. L. Hypoxia — a key regulatory factor in tumour growth. *Nat. Rev. Cancer.* **2002**, *2*, 38.

(97) Höckel, M.; Schlenger, K.; Aral, B.; Mitze, M.; Schäffer, U.; Vaupel, P. Association between Tumor Hypoxia and Malignant Progression in Advanced Cancer of the Uterine Cervix. *Cancer Res.* **1996**, *56*, 4509.

(98) Gatenby, R. A.; Kessler, H. B.; Rosenblum, J. S.; Coia, L. R.; Moldofsky, P. J.; Hartz, W. H.; Broder, G. J. Oxygen distribution in squamous cell carcinoma metastases and its relationship to outcome of radiation therapy. *Int. J. Radiat. Oncol. Biol. Phys.* **1988**, *14*, 831-838.

(99) Hoogsteen, I. J.; Lok, J.; Marres, H. A. M.; Takes, R. P.; Rijken, P. F. J. W.; van der Kogel, A. J.; Kaanders, J. H. A. M. Hypoxia in larynx carcinomas assessed by pimonidazole binding and the value of CA-IX and vascularity as surrogate markers of hypoxia. *Eur. J. Cancer.* **2009**, *45*, 2906-2914.

(100) Mees, G.; Dierckx, R.; Vangestel, C.; Van de Wiele, C. Molecular imaging of hypoxia with radiolabelled agents. *Eur. J. Nucl. Med. Mol. Imaging.* **2009**, *36*, 1674-1686.

(101) Cooper, R. A.; Carrington, B. M.; Loncaster, J. A.; Todd, S. M.; Davidson, S. E.; Logue, J. P.; Luthra, A. D.; Jones, A. P.; Stratford, I.; Hunter, R. D.; West, C. M. L. Tumour oxygenation levels correlate with dynamic contrast-enhanced magnetic resonance imaging parameters in carcinoma of the cervix. *Radiotherapy and Oncology.* **2000**, *57*, 53-59.

(102) Padhani, A. R.; Krohn, K. A.; Lewis, J. S.; Alber, M. Imaging oxygenation of human tumours. *Eur. Radiol.* **2007**, *17*, 861-872.

(103) Zhang, G.; Palmer, G. M.; Dewhirst, M. W.; Fraser, C. L. A dual-emissive-materials design concept enables tumour hypoxia imaging. *Nat. Mater.* **2009**, *8*, 747.

(104) Spencer, J. A.; Ferraro, F.; Roussakis, E.; Klein, A.; Wu, J.; Runnels, J. M.; Zaher, W.; Mortensen, L. J.; Alt, C.; Turcotte, R.; Yusuf, R.; Côté, D.; Vinogradov, S. A.; Scadden, D. T.; Lin, C. P. Direct measurement of local oxygen concentration in the bone marrow of live animals. *Nature.* **2014**, *508*, 269.

(105) Wu, C.; Bull, B.; Christensen, K.; McNeill, J. Ratiometric Single-Nanoparticle Oxygen Sensors for Biological Imaging. *Angew. Chem. Int. Ed.* **2009**, *48*, 2741-2745.

(106) Wang, X.-d.; Stolwijk, J. A.; Lang, T.; Sperber, M.; Meier, R. J.; Wegener, J.; Wolfbeis, O. S. Ultra-Small, Highly Stable, and Sensitive Dual Nanosensors for Imaging Intracellular Oxygen and pH in Cytosol. *J. Am. Chem. Soc.* **2012**, *134*, 17011-17014.

(107) Zhao, Q.; Zhou, X.; Cao, T.; Zhang, K. Y.; Yang, L.; Liu, S.; Liang, H.; Yang, H.; Li, F.; Huang, W. Fluorescent/phosphorescent dual-emissive conjugated polymer dots for hypoxia bioimaging. *Chemical Science.* **2015**, *6*, 1825-1831.

(108) Yoshihara, T.; Yamaguchi, Y.; Hosaka, M.; Takeuchi, T.; Tobita, S. Ratiometric Molecular Sensor for Monitoring Oxygen Levels in Living Cells. *Angew. Chem. Int. Ed.* **2012**, *51*, 4148-4151.

(109) Feng, Y.; Cheng, J.; Zhou, L.; Zhou, X.; Xiang, H. Ratiometric optical oxygen sensing: a review in respect of material design. *Analyst.* **2012**, *137*, 4885-4901.

(110) Koo, Y.-E. L.; Cao, Y.; Kopelman, R.; Koo, S. M.; Brasuel, M.; Philbert, M. A. Real-Time Measurements of Dissolved Oxygen Inside Live Cells by Organically Modified Silicate Fluorescent Nanosensors. *Anal. Chem.* **2004**, *76*, 2498-2505.

(111) Chojnacki, P.; Mistlberger, G.; Klimant, I. Separable Magnetic Sensors for the Optical Determination of Oxygen. *Angew. Chem. Int. Ed.* **2007**, *46*, 8850-8853.

(112) Amelia, M.; Lavie-Cambot, A.; McClenaghan, N. D.; Credi, A. A ratiometric luminescent oxygen sensor based on a chemically functionalized quantum dot. *Chem. Commun.* **2011**, *47*, 325-327.

(113) Coppeta, J.; Rogers, C. Dual emission laser induced fluorescence for direct planar scalar behavior measurements. *Exp. Fluids.* **1998**, *25*, 1-15.

(114) Valeur, B.; Berberan-Santos, M. N. *Molecular fluorescence: principles and applications*; John Wiley & Sons, 2012.

(115) Turro, N. J.; Ramamurthy, V.; Scaiano, J. C.; Wiley Online Library: 2012.

(116) Zhang, G.; Palmer, G. M.; Dewhirst, M. W.; Fraser, C. L. A dual-emissive-materials design concept enables tumour hypoxia imaging. *Nature materials.* **2009**, *8*, 747-751.

(117) Zhang, G.; Chen, J.; Payne, S. J.; Kooi, S. E.; Demas, J.; Fraser, C. L. Multi-emissive difluoroboron dibenzoylmethane polylactide exhibiting intense fluorescence and oxygen-sensitive room-temperature phosphorescence. *J. Am. Chem. Soc.* **2007**, *129*, 8942-8943.

(118) Carreau, A.; Hafny-Rahbi, B. E.; Matejuk, A.; Grillon, C.; Kieda, C. Why is the partial oxygen pressure of human tissues a crucial parameter? Small molecules and hypoxia. *J. Cell. Mol. Med.* **2011**, *15*, 1239-1253.

(119) Finikova, O. S.; Lebedev, A. Y.; Aprelev, A.; Troxler, T.; Gao, F.; Garnacho, C.; Muro, S.; Hochstrasser, R. M.; Vinogradov, S. A. Oxygen microscopy by two-photon-excited phosphorescence. *ChemPhysChem.* **2008**, *9*, 1673-1679.

(120) Magde, D.; Rojas Gail, E.; Seybold Paul, G. Solvent Dependence of the Fluorescence Lifetimes of Xanthene Dyes. *Photochem. Photobiol.* **2008**, *70*, 737-744.

CHAPTER 2. Metal-Organic Layers Catalyze Photoreactions without Pore Size and Diffusion Limitations

2.1 Introduction

By harvesting sunlight to drive thermodynamically uphill reactions, photosynthesis has provided food and energy for the human kind. Chemists have sought to use light as an inexpensive, renewable, and environmentally friendly means to drive photochemical reactions for over a century.[1] Photocatalysis is now used in organic synthesis with high atom efficiency and product selectivity[2] via shifting apparent thermodynamic equilibria of chemical reactions and allowing difficult reactions to be carried out under mild conditions.[3] Photocatalysts are often required in visible-light-driven organic reactions as the majority of organic substrates do not appreciably absorb in the visible spectrum.[4] As an example of the mostly studied photocatalysts,[2,5] $[Ru(bpy)_3]^{2+}$ exhibits high absorption extinction coefficient, good solubility, adequate chemical stability, and long excited-state lifetime, enabling its application in a variety of photocatalytic organic reactions, such as [2+2] cycloaddition,[6] tin-free dehalogenation,[7] thio-ene reactions,[8] olefin epoxidation,[9] bimetallic photocatalysis,[10,11] and asymmetric photocatalysis.[12,13] However, $Ru(bpy)_3^{2+}$ and other homogeneous precious metal-based photocatalysts are difficult to separate from their reaction mixtures for reuse, spurring our interest in heterogenizing molecular photocatalysts to enhance their catalytic efficiencies and to facilitate their recycle and reuse.

Immobilizing homogeneous metal photocatalysts on solid supports, such as graphenes,[14,15] carbon nanotubes,[16] and silicas[17,18] has been extensively explored with the goal of recycling and reusing these valuable catalysts. However, such a strategy can lead to non-uniform distribution of catalysts and cannot prevent self-quenching that can induce loss of activity of the photocatalysts.

To address this issue, our group devoted effort to incorporate polypyridyl Ru(II) complexes into UiO-67 framework via a mixed-ligand synthesis method.[19] The resulted photoactive MOF exhibited good yields and reusability in catalyzing Aza-Henry reactions, oxidative coupling of amines and oxidation sulfides. Similar strategies have been used to construct $Ru(bpy)_3^{2+}$-containing MOFs for aerobic oxidation of arylboronic acids,[20] trifluoroethylation of styrenes[21], and hydrogen evolution reactions.[22] Besides $Ru(bpy)_3^{2+}$, there are also reports of heterogenizing other molecular photocatalysts into MOFs,[23-26] but overall research in this field remains sparse. In many photoreactions, photocatalysts enter excited states upon light irradiation and then react with organic substrates through single-electron transfer (SET) processes (**Figure 2-1**). The resultant radical intermediates must react with their partners within their typically short lifetimes to afford desired products. However, diffusion through nanometer-sized MOF channels is highly restricted,[27-30] which reduces the collision probability between reactive intermediates and their partners in photoreactions, presenting a significant hurdle for designing efficient MOF-based photocatalysts (**Figure 2-2a**).

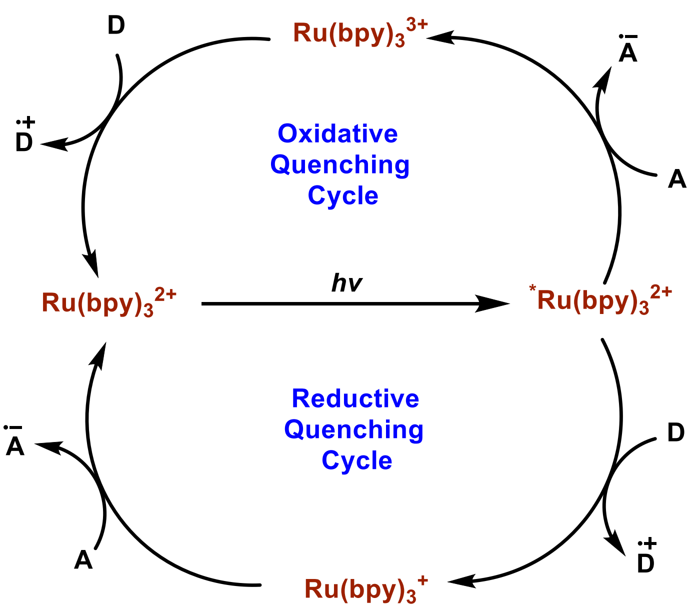

Figure 2-1. Oxidative and Reductive Quenching Cycle of $Ru(bpy)_3^{2+}$.

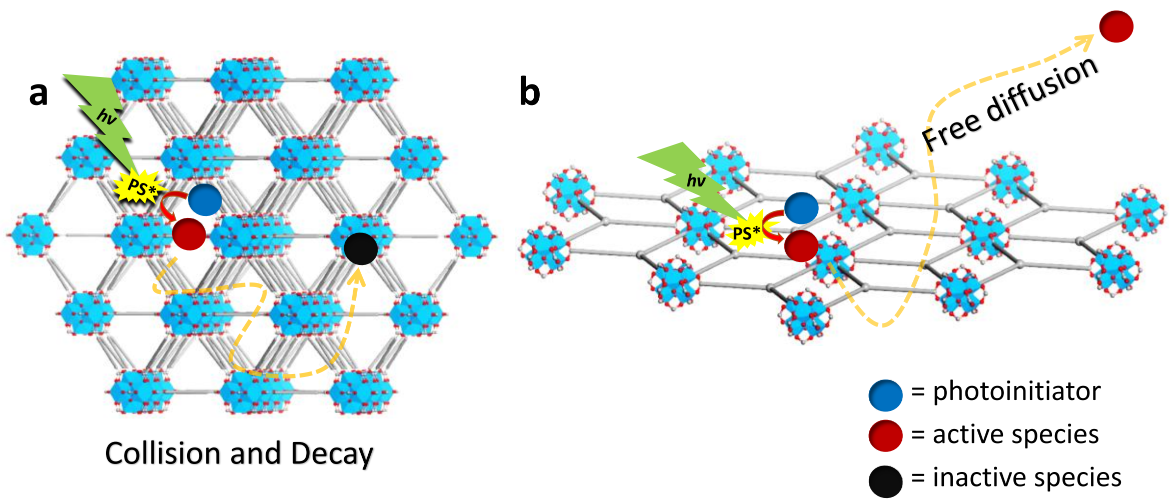

Figure 2-2. Restricted vs. free diffusion of reactive species in MOFs (a) vs. MOLs (b).

Metal-organic layers (MOLs), a subset of MOFs, are two-dimensional self-supporting monolayer nanosheets with one dimension reduced to a monolayer thickness of 1-2 nm. The first reported MOL, $Hf_6(\mu_3\text{-}O)_4(\mu_3\text{-}OH)_4(HCO_2)_6(BTB)_2$, comprises 12-connected Hf_6 clusters, BTB [BTB = benzene 1,3,5-tri(benzoate)] ligands and HCOOH as caping units, forming infinite 3,6-connected 2D network with kagome dual (kgd) topology.[31] MOLs inherit the heterogeneous, crystalline, and single-site solid-state nature of MOFs, and have been reported as efficient catalysts in a few cases.[31-33] Different from MOFs, MOLs are free from pore size limitations and diffusion restriction due to their unique 2D geometry (**Figure 2-2b**), which are especially valuable merits in photoreactions. In this chapter, we successfully synthesized RuBPY-MOL by incorporation of $Ru(bpy)_3^{2+}$ into MOLs. RuBPY-MOL exhibited high photocatalytic activities for [2+2] cycloadditions of bis(enones) and Meerwein additions between aryl diazonium salts, styrenes and nitriles under visible light irradiation. In contrast, the corresponding MOF catalyst, RuUiO-67 containing same $Ru(bpy)_3^{2+}$ species, failed in these photoreactions, due to either pore size limitation or restricted diffusion of reactive intermediates.

2.2 Results and Discussion

2.2.1 Synthesis and Characterization of BPY-MOL and RuBPY-MOL

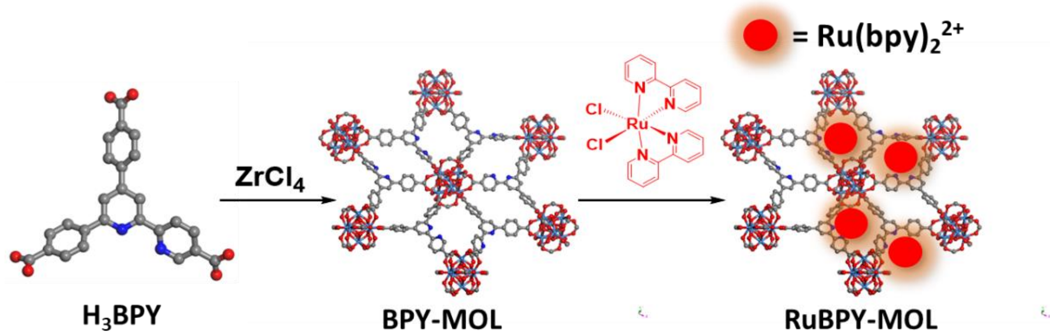

Scheme 2-1. Synthetic scheme of BPY-MOL and RuBPY-MOL.

RuBPY-MOL was synthesized according to **Scheme 2-1**. First, 4',6'-bis(4-benzoic acid)-(2,2'-bipyridine)-5-carboxylic acid (H_3BPY) was mixed with $ZrCl_4$ in a mixed solvent of DMF/H_2O/HCOOH and heated at 120 ˚C to afford BPY-MOL. BPY-MOL showed a wrinkled nanosheet morphology by TEM and kgd topology by powder X-ray diffraction PXRD (**Figure 2-3a**, **2-3b**). BPY-MOL was then was treated with $Ru(bpy)_3Cl_2$ in different solvents at different temperatures. By monitoring the metalation with UV-vis spectroscopy using the characteristic peak at 460 nm corresponding to $Ru(bpy)_3^{2+}$ (**Figure 2-4**), we determined that the metalation was the most facile with pure EtOH as solvent. The sample from pure ethanol, RuBPY-3, was digested and subjected to ICP-MS measurement, giving a Ru/Zr ratio of 1:4.2, corresponding to 71% metalation. RuBPY-MOL thus has an empirical formula of $Zr_6(\mu_3\text{-}O)_4(\mu_3\text{-}OH)_4(HCO_2)_6(BPY)_2\text{-}[Ru(bpy)_2Cl_2]_{1.42}$. TEM and PXRD indicated that the MOL morphology and topology were retained after postsynthetic metalation (Figure **2-3a**, **2-3c**, **2-3d**).

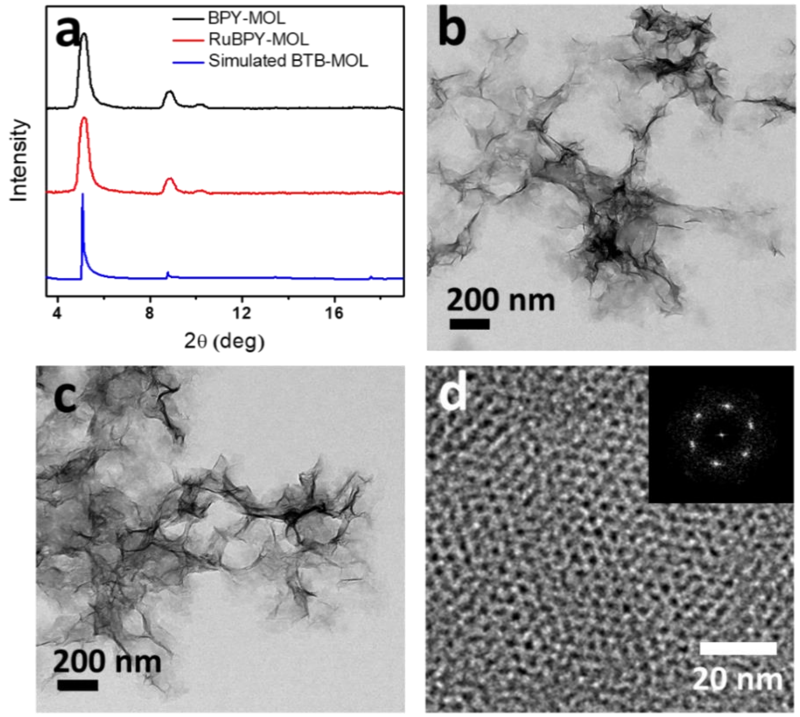

Figure 2-3. Structure and morphology of BPY-MOL and RuBPY-MOL. (a) PXRD patterns of RBPY-MOL and RuBPY-MOL. TEM images of (b) BPY-MOL and (c) RuBPY-MOL. (d) high-resolution TEM images of RuBPY-MOL. Inset: fast Fourier transform patterns of RuBPY-MOL.

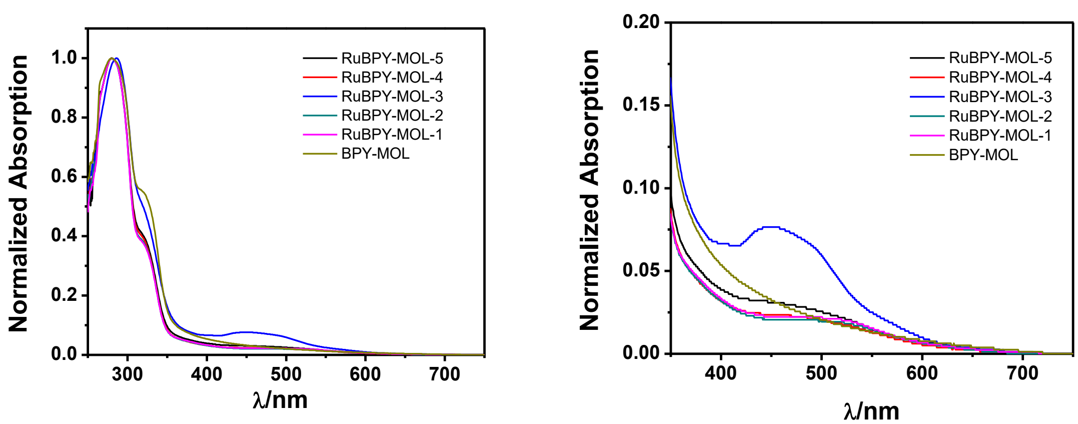

Figure 2-4. Left, UV-vis spectra of RuBPY-MOL synthesized in different solvents and at different temperatures. RuBPY-MOL-1: DMF, 120 °C; RuBPY-MOL-2: DMF, 100 °C; RuBPY-MOL-3:

EtOH, 80 °C; RuBPY-MOL-4: DMF/EtOH = 1:1 v/v, 100 °C; RuBPY-MOL-5: DMF/EtOH = 1:1 v/v, 120 °C. Right, zoomed-in regions of the UV-Vis spectra shown on the left.

2.2.2 Synthesis and Characterization of RuUiO-67

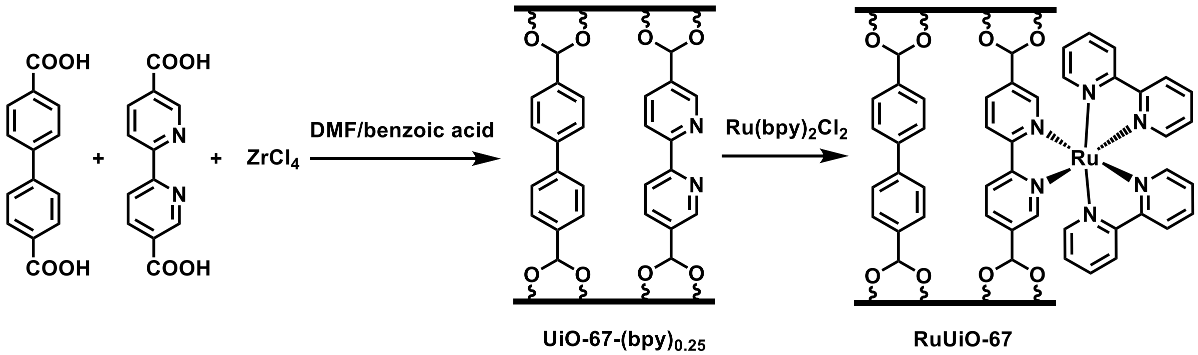

Scheme 2-2. Synthetic scheme of RuUiO-67.

RuUiO-67 was synthesized according to previous report.[20] Briefly, biphenyldicarboxylic acid (H_2bpdc) and 2,2'-bipyridine-5,5'-dicarboxylic acid (H_2bpydc) were mixed with $ZrCl_4$ and benzoic acid in DMF and heated at 120 °C for 24h. The resulted UiO-67-(bpy)$_{0.25}$ was then treated with $Ru(bpy)_2Cl_2$ in EtOH/H_2O, affording RuUiO-67. The PXRD of RuUiO-67 shown in **Figure 2-5** is similar to previously reported.[20]

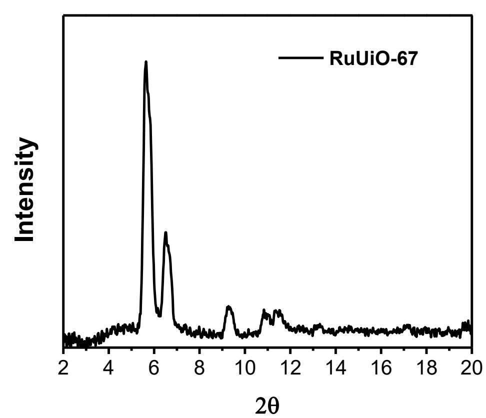

Figure 2-5. PXRD of RuUiO-67.

The composition of RuUiO-67 was determined by [1]HNMR analysis of digested samples, shown in **Figure 2-6**. The ratio of bpdc : bpydc : Rubpydc was 1:0.18:0.22, suggesting 55% metalation relative to bpy sites, corresponding the presence of ~16% $Ru(bpy)_3$ relative to total linkers. The empirical formula is $Zr_6O_4(OH)_4(bpdc)_{4.29}(bpydc)_{0.77}(Rubpydc)_{0.94}$. Nitrogen sorption and thermalgravimetric analysis were also performed and representative results are summarized in **Figure 2-7** and **Figure 2-8**.

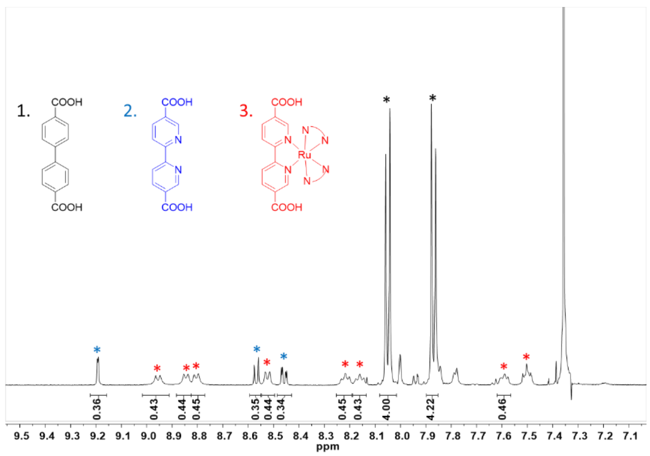

Figure 2-6. ^{1}HNMR of digested RuUiO-67 samples.

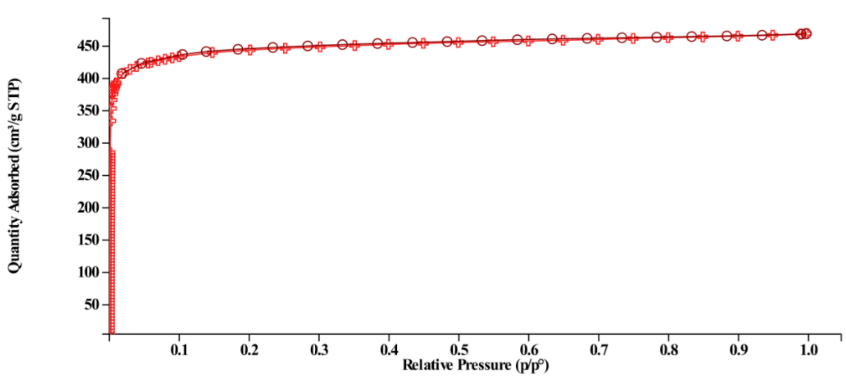

Figure 2-7. Nitrogen sorption isotherms of RuUiO-67 at 77 K (○: adsorption, +: desorption), which gives a calculated BET surface area of 1755 m^2/g.

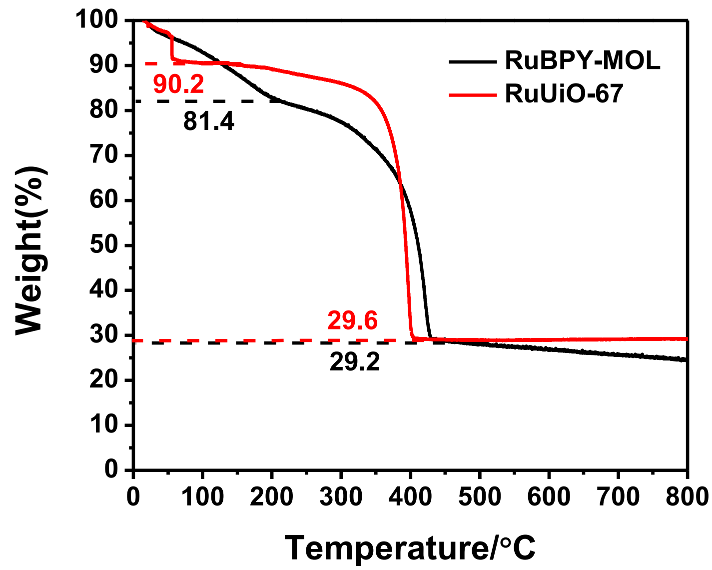

Figure 2-8. TGA curves of RuUiO-67 (red) and RuBPY-MOL (black). The first weight losses (9.8% and 18.6%) in the 25-200 ˚C temperature range correspond to removal of residual solvents. The second weight losses (67.2% and 64.1%) in the 200-800 ˚C temperature range correspond to decomposition of $Zr_6O_4(OH)_4(bpdc)_{4.29}(bpydc)_{0.77}(Rubpydc)_{0.94}$ to ZrO_2 and Ru_2O_3 (calculated: 65.9%), and decomposition of $Zr_6(\mu_3\text{-}O)_4(\mu_3\text{-}OH)_4(HCO_2)_6(BPY)_2[Ru(bpy)_2Cl_2]_{1.42}$ to ZrO_2 and Ru_2O_3 (calculated: 62.4%).

2.2.3 RuBPY-MOL Catalyzed Intramolecular [2+2] Cycloadditions of Bis(enones)

We investigated photocatalytic activities of RuBPY-MOL in several prototypical photoreactions. Intramolecular [2+2] Cycloaddition of bis(enones)[6] was studied first and the results are summarized in **Table 2-1**. Bis(enone) **1a** was irradiated with 410 nm LED for 3 h in the presence of RuBPY-MOL, $LiBF_4$, and diisopropylethylamine (DIPEA) to afford the *meso* diastereomer of the cyclobutane bicyclic dione **2a** in 82% yield and good selectivity (entry 2). The catalytic performance of RuBPY-MOL was comparable to that of homogeneous $Ru(bpy)_3^{2+}$ (entry 1). In contrast, the UiO-67 MOF with doped $Ru(bpy)_3^{2+}$, RuUiO-67, failed to promote [2+2] cycloaddition of **1a** in 8 h (entry 3). No product was observed when BPY-MOL was used, indicating the photocatalytic role of $Ru(bpy)_3^{2+}$ species (entry 4). Furthermore, the [2+2] cycloaddition did not proceed in the dark (entry 5), demonstrating the involvement of light-driven processes.

Table 2-1. [2+2] intramolecular cycloaddition of bis(enone) **1a**.[a]

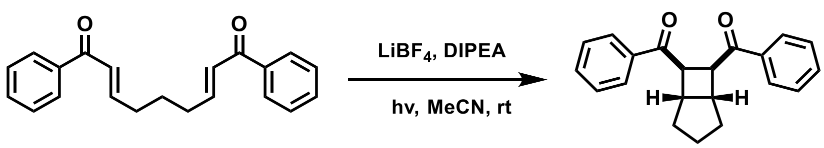

Entry	Catalyst	Yield
1	$Ru(bpy)_3Cl_2 \cdot 6H_2O$	88%
2	RuBPY-MOL	82%
3	RuUiO-67	n.r.
4	BPY-MOL	n.r.
5[a]	RuBPY-MOL	n.r.

[a]Reaction carried without light. n.r.: not reacted.

To test the heterogeneity of RuBPY-MOL, we determined the leaching of Ru and Zr into the supernatant after photocatalytic cycloaddition of **1a** for 3h. ICP-MS analysis showed negligible leaching of Ru and Zr into the supernatant (2.3% and 0.3% for Ru and Zr, respectively). RuBPY-MOL was also readily recovered via centrifugation and used in three consecutive runs of photocatalytic cycloaddition of **1a** without loss of activity or diastereoselectivity (**Table 2-2**).

Furthermore, PXRD studies showed that the MOL diffraction peaks were retained after photocatalysis (**Figure 2-9**).

Table 2-2. Reuse of RuBPY-MOL in [2+2] cycloaddition of **1a**

Entry	Yield	dr
1^{st} run	88%	>10:1
2^{nd} run	80%	>10:1
3^{rd} run	82%	>10:1

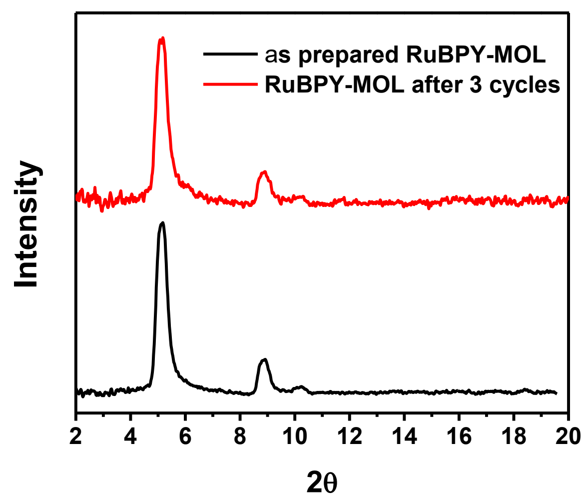

Figure 2-9. PXRD pattern of RuBPY-MOL before and after three consecutive cycles of [2+2] cycloaddition reaction.

We further investigated the substrate scope for RuBPY-MOL catalyzed cycloaddition reactions (**Table 2-3**). In all bis(enones) studied (**1a**-**1e**), RuBPY-MOL afforded [2+2] cycloaddition products in 73-92% yields. In these examples, RuUiO-67 gave <10% desired products. Electron-rich bis(enones) required longer reaction times than electron-deficient bis(enones). RuBPY-MOL also catalyzed [2+2] cycloaddition of a large substrate, *t*-butyl phenyl bis(enone) (entry 7), albeit in a longer reaction time (12 h).

Table 2-3. [2+2] intramolecular cycloadditions of bis(enones) with RuBPY-MOL and RuUiO-67 as photocatalysts[a]

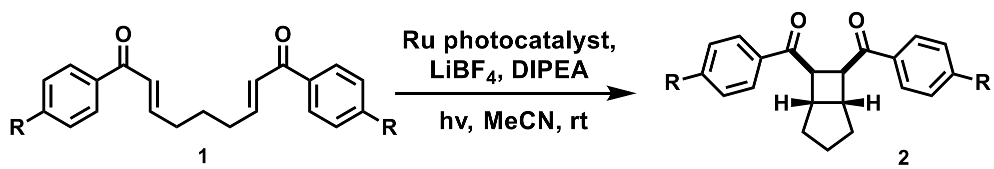

R = H, 1a, 2a; = Cl, 1b, 2b; = Br, 1c, 2c; = *t*Bu, 1d, 2d; = OMe, 1e, 2e

Entry	R	Catalyst	Time	Yield[b]	dr[c]
1	H	RuBPY-MOL	3h	82%	>10:1
2		RuUiO67	8h	n.r.	--
3	Cl	RuBPY-MOL	3h	86%	>10:1
4		RuUiO67	3h	9%	--
5	Br	RuBPY-MOL	3h	92%	>10:1
6		RuUiO67	3h	n.r.	--
7	*t*Bu	RuBPY-MOL	12h	79%	10:1
8		RuUiO67	12h	<10%	--
9	OMe	RuBPY-MOL	6h	73%	8:1
10		RuUiO67	6h	<10%	--

[a]Reaction conditions: 1 mol% RuBPY-MOL or RuUiO-67, 2 eq. DIPEA, 2 eq. LiBF4, 6 mW/cm2 410 nm LED, MeCN (0.1M). [b]Isolated yields. [c]Diastereomer ratios determined by NMR.

2.2.4 RuBPY-MOL Catalyzed Reductive Cyclizations of Bis(enones)

We next examined the use of MOL and MOF photocatalysts in reductive cyclization of bis(enones) to afford monocyclic dione products with formic acid in place of $LiBF_4$.[34] The switch of reaction pathways is believed to arise from different reactivities of neutral radical vs radical anion intermediates.[34] When photocatalytic reductive cyclization of bis(enones) **1a-1e** were carried out in the presence of RuBPY-MOL or RuUiO-67, Products **3a-3e** were obtained in similarly high yields: 75-93% for RuBPY-MOL and 68-85% for RuUiO-67 (**Table 2-4**). In all cases, racemic mixtures of (*R*,*R*)- and (*S*,*S*)-cyclopentyl diones were obtained without the formation of the *meso* diastereomer. Similar to [2+2] cycloaddition reactions, electron-deficient enones reacted faster than electron-rich enones and the large enone substrate with *t*-butyl groups needed a longer reaction time.

Table 2-4. Reductive cyclizations of bis(enones)[a]

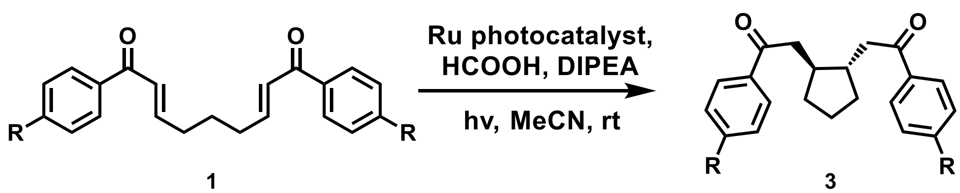

Entry	R	Catalyst	Time	Yield[b]	dr[c]
1	H	RuBPY-MOL	6h	80%	>10:1
2		RuUiO67	6h	82%	>10:1
3	Cl	RuBPY-MOL	3h	85%	>10:1
4		RuUiO67	3h	83%	>10:1
5	Br	RuBPY-MOL	3h	88%	>10:1
6		RuUiO67	3h	83%	>10:1
7	*t*Bu	RuBPY-MOL	12h	93%	>10:1
8		RuUiO67	12h	85%	>10:1
9	OMe	RuBPY-MOL	6h	75%	>10:1
10		RuUiO67	6h	68%	>10:1

[a]Reaction conditions: 2.5 mol% RuBPY-MOL or RuUiO-67, 10 eq. DIPEA, 5eq. HCOOH, 6 mW/cm^2 410 nm LED. [b]Isolated yields. [c]Diastereomer ratios determined by NMR.

The two types of intramolecular photoreactions worked similarly for RuBPY-MOL but showed drastically different reactivities for RuUiO-67. We used molecular mechanics (UFF, **Figure 2-10, 2-11**) to model the products **2a** and **3a** from the two photocyclization reactions. Product **2a** from the [2+2] cycloaddition reaction favors a conformation with the two phenyl groups extending like wings, leading to a triangular configuration with approximate dimensions of ~12.16 × 8.82 Å. In comparison, product **3a** from the reductive cyclization reaction adopts a compact conformation of 10.17 × 5.48 Å in dimensions with the two phenyl rings paralleled to each other in a face-to-face manner. RuUiO-67 has a Ru loading of 16% relative to the dicarboxylate linkers according to NMR analysis (**Figure 2-6**), corresponding an approximate 1:1 ratio between the $Ru(bpy)_3^{2+}$ moiety and the octahedral pore. Most octahedral pores in RuUiO-67 are thus occupied by $Ru(bpy)_3^{2+}$, leaving tetrahedral pores to accommodate bis(enone) substrates. The tetrahedral pore of UiO-67 was reported to be 11.5~12 Å,[35-37] in between the sizes of **2a** and **3a**. Therefore, **3a** but not **2a** can fit in the UiO-67 tetrahedral pores (**Figure 2-10c, 2-11c**). **3a** can also pass through the triangular window of UiO-67 (**Figure 2-11d**) while **2a** is blocked (**Figure 2-10d**). As a result, reductive cyclization but not [2+2] cycloaddition can occur in tetrahedral pores of RuUiO-67. Moreover, as both intramolecular photoreactions have similar initiation mechanism by $Ru(bpy)_3^{2+}$, diffusion cannot be a limiting factor. The different reactivities are a result of pore size limitation of MOF photocatalysts which does not apply to MOLs.

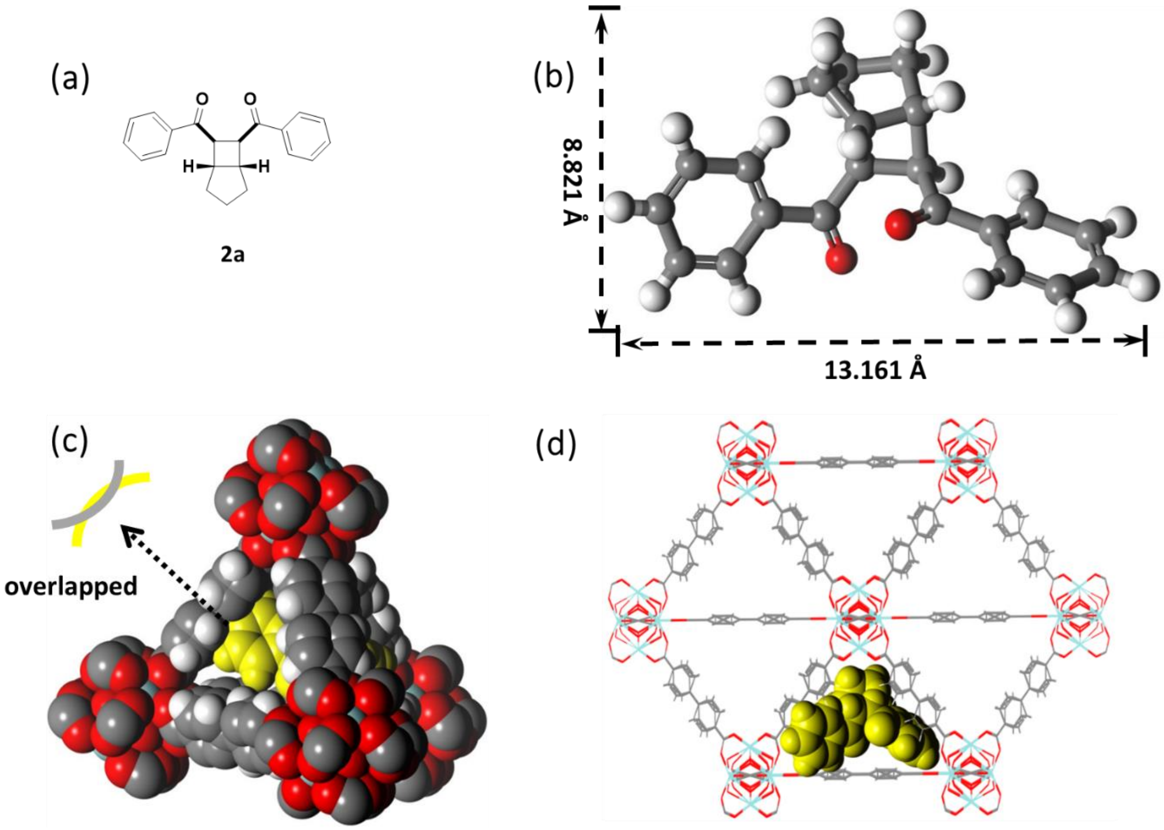

Figure 2-10. Structure model of [2+2] cycloadduct **2a** in UiO-67. (a) Chemical structure of **2a**. (b) Ball-stick model of **2a**. (c) CPK model of **2a** in UiO-67 tetrahedral pores. (d) Structure model of **2a** in UiO-67 triangular window.

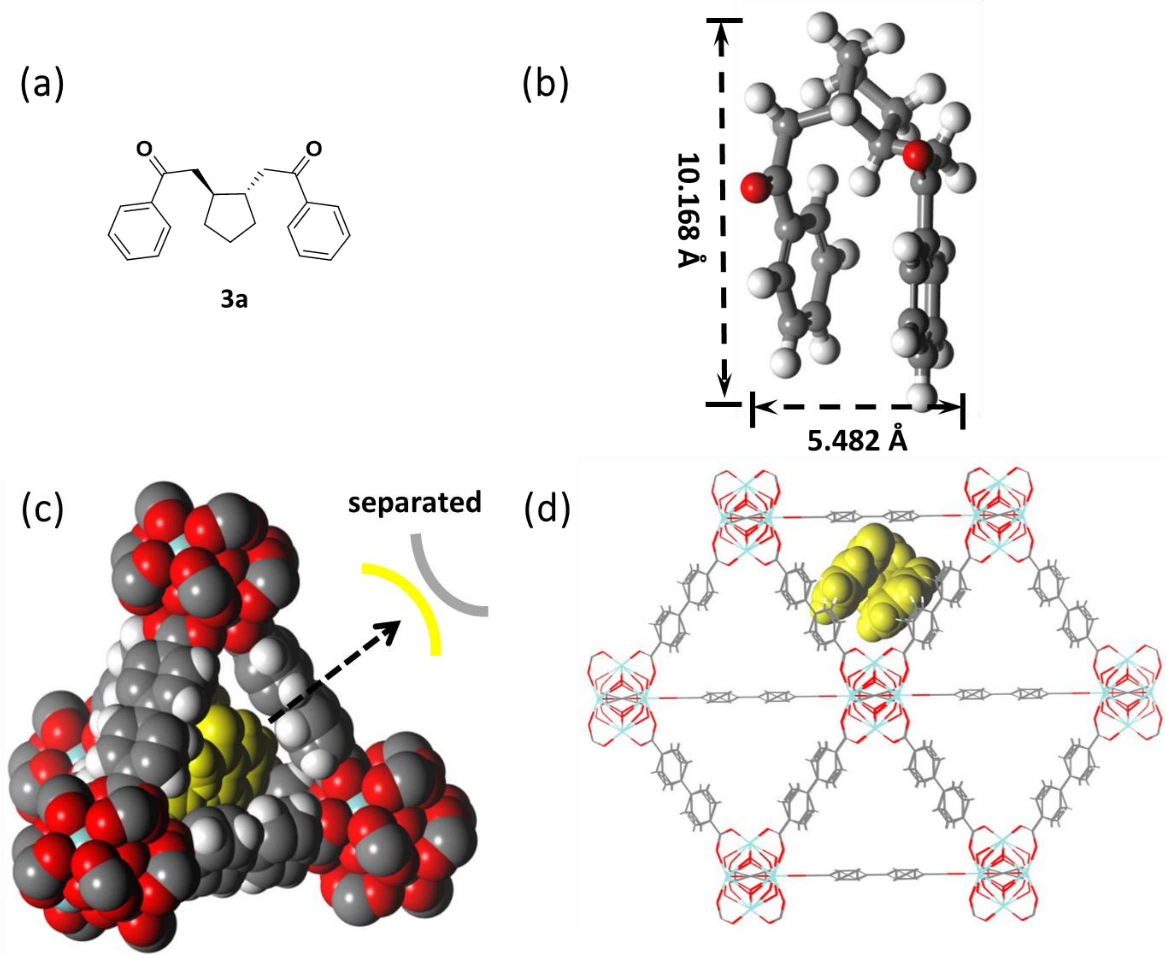

Figure 2-11. Structure model of reductive cycloadduct **3a** in UiO-67. (a) Chemical structure of **3a**. (b) Ball-stick model of **3a**. (c) CPK model of **3a** in UiO-67 tetrahedral pores. (d) Structure model of **3a** in UiO-67 triangular window.

2.2.5 RuBPY-MOL Catalyzed Reductive Cyclizations of Bis(enones)

We also studied intermolecular [2+2] cross cycloadditions of acyclic enones[38] with RuBPY-MOL and RuUiO-67 as photocatalysts. RuBPY-MOL catalyzed cross cycloadditions between various enones and Michael acceptors to afford cyclobutyl diones in 55-81% yields

(**Table 2-5**). Under identical condition, RuUiO-67 afforded cyclobutyl diones in much lower yields (5-26%).

Table 2-5. Crossed [2+2] cycloadditions of acyclic enones[a]

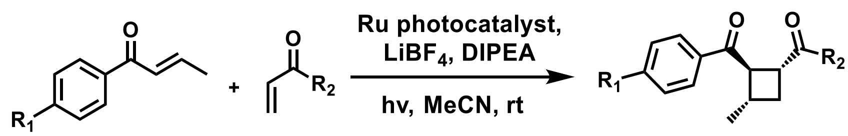

Entry	Enone	Michael Acceptor	Cycloadduct	Catalyst	Time	Yield[b]	dr[c]
1	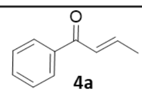 4a	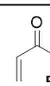 5a	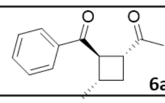 6a	RuBPY-MOL	12h	75%	6:1
2				RuUiO67	12h	12%	6:1
3	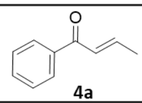 4a	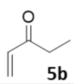 5b	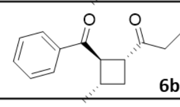 6b	RuBPY-MOL	12h	78%	10:1
4				RuUiO67	12h	18%	8:1
7	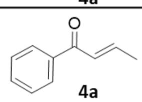 4a	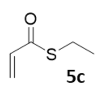 5c	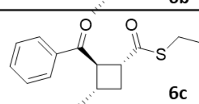 6c	RuBPY-MOL	12h	72%	>10:1
8				RuUiO67	12h	25%	>10:1
9	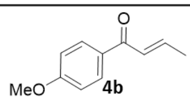 4b	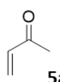 5a	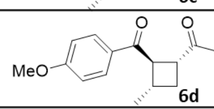 6d	RuBPY-MOL	24h	55%	6:1
10				RuUiO67	24h	<5%	--
11	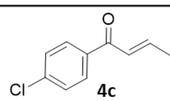 4c	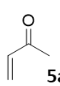 5a	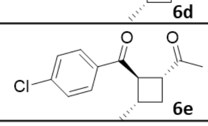 6e	RuBPY-MOL	6h	81%	>10:1
12				RuUiO67	6h	26%	>10:1

[a]Reaction conditions: 2.5 eq. Michael acceptor, 1 mol% RuBPY-MOL or RuUiO-67, 2 eq. DIPEA, 4 eq. $LiBF_4$, 6 mW/cm^2 410 nm LED, MeCN (0.1M). [b]Isolated yields. [c]Diastereomer ratios determined by NMR.

The cross-coupled products **6a-6e** bear only one phenyl group and are thus significantly smaller than the intramolecular [2+2] cycloaddition products in **Table 2-5**. Take **6c** as an example, with a flexible thioester chain, it can be easily fitted in to UiO-67 pore (**Figure 2-12**). As a result, the transition states and intermediates for the cross cycloaddition reactions can also be accommodated in the pores of RuUiO-67. Therefore pore size limitations will not be a limiting factor here for the different reactivity. We attribute the drastically different catalytic efficiencies between RuBPY-MOL and RuUiO-67 to restricted diffusion of reactive intermediates in MOF channels.

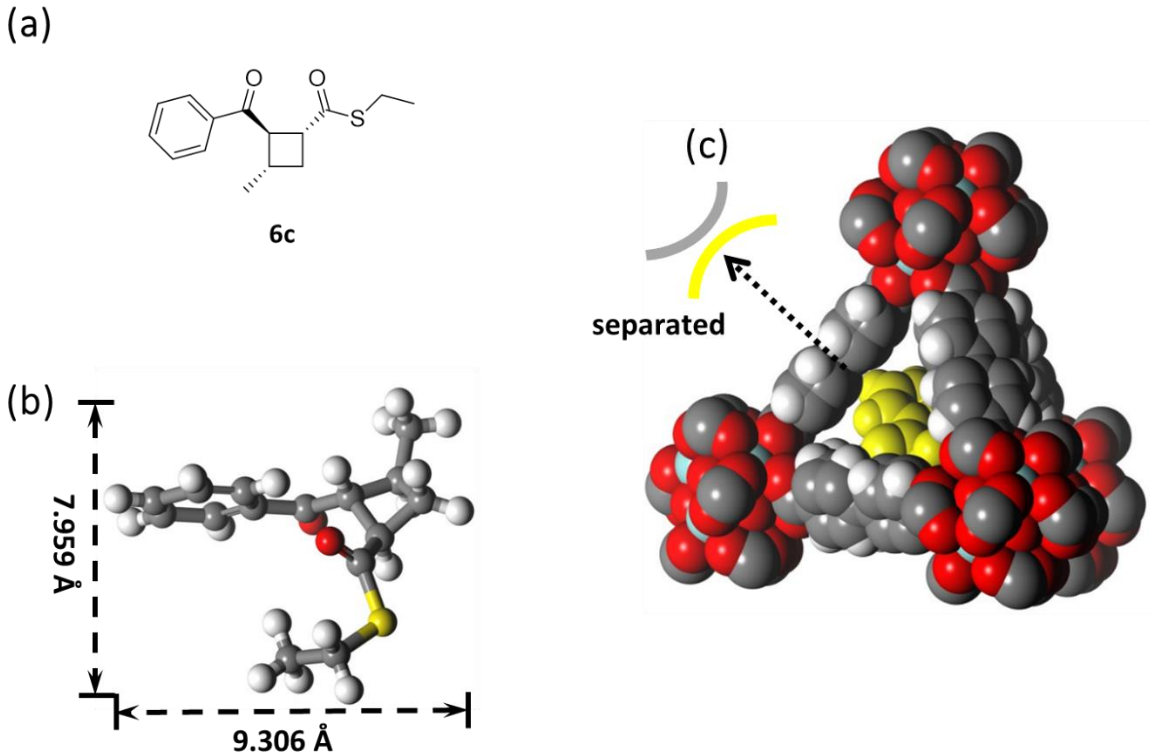

Figure 2-12. Structure model of crossed [2+2] adduct **6c** in UiO-67. (a) Chemical structure of **6c**. (b) Ball-stick model of **6c**. (c) CPK model of **6c** in UiO-67 tetrahedral pores.

We studied the RuBPY-MOL catalyzed reactions mechanism by measuring photoluminescence quenching of $Ru(bpy)_3^{2+}$* with different substrates (**Figures 2-13** and **Figure 2-14**). RuBPY–MOL showed significant quenching by DIPEA with a Stern-Völmer constant $K_{SV} = (1.22 \pm 0.05) \times 10^{-3}$ $mmol^{-1} \cdot L$, but was not quenched by other reactants including enones, Michael acceptors, $LiBF_4$, and HCOOH.

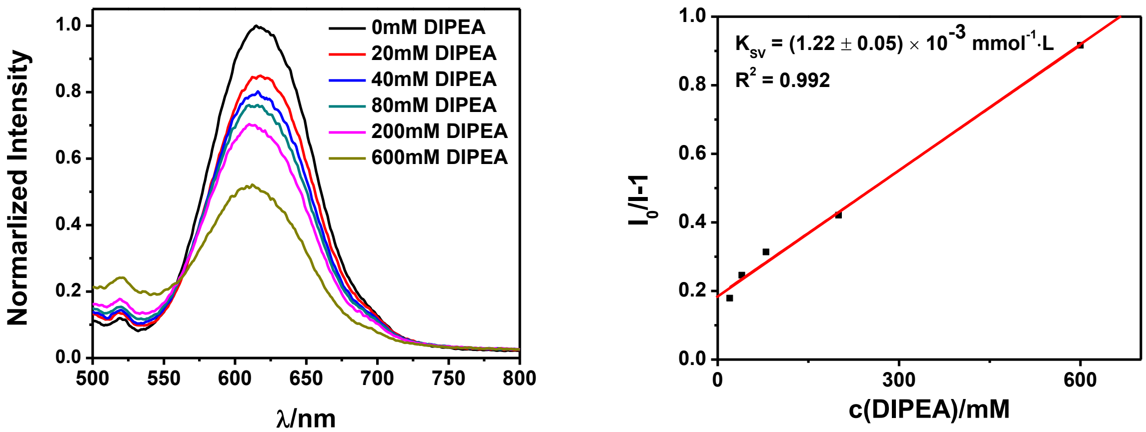

Figure 2-13. Photoluminescence quenching of RuBPY-MOL by DIPEA (left) and fitting to Stern-Völmer equation $\frac{I_0}{I} - 1 = K_{SV} \cdot c$ (right). (RuBPY-MOL: 40 μM by Ru in MeCN, Ex: 450 nm).

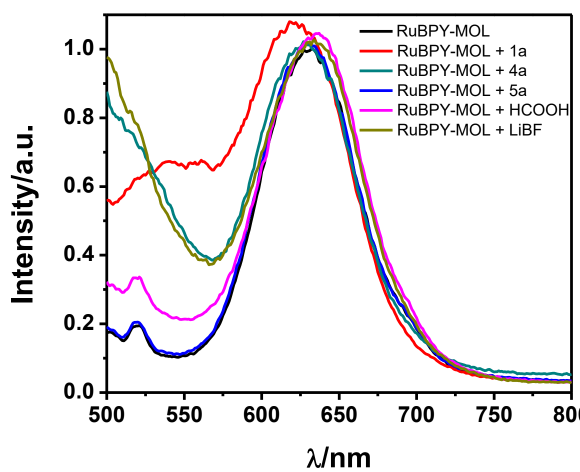

Figure 2-14. Photoluminescence of RuBPY-MOL in the presence of different reactants. RuBPY-MOL: 40 μM by Ru, Ex: 480 nm to avoid auto-fluorescence of some reactants. **1a**: 100 mM; **4a**: 100 mM; **5a**: 250 mM; HCOOH: 250 mM $LiBF_4$: 400 mM.

Photoluminescence quenching results suggest the following mechanism (**Scheme 2-3**). Upon light irradiation, photo-excited RuBPY-MOL will first react with DIPEA, generating $[Ru(bipy)_3]^+$ species, which undergoes SET with enones to generate highly active species. This is consistent with previously proposed mechanisms for homogeneously catalyzed reactions.[6,34,38]

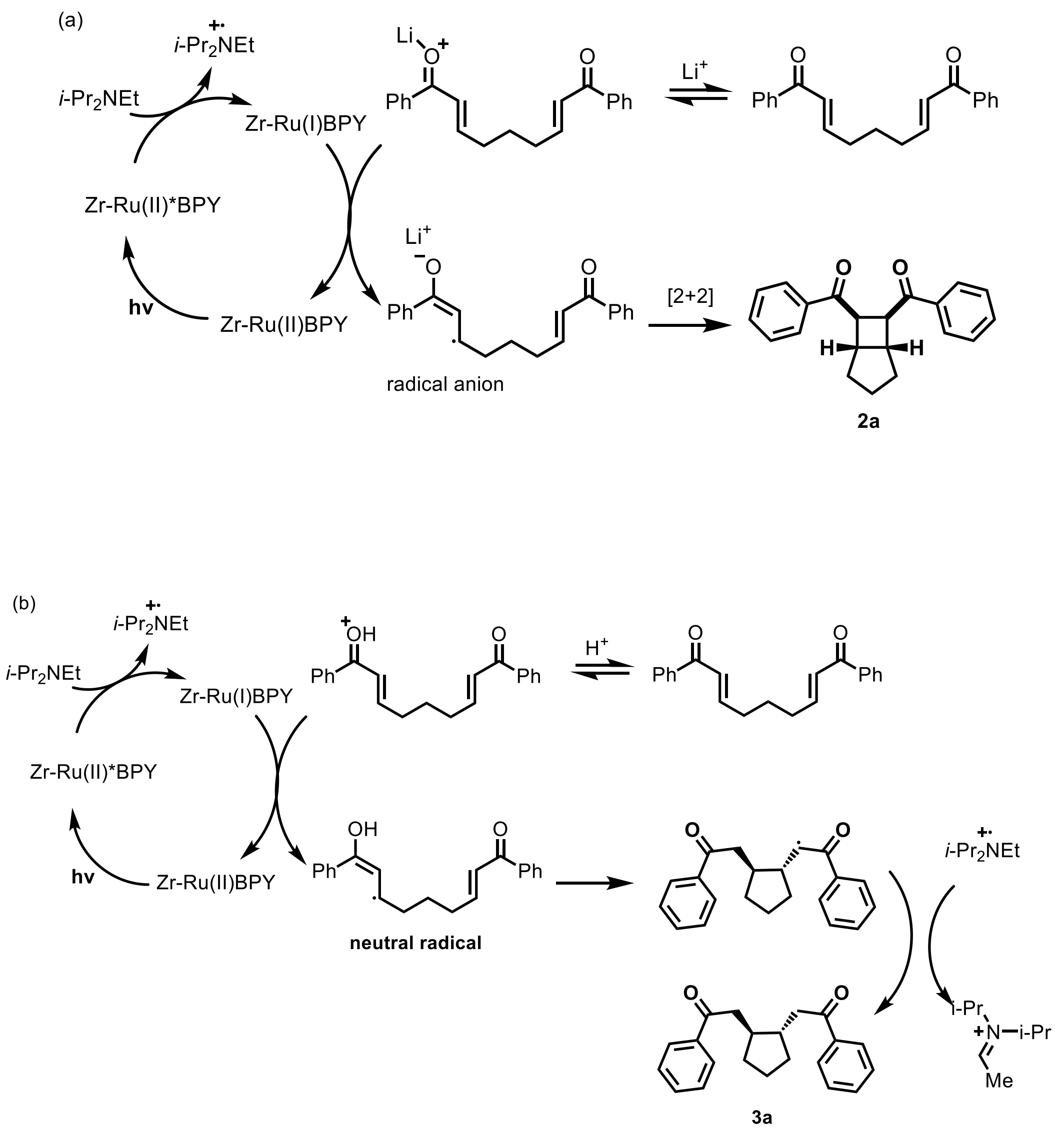

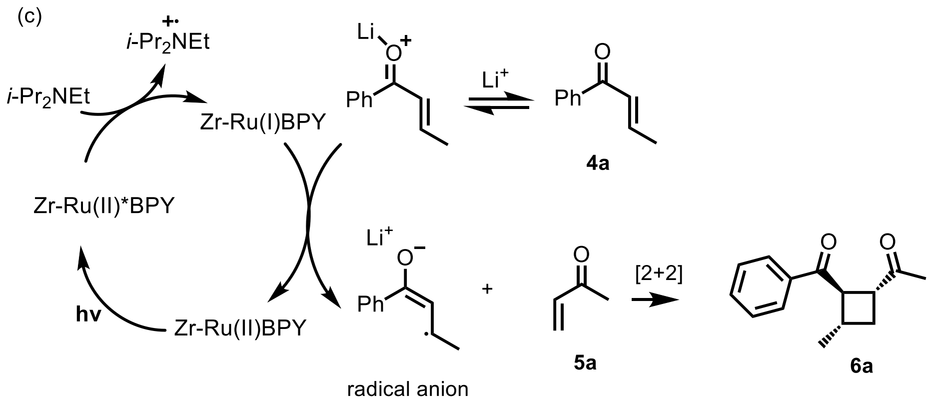

Scheme 2-3. Proposed mechanisms for RuBPY-MOL catalyzed (a) intermolecular [2+2] cycloadditions of bis(enones); (b) reductive cyclizations of bis(enones); (c) crossed [2+2] cycloadditions of acyclic enones.

Unlike unimolecular [2+2] cycloadditions and reductive cyclization reactions of bis(enones) (**Scheme 2-3a, b**), the highly reactive enolate anions in cross cycloadditions must travel some distances to find Michael acceptors to lead to desired products (**Scheme 2-3c**). However, diffusion in these active species in MOF channels is highly inhibited. In MOFs, the diffusivity D of guest molecules decreases dramatically as the molecular size increases due to two reasons.[39] On one hand, larger molecules generally have stronger interactions with MOFs, which increases activation energy for transport, leading to decreased diffusivity. On the other hand, due to MOF pore size limitation, moderately sized molecules can only diffuse in one direction through narrow gates formed in MOF, and they have to adopt certain conformation, which severely hinders their motion. Thus, typical organic compounds (like trimethylamine, cyclohexane, ~10^{-12}~10^{-14} m^2/s) can have orders of magnitude difference in diffusivity compared with small molecules (H_2, $^1O_2$, CH_4, ~10^{-9} m^2/s).[29,39]

In photoreactions, active species (radicals/cationic radicals/anionic radicals/singlet species) are generated upon light irradiation. Take a typical organic radical - benzyl radical as an example, the lifetime is $\tau = 1.44\ \mu s$[40] (with respect to photolysis of toluene).

In free MeCN solution or in MOL-catalyzed reaction, the diffusivity for an organic compound (**1a,** M ~ 300 g/mol) in MeCN is $D = 1.5\times10^{-9}\ m^2/s$.[41] The diffusion length can thus be calculated as:

$$r_{MOL} = \sqrt{\tau \times \mathrm{D}} = \sqrt{1.44 \times 10^{-6}\ \mathrm{s} \times 1.5 \times 10^{-9}\ m^2/s} = 46\ \mathrm{nm} \tag{2-1}$$

This is a large diffusion length for active species to move and collide with other substrates.

In MOFs, use $\mathrm{D}' = 10^{-12}\ m^2/s$, and the same lifetime τ.

$$r_{MOF} = \sqrt{\tau \times \mathrm{D}'} = \sqrt{1.44 \times 10^{-6}\ \mathrm{s} \times 10^{-12}\ m^2/s} = 1.2\ \mathrm{nm} \tag{2-2}$$

This number is even smaller than the unit cell length of MOFs, active species can hardly diffuse out of MOF cages to have effective collision with other substrates. In terms of the crossed [2+2] cycloaddition reactions, the enolate anions can decompose in MOF cages before finding Michael acceptors due to restricted diffusion. Hence, MOFs are poor candidates in multi-component photocatalysis. In contrast, as a 2D material, RuBPY-MOL allows free diffusion of reaction substrates and intermediates in multicomponent photoreactions, leading to much higher photocatalytic efficiency than its MOF counterpart.

2.2.6 RuBPY-MOL Catalyzed Meerwein Addition Reactions

The superior photocatalytic activity of RuBPY-MOL over RuUiO-67 was also demonstrated in Meerwein addition reactions (**Table 2-6**).[42] RuBPY-MOL efficiently catalyzed three-component Meerwein addition reactions between aryl diazonium salts, styrenes, and nitriles under LED irradiation to afford desired products in 55-83% yields. In contrast, RuUiO-67 produced desired products in much lower 0-21% yields. The difference in photocatalytic activities of RuBPY-MOL over RuUiO-67 is likely due to the ease of intermediate and substrate diffusion in 2D MOLs but not 3D MOFs. The reaction mechanism of photo Meerwein addition reactions is shown in **Scheme 2-4**.

Table 2-6. Meerwein addition reactions[a]

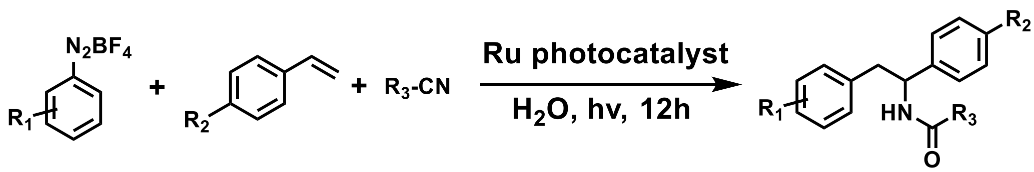

Entry	Dizazonium Salt	Styrene	Nitrile	Adduct	Catalyst	Yield[b]
1	7a	8a	MeCN	9a	RuBPY-MOL	83%
2					RuUiO67	<10%
3	7b	8a	MeCN	9b	RuBPY-MOL	55%
4					RuUiO67	n.r.
5	7c	8a	MeCN	9c	RuBPY-MOL	76%
6					RuUiO67	<5%
7	7a	8b	MeCN	9d	RuBPY-MOL	76%
8					RuUiO67	21%
9	7a	8a	$ClCH_2CN$	9e	RuBPY-MOL	62%
10					RuUiO67	15%

[a]Reaction conditions: 1 eq. diazonium salt, 2 eq. styrene, 0.5% RuBPY-MOL or RuUiO-67, 1 eq. H_2O, 6 mW/cm^2 410 nm LED, MeCN or $ClCH_2CN$ (0.25 M), room temperature. [b]Isolated yields.

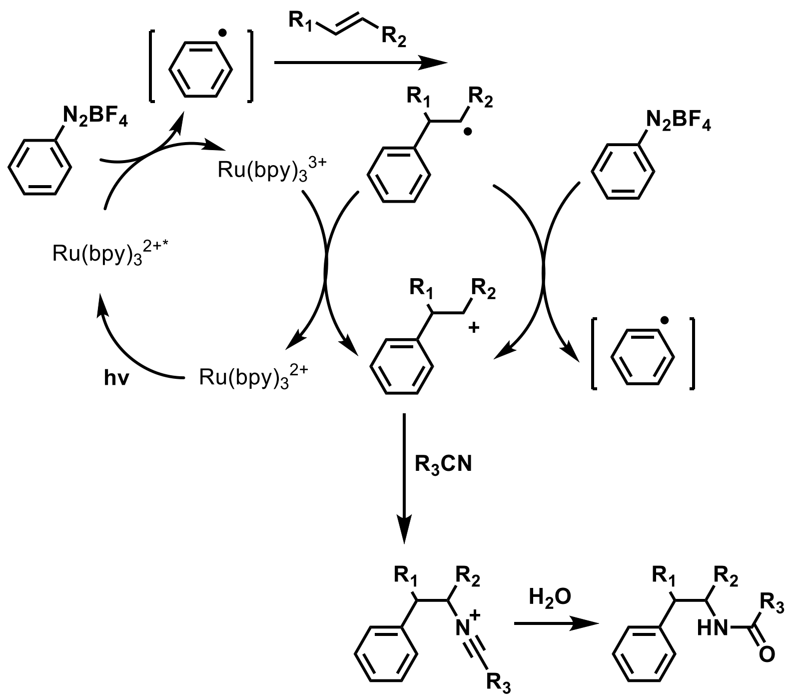

Scheme 2-4. Proposed mechanism for RuBPY-MOL catalyzed photo Meerwein addition reaction.[42]

2.3 Conclusion

In this work, we synthesized photoactive RuBPY-MOL via post-synthetic incorporation of $Ru(bpy)_3^{2+}$ into the backbone of BPY-MOL. RuBPY-MOL was shown to be an efficient heterogeneous photocatalyst for intra/intermolecular [2+2] cycloaddition and Meerwein addition reactions under visible-light irradiation without significant loss of activity for at least three cycles. In contrast, the corresponding MOF catalyst, RuUiO-67 bearing the same $Ru(bpy)_3^{2+}$ photosensitizer failed in these photoreactions, due to either pore size limitation or restricted diffusion of reactive intermediates. We also observed distinct catalytic activity of RuUiO-67 for two different photoreactions with same substrates because of different reaction pathways. This can be instructive in terms of designing and using MOFs for certain reactions with selective pathways to inhibit side products. Our work highlights the potential of MOLs in catalyzing a variety of multicomponent photoreactions.

2.4 Methods and Experimental Details

2.4.1 General Methods

All starting materials were purchased from Aldrich and Fisher, unless otherwise noted. ^{1}H NMR spectra were recorded on a Bruker NMR 500 DRX spectrometer at 500 MHz and referenced to the proton resonance resulting from incomplete deuteration of the $CDCl_3$ (δ 7.26). ^{13}C NMR spectra were recorded at 125 MHz, and all of the chemical shifts were reported downfield in ppm relative to the carbon resonance of $CDCl_3$ (δ 77.10). TEM data were collected on a Tecnai Spirit (FEI, USA) electron microscope. Powder X-ray diffraction data were collected on a Bruker D8 Venture diffractometer using Cu Kα radiation source (λ = 1.54178 Å). UV-vis data were taken on a Shimadzu UV-2600 spectrometer. Photoluminescence data were taken on a RF-5301 fluorimeter. RuBPY-MOL samples were subjected to microwave digestion (MARS 6, OneTouch, HNO_3/HF/HCl (18:1:1 v/v/v), 200 ^{o}C, 50 min) prior to ICP-MS measurement. ICP-MS data were obtained with an Agilent 7700x ICP-MS and analyzed using ICP-MS MassHunter version B01.03. Samples were diluted in a 2% HNO_3 matrix and analyzed with a ^{159}Tb internal standard against a 12-point standard curve over the range from 0.1ppb to 500ppb. Thermogravimetric analysis (TGA) was performed in air using a Shimadzu TGA-50 equipped with a platinum pan and heated at a rate of 2 °C per min. Photoreactions were performed under the irradiation of a 410nm blue LED (IM101C121M Potrans power supply). The light intensity was determined by an optical power meter (PM100D, Thorlabs).

2.4.2 Synthesis Details

Synthesis of H_3BPY ligands

H_3BPY was synthesized according to **Scheme 2-5**.

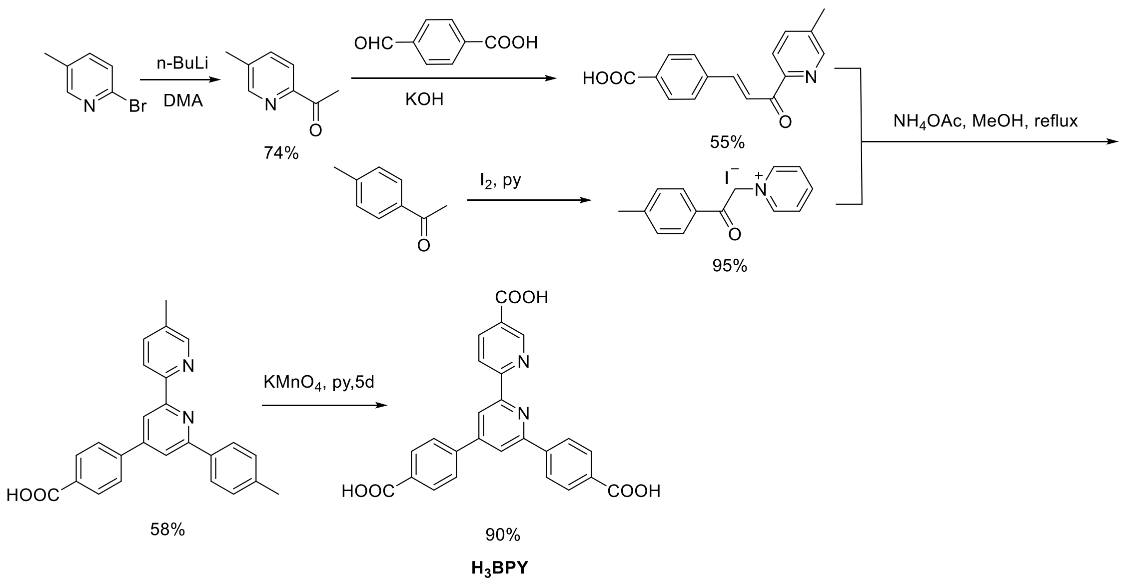

Scheme 2-5. Synthesis of H_3BPY.

1-(5-methylpyridin-2-yl)ethanone

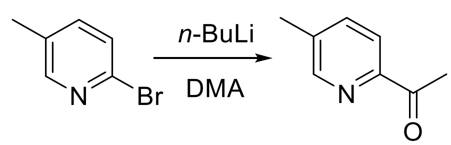

2-bromo-5-methylpyridine (15 g, 87 mmol) was dissolved in 165 mL dry Et_2O and cooled to -78 ^{o}C. *n*-BuLi (35 mL, 2.5M in hexene) was added dropwise over 1h. The mixture was stirred at -78 ^{o}C for 90 min before dimethylacetamide (9 mL) was added dropwise and stirred for another 3h. Sat. NH_4Cl (aq.) was added to quench the reaction. The aqueous layer was washed with Et_2O a couple of times and all the organic parts were combined, dried over anhydrous Mg_2SO4 and filtered. After evaporation of the solvent, the residue was subjected to flash column chromatography on silica gel (10:90 EtOAc/CH_2Cl_2 as eluent), affording 1-(5-methylpyridin- 2-yl)ethanone (9.7 g, 65 mmol, 74% yield) as colorless oil. ^{1}H NMR (500 MHz, $CDCl_3$): δ 8.50 (s, 1 H), 7.95 (d, 1 H, J = 8.0 Hz), 6.21 (m, 1 H), 2.70 (s, 3 H), 2.42 (s, 3 H).

4-(5-methylpyridin-2-yl)formylvinyl benzoic acid

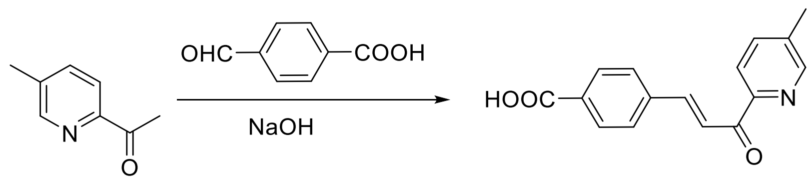

1-(5-methylpyridin-2-yl)ethanone (9.7 g, 65 mmol) was dissolved in EtOH (10 mL), which was added dropwise to a mixed solution of 4-carboxybenzaldehyde (10 g, 74.2 mmol) and NaOH (3.6 g, 90 mmol) in EtOH/H_2O (1:1 v/v, 100mL). The reaction mixture was stirred at room temperature overnight. The reaction vessel was then cooled in ice and the precipitate was separated via filtration and dissolved in MeOH/H_2O (1:1). 1M HCl was added to adjust the pH to 4-5 to afford white precipitate, which was collected via filtration and washed with MeOH/H_2O. This procedure produced 4-(5-methylpyridin-2-yl)formylvinyl benzoic acid. (9.6 g, 35.9 mmol, 55% yield). ^{1}H NMR (500 MHz, DMSO-d^6): δ 13.15 (br, 1H), 8.65 (s, 1H), 8.35 (d, 1H, J = 16.0 Hz), 7.8 – 8.1 (m, 7H), 2.43 (s, 3H).

1-(2-oxo-2-(p-tolyl)ethyl)pyridin-1-ium

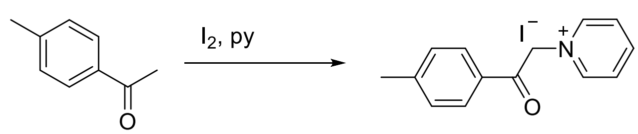

4'-methylacetophenone (6.68 mL, 50 mmol) and iodine powder (12.7 g, 50 mmol) were dissolved in 50 mL pyridine and heated at 120°C with stirring overnight. The reaction mixture was then cooled to 0°C. Brown precipitate was filtered and washed sequentially with cold pyridine, $CHCl_3$

and Et_2O and then dried under vacuum to afford 1-(2-oxo-2-(p-tolyl)ethyl)pyridin-1-ium (15.3 g, 45mmol, 95% yield) as yellowish solid. ^{1}H NMR (500 MHz, DMSO-d^6): δ 8.99 (d, 2 H, J = 6.5 Hz), 9.74 (t, 1 H, J = 8.0 Hz), 8.28 (t, 2 H, J = 7.0 Hz), 7.98 (d, 2 H, J = 7.0 Hz), 7.49 (d, 2 H, J = 8.0 Hz), 6.43 (s, 2 H), 2.46 (s, 3 Hz).

4-[2-(4-methylphenyl)-6-(5-methylpyridin-2-yl)pyridin-4-yl]benzoic acid

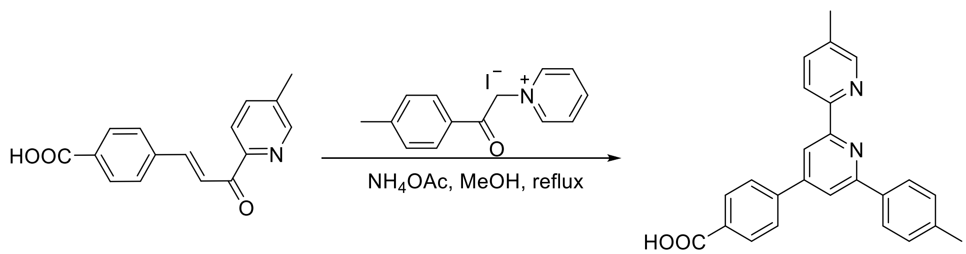

4-(5-methylpyridin-2-yl)formylvinyl benzoic acid (9.5 g, 35.6 mmol) and 1-[2-(4-methylphenyl)-2-oxoethyl]-pyridinium iodide (12.1 g, 35.6 mmol) were dissolved in 210mL MeOH, followed by the addition of NH_4OAc (27.4 g, 252 mmol). The reaction mixture was stirred under reflux for 6h. After cooling to 0 ^oC, the precipitate was filtered and washed with cold MeOH, and Et_2O to obtain 4-[2-(4-methylphenyl)-6-(5-methylpyridin-2-yl)pyridin-4-yl]benzoic acid (8.1 g, 21.4 mmol, 60% yield) as white solid. ^{1}H NMR (500 MHz, DMSO-d^6): δ 8.60-8.58 (2H), 8.53 (d, 1H, J = 8.0 Hz), 8.33-8.25 (m, 3H), 8.14-8.08 (m, 4H), 7.84 (d, 1H, J = 7.0 Hz), 7.38 (d, 2H, J = 8.0 Hz), 2.40 (s, 6H).

4',6'-dibenzoato-[2,2'-bipyridine]-4-carboxylic acid (H_3BPY)

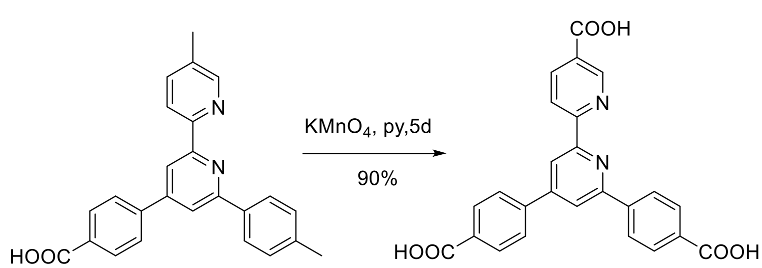

H_3BPY (6.3 g, 16.6 mmol) was dissolved in pyridine/H_2O (3:1, 450 mL), followed by the addition of $KMnO_4$ (9 g, 57 mmol). The reaction mixture was heated at 90 ^oC overnight. More $KMnO_4$ (9 g × 5, 84 mmol) was added into the reaction mixture to ensure complete oxidation. After refluxing for 5 d, the reaction mixture was cooled to room temperature, added with EtOH to react with residue $KMnO_4$, and filtered. The filtrate was put into rotovape to remove most of the solvent. 1M HCl was added to the filtrate to adjust the pH to 3. White precipitates were collected via filtration, washed tremendously with water, and dried in vacuo to afford H_3BPY (6.6 g, 15.0 mmol, 90% yield). ^1H NMR (500 MHz, DMSO-d^6) δ 12.23 (br, 3H), 9.24 (s, 1H), 8.79-8.76 (m, 2H), 8.53-8.49 (m, 4H), 8.18 - 8.11 (m, 6H).

Synthesis of BPY-MOL: H_3BPY (12.5mg, 28.3 μmol) and $ZrCl_4$ (10.2 mg, 43.8 μmol) were mixed in DMF (2.05 mL). To this mixture was added HCOOH (0.88 mL) and H_2O (0.3 mL). The final mixture was dispersed by sonication and kept in a 120 ˚C oven for 2 days. The white precipitate was collected via centrifugation and washed with DMF and EtOH three times. Yield: 9.6 mg (74%).

Synthesis of RuBPY-MOL: The above as-synthesized BPY-MOL dispersion in EtOH was added with $Ru(bpy)_2Cl_2$ (9.7 mg, 20 umol). After 24h, the sample was collected by centrifugation and washed with DMF and MeCN 3 times respectively to completely remove unreacted $Ru(bpy)_2Cl_2$. RuBPY-MOL was saved in ethanol as a stock solution for further use.

Synthesis of UiO-67-(bpy)$_{0.25}$: $ZrCl_4$ (120 mg, 0.514 mmol), benzoic acid (1.88 g,15.4 mmol), H_2bpdc (94 mg, 0.39 mmol), and H_2bpydc (31 mg, 0.13 mmol) were mixed in 20 mL DMF. The solids were dispersed via sonication and heated at 120 °C for 24 h. After cooling, the white precipitate was collected by centrifugation and washed with DMF and EtOH at least 2 times, respectively. Yield: 129 mg (71%).

Synthesis of RuUiO-67: UiO-67-$(bpy)_{0.25}$ (35.5 mg, 0.1 mmol) and $Ru(bpy)_2Cl_2$ (48.4 mg,0.1 mmol) were placed in a scintillation vial that was filled with 1 mL EtOH and 1 mL H_2O. The solids were dispersed via sonication and heated at 80 °C overnight. After cooling, the solids were collected by centrifugation and washed with EtOH twice and MeCN twice. The solids were soaked in MeCN for 3 d, with the solution exchanged with fresh MeCN (10 mL) every 24 h. The resulting solids were used for photoreactions.

General Procedures for Intramolecular [2+2] Cycloaddition of Bis(enones)

The bis(enone) substrates **1a-1e** were synthesized according to reported procedures.[43]

An 8 mL glass vial was charged with bisenone **1** (400 μmol, 1 equiv.), Ru photocatalysts (1% RuBPY-MOL or RuUiO-67, 4 μmol by Ru), $LiBF_4$ (75 mg, 800 μmol, 2 equiv.), DIPEA (139 μL, 800 μmol, 2 equiv.) and acetonitrile (4 mL, 0.1 M). The vial was sealed with a septum and parafilm, degassed in the dark with three freeze-pump-thaw cycles under nitrogen. The reaction was stirred and irradiated with a 410 nm LED. Light intensity at the reaction vial was maintained at 6 mW/cm^2. The reaction was monitored by TLC. Upon completion of the reaction, dichloromethane was added to completely dissolve the product. The heterogeneous photocatalyst was separated by centrifugation. The solvents were removed on a rotary evaporator. The residue was purified by silica gel column chromatography to afford **2a-2e**.

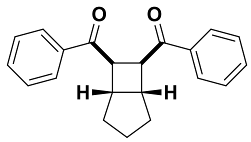

2a: yield: 82%. ^{1}H NMR (500 MHz, $CDCl_3$): δ 7.75 (d, *J* = 8.5 Hz, 4H), 7.45 (t, *J* = 7.5 Hz, 2H), 7.34 (t, *J* = 7.5Hz, 4H), 3.86 (d, *J* = 4 *Hz*, 2H), 3.21 (m, 2H), 2.03 (m, 2H), 1.85 (m, 2H), 1.70 (m, 2H). The ^{1}H NMR peaks are consistent with those reported in the literature.[6]

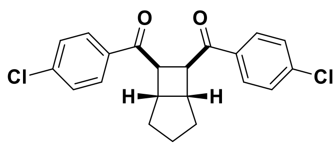

2b: yield: 86%. ^{1}H NMR (500 MHz, $CDCl_3$): δ 7.68 (d, *J* = 8.5 Hz, 4H), 7.33 (d, *J* = 8.5 Hz, 4H), 3.80 (d, *J* = 4 Hz, 2H), 3.18 (m, 2H), 2.03 (m, 2H), 1.83 (m, 2H), 1.71 (m, 2H). The ^{1}H NMR peaks are consistent with those reported in the literature.[6]

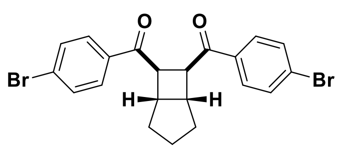

2c: yield: 92%. ^{1}H NMR (500 MHz, $CDCl_3$): δ 7.61 (d, *J* = 8.5 Hz, 4H), 7.51 (d, *J* = 8.5 Hz, 4H), 3.79 (d, *J* = 4 Hz, 2H), 3.18 (m, 2H), 2.02 (m, 2H), 1.82 (m, 2H), 1.70 (m, 2H); ^{13}C NMR (125 MHz, $CDCl_3$): δ 197.66, 135.05, 131.95, 129.38, 127.83, 48.25, 39.18, 32.51, 25.28; ESI-MS: calc'd for $[M+H]^+$: 461.0; found 460.9.

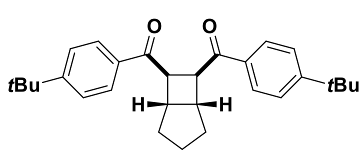

2d: yield: 79%. ^{1}H NMR (500 MHz, $CDCl_3$): δ 7.70 (d, *J* = 8.5 Hz, 4H), 7.36 (d, *J* = 8.0 Hz, 4H), 3.83 (d, *J* = 4 Hz, 2H), 3.20 (m, 2H), 2.02 (m, 2H), 1.84 (m, 2H), 1.69 (m, 2H), 1.28 (s, 18H); ^{13}C NMR (125 MHz, $CDCl_3$): δ 198.38, 156.12, 133.91,127.84, 125.49, 48.43, 39.14, 35.07, 32.60, 31.15, 25.34; ESI-MS: calc'd for $[M+H]^+$: 417.3; found: 417.3.

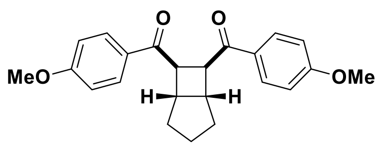

2e: yield: 73%. ^{1}H NMR (500 MHz, $CDCl_3$): δ 7.73 (d, *J* = 9.0 Hz, 4H), 6.82 (d, *J* = 9.0 Hz, 4H), 3.81 (s, 6H), 3.79 (d, *J* = 4 Hz, 2H), 3.19 (m, 2H), 2.02 (m, 2H), 1.83 (m, 2H), 1.69 (m, 2H). The ^{1}H NMR peaks are consistent with those reported in the literature.[6]

General Procedures for Reductive Cyclization of Bis(enones)

A 20 mL glass vial was charged with bisenone **1** (400 μmol, 1 equiv.), Ru photocatalysts (2.5% RuBPY-MOL or RuUiO-67, 10 μmol by Ru), HCOOH (75 μL, 2 mmol, 5 equiv.), DIPEA (697 μL, 4 mmol, 10 equiv.) and acetonitrile (8 mL, 0.05 M). The vial was sealed with a septum and parafilm, and degassed in the dark with three freeze-pump-thaw cycles under nitrogen. The mixture was stirred and irradiated with a 410 nm LED. Light intensity at the reaction vial was maintained at 6 mW/cm^2. The reaction progress was monitored by TLC. The heterogeneous photocatalyst was separated by centrifugation. The organic volatiles were removed on a rotary evaporator. The residue was purified by silica gel column chromatography to afford **3a-3e**.

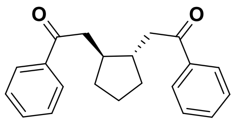

3a: yield: 80%. ^{1}H NMR (500 MHz, $CDCl_3$): δ 7.95 (d, *J* = 7.5 Hz, 4H), 7.55 (t, *J* = 7.5 Hz, 2H), 7.45 (t, *J* = 7.0 Hz, 4H), 3.20 (dd, *J* = 16.5 Hz, 4.5 Hz, 2H), 2.94 (dd, J = 16.5 Hz, 8.5Hz, 2H), 2.19 (m, 2H), 1.99 (m, 2H), 1.63 (m, 2H), 1.29 (m, 2H). The ^{1}H NMR peaks are consistent with those reported in the literature.[34]

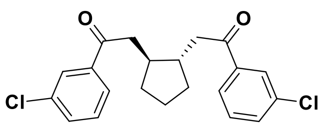

3b: yield: 85%. ^{1}H NMR (500 MHz, $CDCl_3$): δ 7.87 (d, *J* = 8.5 Hz, 4H), 7.42 (d, *J* = 8.5 Hz, 2H), 3.16 (dd, *J* = 16.5 Hz, 4.5 Hz, 2H), 2.92 (dd, J = 16.5 Hz, 8.0Hz, 2H), 2.16 (m, 2H), 1.97 (m, 2H), 1.64 (m, 2H), 1.29 (m, 2H). The ^{1}H NMR peaks are consistent with those reported in the literature.[34]

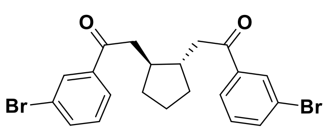

3c: yield: 88%. ^{1}H NMR (500 MHz, $CDCl_3$): δ 7.79 (d, *J* = 8.5 Hz, 4H), 7.59 (d, *J* = 8.5 Hz, 2H), 3.15 (dd, *J* = 16.5 Hz, 5.0 Hz, 2H), 2.91 (dd, J = 17.0 Hz, 8.0Hz, 2H), 2.16 (m, 2H), 1.96 (m, 2H), 1.64 (m, 2H), 1.29 (m, 2H); ^{13}C NMR (125 MHz, $CDCl_3$): δ 199.21, 135.91, 131.97, 129.71, 128.24, 44.09, 41.46, 32.67, 23.79; calc'd for $[M+H]^+$: 463.0; found 462.9.

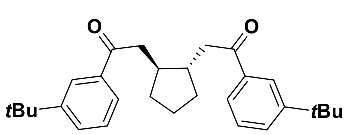

3d: yield: 93%. ^{1}H NMR (500 MHz, $CDCl_3$): δ 7.89 (d, *J* = 8.5 Hz, 4H), 7.46 (d, *J* = 8.5 Hz, 2H), 3.17 (dd, *J* = 16.0 Hz, 3.5 Hz, 2H), 2.91 (dd, J = 16.0 Hz, 8.0Hz, 2H), 2.18 (m, 2H), 1.97 (m, 2H), 1.62 (m, 2H), 1.34 (s 18H), 1.26 (m, 2H); ^{13}C NMR (125 MHz, $CDCl_3$): δ 200.08, 156.71, 134.72, 128.18, 125.59, 43.95, 41.87, 35.17, 32.61, 31.18, 23.77; calc'd for $[M+H]^+$: 419.3; found 419.3.

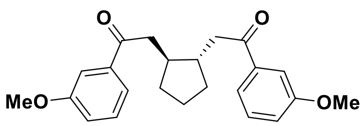

3e: yield: 75%. ^{1}H NMR (500 MHz, $CDCl_3$): δ 7.93 (d, *J* = 9.0 Hz, 4H), 6.92 (d, *J* = 9.0 Hz, 2H), 3.86 (s, 6H), 3.13 (dd, *J* = 16.5 Hz, 4.5 Hz, 2H), 2.87 (dd, J = 16.0 Hz, 8.5Hz, 2H), 2.16 (m, 2H), 1.96 (m, 2H), 1.61 (m, 2H), 1.26 (m, 2H). The ^{1}H NMR peaks are consistent with those reported in the literature.[34]

General Procedures for Crossed [2+2] Cycloadditions of Acyclic Enones

4a and **4b** were synthesized by Friedel-Crafts acylation. **4c**[44] and **5c**[45] were synthesized according to literature procedures.

An 8 mL glass vial was charged with enone **4** (400 μmol, 1 equiv.), Michael acceptor **5** (1 mmol, 2.5 equiv.), Ru photocatalysts (1% RuBPY-MOL or RuUiO-67, 4 μmol by Ru), $LiBF_4$ (150 mg, 1.6 mmol, 4 equiv.), DIPEA (139 μL, 800 mol, 2 equiv.) and acetonitrile (4 mL). The vial was sealed with a septum and parafilm, and degassed in the dark with three freeze-pump-thaw cycles under nitrogen. The mixture was stirred and irradiated with a 410 nm LED. Light intensity at the reaction vial was maintained at 6 mW/cm^2. The reaction progress was monitored by TLC. Upon completion of the reaction, the heterogeneous photocatalyst was separated by centrifugation. The organic volatiles were removed by rotary evaporation. The residue was purified by silica gel column chromatography to afford **6a-6e**.

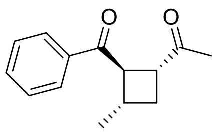

6a: yield: 75%. ^{1}H NMR (500 MHz, $CDCl_3$): δ 7.97 (d, *J* = 7.0 Hz, 2H), 7.57 (t, *J* = 7.5 Hz, 1H), 7.47 (t, *J* = 7.5 Hz, 2H), 3.91 (t, *J* = 8.0 Hz, 1H), 3.62 (q, *J* = 9.5 Hz,1H), 2.48 (m, 1H), 2.38 (m, 1H), 2.08 (s, 3H), 1.74 (q, *J* = 9.5 Hz, 1H), 1.18 (d, *J* = 7.0 Hz, 3H). The ^{1}H NMR peaks are consistent with those reported in the literature.[38]

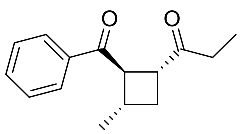

6b: yield: 78%. ^{1}H NMR (500 MHz, $CDCl_3$): δ 7.96 (d, *J* = 7.5 Hz, 2H), 7.56 (t, *J* = 7.5 Hz, 1H), 7.46 (t, *J* = 7.5 Hz, 2H), 3.93 (t, *J* = 7.5 Hz, 1H), 3.60 (q, *J* = 9.0 Hz, 1H), 2.5-2.3 (m, 4H), 1.74 (q, *J* = 9,5 Hz, 1H), 1.17 (d, *J* = 6.5 Hz, 3H), 1.03 (t, *J* = 7.5 Hz, 3H). The ^{1}H NMR peaks are consistent with those reported in the literature.[38]

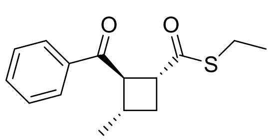

6c: yield: 72%. ^{1}H NMR (500 MHz, $CDCl_3$): δ 7.94 (d, *J* = 7.5 Hz, 2H), 7.57 (t, *J* = 7.5 Hz, 1H), 7.46 (t, *J* = 7.5 Hz, 2H), 3.96 (t, *J* = 8.5 Hz, 1H), 3.68 (q, *J* = 9.0 Hz, 1H), 2.87 (q, *J* = 7.5 Hz, 2H), 2.50 (m, 1H), 2.40 (m, 1H), 1.92 (q, J = 9.5 Hz, 1H), 1.23 (t, J = 7.0 Hz, 3H), 1.20 (d, J = 7.0 Hz, 3H). The ^{1}H NMR peaks are consistent with those reported in the literature.[38]

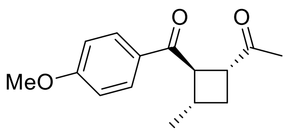

6d: yield: 55%. ^{1}H NMR (500 MHz, $CDCl_3$): δ 7.96 (d, J = 8.5 Hz, 2H), 6.94 (d, J = 9.0 Hz, 1H), 3.87 (s, 3H), 3.84 (1H), 3.61 (q, J = 9.0 Hz, 1H), 2,48 (m, 1H), 2.36 (q, J = 9.0 Hz, 1H), 2.07 (s, 3H), 1.73 (q, J = 9.5 Hz, 1H), 1.17 (d, J = 7.0 Hz, 3H). The ^{1}H NMR peaks are consistent with those reported in the literature.[38]

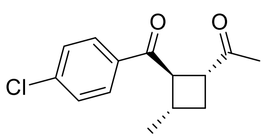

6e: yield: 81%. ^{1}H NMR (500 MHz, $CDCl_3$): δ 7.92 (d, J = 8.5 Hz, 2H), 7.44 (d, J = 8.0 Hz, 1H), 3.88 (t, J = 8.5 Hz, 1H), 3.57 (q, J = 9.0 Hz, 1H), 2,50 (m, 1H), 2.40 (m, 1H), 2.08 (s, 3H), 1.71 (q, J = 10.0 Hz, 1H), 1.16 (d, J = 7.0 Hz, 3H). The ^{1}H NMR peaks are consistent with those reported in the literature.[38]

General Procedures for Meerwein Addition Reactions

7a-7c were synthesized according to literature procedures.[46]

A 4 mL glass vial was charged with diazonium salt **7** (400 μmol, 1 equiv.), Styrene **8** (800 μmol, 2 equiv.), Ru photocatalysts (0.5% RuBPY-MOL or RuUiO-67, 2 μmol by Ru), H_2O (7.2 μL, 0.4 mmol, 1 equiv) and acetonitrile (or chloroacetonitrile, 1.6 mL). The vial was sealed with a septum and parafilm, and degassed in the dark with three freeze-pump-thaw cycles under nitrogen. The mixture was stirred and irradiated with a 410 nm LED. Light intensity at the reaction vial was maintained at 6 mW/cm^2. The reaction progress was monitored by TLC. Upon completion of the reaction, the heterogeneous photocatalyst was separated by centrifugation. The organic volatiles were removed by rotary evaporation. The residue was purified by silica gel column chromatography to afford **9a-9e**.

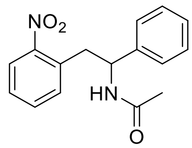

9a: yield: 83%. ^{1}H NMR (500 MHz, $CDCl_3$): δ 7.87(dd, *J* = 8.0 Hz, 1.2 Hz, 1H), 7.54 (td, *J* = 8.0 Hz, 1.2 Hz, 1H), 7.45 (dd, *J* = 8.0 Hz, 1.2 Hz, 1H), 7.40-7.33 (m, 5H), 7.30-7.27 (m, 1H), 6.32 (s, 1H), 5.35 (m, 1H), 3.45 (dd, *J* = 13.5 Hz, 10.0 Hz, 1H), 3.30 (dd, *J* = 14.0 Hz, 5.5 Hz, 1H), 1.85 (s, 3H). The ^{1}H NMR peaks are consistent with those reported in the literature.[42]

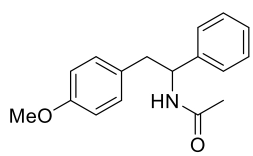

9b: yield: 55%. ^{1}H NMR (500 MHz, $CDCl_3$): δ 7.32-7.24 (m, 3H), 7.20-2.18 (m, 2H), 6.94 (d, *J* = 8.5 Hz, 2H), 6.76 (d, *J* = 8.5 Hz, 2H), 5.78 (d, *J* = 6.5 Hz, 1H), 5.23 (q, *J* = 7.5 Hz, 1H), 3.76 (s, 3H), 3.04 (d, *J* = 7.0 Hz, 2H), 1.94 (s, 3H). The ^{1}H NMR peaks are consistent with those reported in the literature.[42]

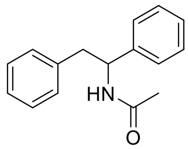

9c: yield: 76%. ^{1}H NMR (500 MHz, $CDCl_3$): δ 7.34-7.21(m, 8H), 7.09-7.07 (m,2H), 5.88 (d, *J* = 7.0 Hz, 1H), 5.40 (q, *J* = 7.5 Hz, 1H), 3.13 (d, *J* = 7.0 Hz, 2H), 1.96 (s, 3H). The ^{1}H NMR peaks are consistent with those reported in the literature.[42]

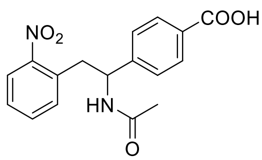

9d: yield: 76%. ^{1}H NMR (500 MHz, DMSO-d^6): δ 12.92 (s, 1H), 8.53 (d, *J* = 9.0 Hz, 1H), 7.96 (dd, *J* = 8.5 Hz, 1.2 Hz, 1H), 7.91 (d, *J* = 8.0 Hz, 2H), 7.65 (td, *J* = 7.5 Hz, 1.3 Hz, 1H), 7.49 (m, 2H), 7.43 (d, *J* = 8.0 Hz, 2H), 5.23 (m, 1H), 3.34 (2H, merged with H_2O), 3.09 (dd, *J* = 14.0 Hz, 9.0 Hz, 1H), 1.75 (s, 3H); ^{13}C NMR (125 MHz, DMSO-d^6): δ 168.59, 167.13, 149.23, 147.81, 133.10, 132.89, 132.77, 129.55, 129.52, 128.13, 126.52, 124.61, 52.50, 33.83, 22.53; ESI-MS: calc'd for $[M+H]^+$: 329.1; found 329.1.

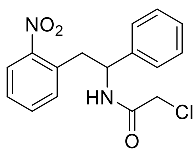

9e: yield: 62%. ^{1}H NMR (500 MHz, $CDCl_3$): δ 7.95-7.92 (m, 1H), 7.56 (td, *J* = 7.2 Hz, 1.0 Hz, 1H), 7.45 (d, *J* = 8.0 Hz, 1H), 7.43-7.36 (m, 6H), 7.34-7.29 (m, 1H), 5.37 (m, 1H), 3.91 (d, *J* = 15 Hz, 1H), 3.84 (d, *J* = 15 Hz, 1H), 3.47 (dd, *J* = 14 Hz, 10.5 Hz, 1H), 3.37 (dd, *J* = 13.5 Hz, 5.5 Hz, 1H). ^{13}C NMR (125 MHz, DMSO-d^6): δ 165.50, 149.95, 140.90, 133.41, 132.74, 132.60, 129.09, 128.25, 128.13, 126.42, 125.13, 55.07, 42.60, 38.96; ESI-MS: calc'd for $[M+H]^+$: 319.1; found 319.2.

2.5. References

(1) Ciamician, G. THE PHOTOCHEMISTRY OF THE FUTURE. *Science.* **1912**, *36*, 385.

(2) Narayanam, J. M. R.; Stephenson, C. R. J. Visible light photoredox catalysis: applications in organic synthesis. *Chem. Soc. Rev.* **2011**, *40*, 102-113.

(3) Deng, X.; Li, Z.; García, H. Visible Light Induced Organic Transformations Using Metal-Organic-Frameworks (MOFs). *Chem. Eur. J.* **2017**, *23*, 11189-11209.

(4) Shaw, M. H.; Twilton, J.; MacMillan, D. W. C. Photoredox Catalysis in Organic Chemistry. *J. Org. Chem.* **2016**, *81*, 6898-6926.

(5) Prier, C. K.; Rankic, D. A.; MacMillan, D. W. C. Visible Light Photoredox Catalysis with Transition Metal Complexes: Applications in Organic Synthesis. *Chem. Rev.* **2013**, *113*, 5322-5363.

(6) Ischay, M. A.; Anzovino, M. E.; Du, J.; Yoon, T. P. Efficient Visible Light Photocatalysis of [2+2] Enone Cycloadditions. *J. Am. Chem. Soc.* **2008**, *130*, 12886-12887.

(7) Narayanam, J. M. R.; Tucker, J. W.; Stephenson, C. R. J. Electron-Transfer Photoredox Catalysis: Development of a Tin-Free Reductive Dehalogenation Reaction. *J. Am. Chem. Soc.* **2009**, *131*, 8756-8757.

(8) Tyson, E. L.; Ament, M. S.; Yoon, T. P. Transition Metal Photoredox Catalysis of Radical Thiol-Ene Reactions. *J. Org. Chem.* **2013**, *78*, 2046-2050.

(9) Fukuzumi, S.; Kishi, T.; Kotani, H.; Lee, Y.-M.; Nam, W. Highly efficient photocatalytic oxygenation reactions using water as an oxygen source. *Nat. Chem.* **2010**, *3*, 38-41.

(10) Twilton, J.; Le, C.; Zhang, P.; Shaw, M. H.; Evans, R. W.; MacMillan, D. W. C. The merger of transition metal and photocatalysis. *Nat. Rev. Chem.* **2017**, *1*, 0052.

(11) Jouffroy, M.; Primer, D. N.; Molander, G. A. Base-Free Photoredox/Nickel Dual-Catalytic Cross-Coupling of Ammonium Alkylsilicates. *J. Am. Chem. Soc.* **2016**, *138*, 475-478.

(12) Blum, T. R.; Miller, Z. D.; Bates, D. M.; Guzei, I. A.; Yoon, T. P. Enantioselective photochemistry through Lewis acid–catalyzed triplet energy transfer. *Science.* **2016**, *354*, 1391.

(13) Miller, Z. D.; Lee, B. J.; Yoon, T. P. Enantioselective Crossed Photocycloadditions of Styrenic Olefins by Lewis Acid Catalyzed Triplet Sensitization. *Angew. Chem., Int. Ed.* **2017**, *56*, 11891-11895.

(14) Li, X.; Hao, Z.; Zhang, F.; Li, H. Reduced Graphene Oxide-Immobilized Tris(bipyridine)ruthenium(II) Complex for Efficient Visible-Light-Driven Reductive Dehalogenation Reaction. *ACS Appl. Mater. & Interfaces.* **2016**, *8*, 12141-12148.

(15) Kumar, P.; Sain, B.; Jain, S. L. Photocatalytic reduction of carbon dioxide to methanol using a ruthenium trinuclear polyazine complex immobilized on graphene oxide under visible light irradiation. *J. of Mater. Chem. A.* **2014**, *2*, 11246-11253.

(16) Chen, J.; Zhong, J.; Guo, Y.; Chen, L. Ruthenium complex immobilized on poly(4-vinylpyridine)-functionalized carbon-nanotube for selective aerobic oxidation of 5-hydroxymethylfurfural to 2,5-diformylfuran. *RSC Adv.* **2015**, *5*, 5933-5940.

(17) Qian, L.; Yang, X. R. One-Step Synthesis of Ru(2,2′-Bipyridine)$_3$Cl$_2$-Immobilized Silica Nanoparticles for Use in Electrogenerated Chemiluminescence Detection. *Adv. Funct. Mater.* **2007**, *17*, 1353-1358.

(18) Sardesai, N.; Pan, S.; Rusling, J. Electrochemiluminescent immunosensor for detection of protein cancer biomarkers using carbon nanotube forests and [Ru-(bpy)$_3$]$^{2+}$-doped silica nanoparticles. *Chem. Commun.* **2009**, 4968-4970.

(19) Wang, C.; Xie, Z.; deKrafft, K. E.; Lin, W. Doping Metal–Organic Frameworks for Water Oxidation, Carbon Dioxide Reduction, and Organic Photocatalysis. *J. Am. Chem. Soc.* **2011**, *133*, 13445-13454.

(20) Yu, X.; Cohen, S. M. Photocatalytic metal-organic frameworks for the aerobic oxidation of arylboronic acids. *Chem. Commun.* **2015**, *51*, 9880-9883.

(21) Yu, X.; Cohen, S. M. Photocatalytic Metal–Organic Frameworks for Selective 2,2,2-Trifluoroethylation of Styrenes. *J. Am. Chem. Soc.* **2016**, *138*, 12320-12323.

(22) Zhang, Z.-M.; Zhang, T.; Wang, C.; Lin, Z.; Long, L.-S.; Lin, W. Photosensitizing Metal–Organic Framework Enabling Visible-Light-Driven Proton Reduction by a Wells–Dawson-Type Polyoxometalate. *J. Am. Chem. Soc.* **2015**, *137*, 3197-3200.

(23) Wang, C.; deKrafft, K. E.; Lin, W. Pt Nanoparticles@Photoactive Metal–Organic Frameworks: Efficient Hydrogen Evolution via Synergistic Photoexcitation and Electron Injection. *J. Am. Chem. Soc.* **2012**, *134*, 7211-7214.

(24) Xie, M.-H.; Yang, X.-L.; Zou, C.; Wu, C.-D. A SnIV–Porphyrin-Based Metal–Organic Framework for the Selective Photo-Oxygenation of Phenol and Sulfides. *Inorg. Chem.* **2011**, *50*, 5318-5320.

(25) Fateeva, A.; Chater Philip, A.; Ireland Christopher, P.; Tahir Asif, A.; Khimyak Yaroslav, Z.; Wiper Paul, V.; Darwent James, R.; Rosseinsky Matthew, J. A Water-Stable Porphyrin-Based Metal–Organic Framework Active for Visible-Light Photocatalysis. *Angew. Chem., Int. Ed.* **2012**, *51*, 7440-7444.

(26) Wu, P.; He, C.; Wang, J.; Peng, X.; Li, X.; An, Y.; Duan, C. Photoactive Chiral Metal–Organic Frameworks for Light-Driven Asymmetric α-Alkylation of Aldehydes. *J. Am. Chem. Soc.* **2012**, *134*, 14991-14999.

(27) Chem. Rev.Dhakshinamoorthy, A.; Alvaro, M.; Hwang, Y. K.; Seo, Y.-K.; Corma, A.; Garcia, H. Intracrystalline diffusion in Metal Organic Framework during heterogeneous catalysis: Influence of particle size on the activity of MIL-100 (Fe) for oxidation reactions. *Dalton Trans.* **2011**, *40*, 10719-10724.

(28) Horike, S.; Dincă, M.; Tamaki, K.; Long, J. R. Size-Selective Lewis Acid Catalysis in a Microporous Metal-Organic Framework with Exposed Mn^{2+} Coordination Sites. *J. Am. Chem. Soc.* **2008**, *130*, 5854-5855.

(29) Wang, C.; Lin, W. Diffusion-Controlled Luminescence Quenching in Metal−Organic Frameworks. *J. Am. Chem. Soc.* **2011**, *133*, 4232-4235.

(30) Wang, C.; Wang, J.-L.; Lin, W. Elucidating Molecular Iridium Water Oxidation Catalysts Using Metal–Organic Frameworks: A Comprehensive Structural, Catalytic, Spectroscopic, and Kinetic Study. *J. Am. Chem. Soc.* **2012**, *134*, 19895-19908.

(31) Cao, L.; Lin, Z.; Peng, F.; Wang, W.; Huang, R.; Wang, C.; Yan, J.; Liang, J.; Zhang, Z.; Zhang, T.; Long, L.; Sun, J.; Lin, W. Self-Supporting Metal–Organic Layers as Single-Site Solid Catalysts. *Angew. Chem., Int. Ed.* **2016**, *55*, 4962-4966.

(32) Lin, Z.; Thacker, N. C.; Sawano, T.; Drake, T.; Ji, P.; Lan, G.; Cao, L.; Liu, S.; Wang, C.; Lin, W. Metal-organic layers stabilize earth-abundant metal-terpyridine diradical complexes for catalytic C-H activation. *Chem. Sci.* **2018**, *9*, 143-151.

(33) Shi, W.; Cao, L.; Zhang, H.; Zhou, X.; An, B.; Lin, Z.; Dai, R.; Li, J.; Wang, C.; Lin, W. Surface Modification of Two-Dimensional Metal–Organic Layers Creates Biomimetic Catalytic Microenvironments for Selective Oxidation. *Angew. Chem., Int. Ed.* **2017**, *56*, 9704-9709.

(34) Du, J.; Espelt, L. R.; Guzei, I. A.; Yoon, T. P. Photocatalytic reductive cyclizations of enones: Divergent reactivity of photogenerated radical and radical anion intermediates. *Chem. Sci.* **2011**, *2*, 2115-2119.

(35) Cavka, J. H.; Jakobsen, S.; Olsbye, U.; Guillou, N.; Lamberti, C.; Bordiga, S.; Lillerud, K. P. A New Zirconium Inorganic Building Brick Forming Metal Organic Frameworks with Exceptional Stability. *J. Am. Chem. Soc.* **2008**, *130*, 13850-13851.

(36) Peterson, G. W.; Moon, S.-Y.; Wagner, G. W.; Hall, M. G.; DeCoste, J. B.; Hupp, J. T.; Farha, O. K. Tailoring the Pore Size and Functionality of UiO-Type Metal–Organic Frameworks for Optimal Nerve Agent Destruction. *Inorg. Chem.* **2015**, *54*, 9684-9686.

(37) Chavan, S.; Vitillo, J. G.; Gianolio, D.; Zavorotynska, O.; Civalleri, B.; Jakobsen, S.; Nilsen, M. H.; Valenzano, L.; Lamberti, C.; Lillerud, K. P.; Bordiga, S. H2storage in isostructural UiO-67 and UiO-66 MOFs. *Phys. Chem. Chem. Phys.* **2012**, *14*, 1614-1626.

(38) Du, J.; Yoon, T. P. Crossed Intermolecular [2+2] Cycloadditions of Acyclic Enones via Visible Light Photocatalysis. *J. Am. Chem. Soc.* **2009**, *131*, 14604-14605.

(39) Sun, X.; Wick, C. D.; Thallapally, P. K.; McGrail, B. P.; Dang, L. X. Molecular mechanism of hydrocarbons binding to the metal–organic framework. *Chem. Phys. Lett.* **2011**, *501*, 455-460.

(40) Okamura, T.; Obi, T.; Tanaka, I. The flourescence lifetime of the benzyl radical. *Chem. Phys. Lett.* **1974**, *26*, 218-220.

(41) Valencia, D. P.; González, F. J. Understanding the linear correlation between diffusion coefficient and molecular weight. A model to estimate diffusion coefficients in acetonitrile solutions. *Electrochem. Commun.* **2011**, *13*, 129-132.

(42) Prasad Hari, D.; Hering, T.; König, B. The Photoredox-Catalyzed Meerwein Addition Reaction: Intermolecular Amino-Arylation of Alkenes. *Angew. Chem., Int. Ed.* **2014**, *53*, 725-728.

(43) Yang, J.; Felton, G. A. N.; Bauld, N. L.; Krische, M. J. Chemically Induced Anion Radical Cycloadditions: Intramolecular Cyclobutanation of Bis(enones) via Homogeneous Electron Transfer. *J. Am. Chem. Soc.* **2004**, *126*, 1634-1635.

(44) Massari, S.; Desantis, J.; Nannetti, G.; Sabatini, S.; Tortorella, S.; Goracci, L.; Cecchetti, V.; Loregian, A.; Tabarrini, O. Efficient and regioselective one-step synthesis of 7-aryl-5-methyl- and 5-aryl-7-methyl-2-amino-[1,2,4]triazolo[1,5-a]pyrimidine derivatives. *Org. Biomol. Chem.* **2017**, *15*, 7944-7955.

(45) van Zijl, A. W.; Minnaard, A. J.; Feringa, B. L. Straightforward Synthesis of α,β-Unsaturated Thioesters via Ruthenium-Catalyzed Olefin Cross-Metathesis with Thioacrylate. *J. Org. Chem.* **2008**, *73*, 5651-5653.

(46) Hanson, P.; Jones, J. R.; Taylor, A. B.; Walton, P. H.; Timms, A. W. Sandmeyer reactions. Part 7.1 An investigation into the reduction steps of Sandmeyer hydroxylation and chlorination reactions. *J. Chem. Soc., Perkin Trans. 2.* **2002**, 1135-1150.

CHAPTER 3. Metal-Organic Layers Efficiently Catalyze Photoinduced Polymerization under Visible Light

3.1 Introduction

Chapter 2 describes our efforts on using $Ru(bpy)_3^{2+}$-based MOLs in catalyzing several organic transformations under visible light irradiation. We found that MOL catalysts are superior to MOF catalysts in these photoreactions due to the removal of pore size and diffusion constraints. In this chapter, I will report $Ir(ppy)_2(bpy)^+$-based MOL, IrBPY-MOL, as a heterogeneous photocatalyst with enhanced activities for photopolymerization.

Photopolymerization, which forms the basis of numerous applications in areas such as biomedical materials,[1-3] optical waveguides,[4,5] microelectronics,[6] 3D printing[7-9] and other,[10-12] has received revitalized interest in recent years and been extensively studied. Photopolymerization processes sometimes do not require the use of solvents, have low energy consumptions, and can proceed at ambient temperature in short reaction times,[13-18] presenting potentially important economic and environmental advantages. Most photopolymerizations occur via chain-growth polymerization where light is absorbed either directly by reactants (direct polymerization) or by a photosensitizer to generate radicals or cations as reactive species. In many cases, direct polymerization is not effective because organic monomers do not readily absorb light. A photoinitiator is introduced to the polymerization system, which can generate reactive species upon light irradiation. Common photoinitiators include amines,[19] ethers,[20] thios,[21,22] cationium compounds,[23-25] and alkyl halides.[26-28] Sometimes a photosensitizer is also required to increase spectral sensitivity, whose role is to absorb light at a wavelength where the photoinitiator is unable to operate and transfer the absorbed energy or electrons to surrounding photoinitiators which initiate monomer additions.

Traditional photocatalysts used as photosensitizers in photopolymerization include benzophenone,[29,30] camphorquinone,[19] and thioxanthone derivatives[31,32] which mainly absorb UV light. Polymerization systems that utilize light in the visible region (390–700 nm) are more cost-effective and environmentally benign, with minimal side reactions due to lack of background absorption from organic solvents and monomers. Some representative visible-light photocatalysts for photopolymerization comprise small-molecule organic dyes (erosin, methylene blue, etc.),[33,34] metal complexes,[35-37] and semiconductors (CdS,[38] Fe_3O_4[39]). Among them, cyclometallated iridium complexes, similar to $Ru(bpy)_3^{2+}$-based complexes mentioned in Chapter 2, draw great attention as SET photoredox catalysts in organic transformations due to their strong absorbance, good solubility, chemical stability, and long-lived excited-state.[40-43] In 2012, Lalevée *et al*. demonstrated the use of $Ir(ppy)_3^{2+}$- and $Ir(ppy)_2(bpy)^+$-based photocatalysts in free radical polymerization of pentaerythritol tetraacrylate.[28] In the same year, Hawker *et al*. applied *fac*-$Ir(ppy)_3$ to atom-transfer radical polymerization (ATRP) of methyl methacrylate (MMA), achieving controlled living feature with perfect temporal control in the absence/presence of light.[37] Since then, more researches on Ir-based complexes as photocatalysts have been reported.[44-46]

It is favorable to heterogenize and recycle iridium complexes out of economic considerations. Our group first incorporated $Ir(ppy)_2(bpy)_2^+$ into UiO-67 MOF for organic catalysis.[47] Similar strategies have been employed to construct more sophisticated catalytic MOF systems (together with PtNP and POM) for hydrogen evolution reaction,[48,49] which showed good efficacy and recyclability. As shown in Chapter 2, MOFs have intrinsic drawbacks as photocatalysts owing to pore size limitation and diffusion limitation in multicomponent photoreactions, as well as light scattering and penetrating issues. In comparison, MOLs can effectively overcome these problems as a well-dispersed, 2D ultrathin material with only 1-2 nm in thickness.[50] The geometric features of MOLs can be especially beneficial for polymerization – all the substrates, intermediates, oligomers and the growing chains can have free access to active sites without spatial confinement just like homogeneous catalysts (**Figure 3-1**). In this chapter, we synthesized IrBPY-MOL by postsynthetic metalation of BPY-MOL and studied the use of IrBPY-MOLs in photopolymerization in comparison with the IrUiO-69 MOF control.[48,51] IrUiO-69 is a Hf-oxo based MOF with large pores which can easily accommodate most small molecules. In the case of photopolymerization of MMA and other monomers, IrBPY-MOL showed superior photocatalytic activity than IrUiO-69, affording polymers with a high-number-average molar mass and low polydispersity index.

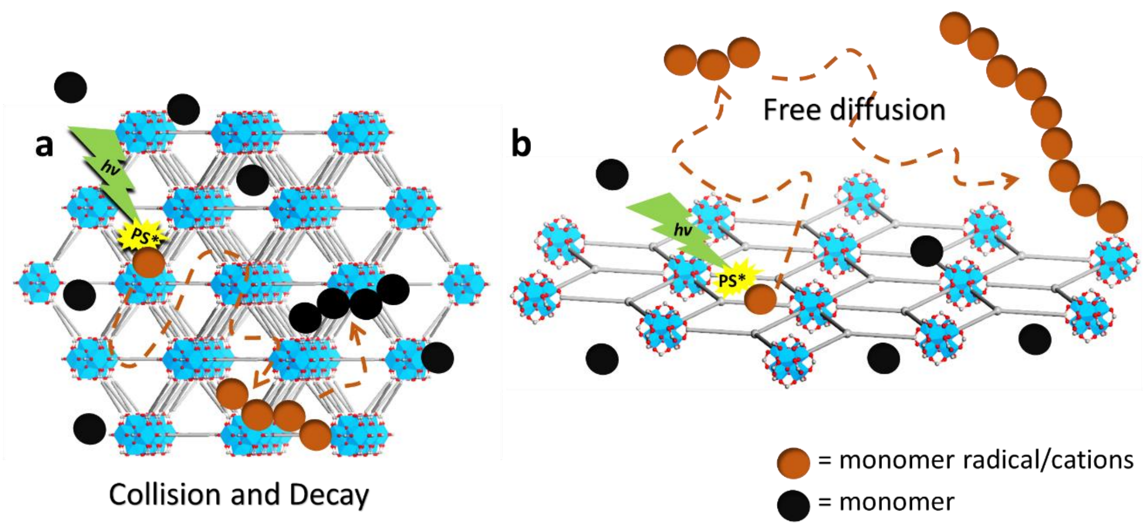

Figure 3-1. Photoactive MOFs (a) and MOLs (b) catalyzed photopolymerization.

3.2 Results and Discussion

3.2.1 Synthesis and Characterization of BPY-MOL and IrBPY-MOL

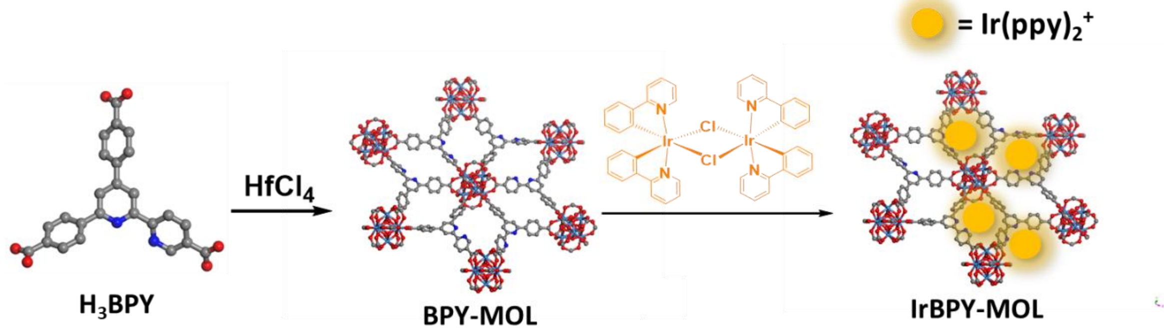

Scheme 3-1. Synthetic scheme of BPY-MOL and IrBPY-MOL.

IrBPY-MOL was synthesized according to **Scheme 3-1**. First, H_3BPY heated with $HfCl_4$ in a mixed solvent of DMF/H_2O/HCOOH under solvothermal conditions (120 °C) to afford BPY-MOL as a white solid. The resulting BPY-MOL comprises Hf_6 clusters in substitution of previous Zr_6 clusters as reported in Chapter 2. Considering their isoreticular structure, we are using the term "BPY-MOL" to describe the Hf-BPY MOL in this chapter. The as-prepared BPY-MOL was then reacted with iridium dimers, $Ir_2(ppy)_4Cl_2$, in a mixed solvent of MeOH/DMF at 70 ºC for two days. The mixture color changed from pale yellow to orange, indicating the formation of IrBPY-MOL. TEM showed well-dispersed, wrinkled, sheet-like morphology of BPY-MOL with the size of a few hundred nanometers (**Figure 3-2a**), which remained intact in IrBPY-MOL without observable degradation (**Figure 3-2b**). PXRD of BPY-MOL and IrBPY-MOL both displayed good crystallinity with characteristic patterns of two-dimensional kgd topology (**Figure 3-2c**). ICP-MS data confirmed metalation with Ir with the Ir loading of 78 mol%, giving the empirical formula of IrBPY-MOL as $Hf_6(\mu_3\text{-}O)_4(\mu_3\text{-}OH)_4(HCO_2)_6(BPY)_2[Ir(ppy)_2Cl]_{1.56}$.

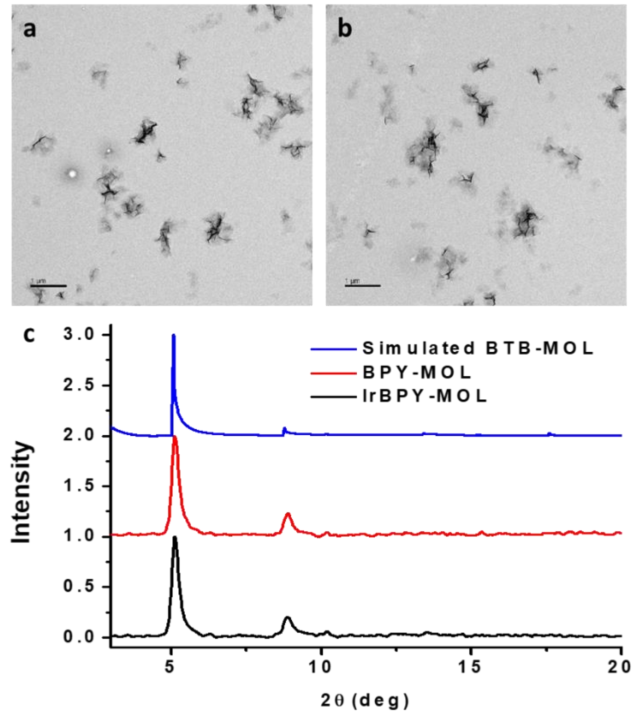

Figure 3-2. Structures and morphologies of BPY-MOL and IrBPY-MOL. (a) TEM image of BPY-MOL (scale bar: 1 μm); (b) TEM image of IrBPY-MOL (scale bar: 1 μm); (c) PXRD patterns of BPY-MOL, IrBPY-MOL, and simulated BTB-MOL.

We tested the photophysics property of the IrBPY-MOL in order to better understand its potential in catalyzing photopolymerization. The UV-vis spectrum of BPY-MOL in DMF showed a main peak at 290 nm with a shoulder peak at 322 nm (**Figure 3-3**). After metalation, the absorption of IrBPY-MOL extends to visible region, which has similar features as the IrBPY ligand (**Figure 3-3**). The shoulder peak at 410 nm, which is attributed to singlet metal-to-ligand (^{1}MLCT) charge transfer of the Ir photophore,[52] was selected as excitation wavelength. Photoluminescence spectrum of free IrBPY in DMF shows two signature peaks as reported for $Ir(ppy)_2(bpy)$[52] (**Figure 3-4a**). The orange main peak centered at 590 nm is assigned to triplet metal-to-ligand bpy charge transfer ($^3MLCT_{bpy}$). The green shoulder peak centered at 510 nm is assigned to triplet metal-to-ligand ppy charge transfer ($^3MLCT_{ppy}$). When we measured the emission of IrBPY-MOL with the same Ir- concentration, the intensity of the green band remained the same but the orange emission was heavily quenched (**Figure 3-4a**). Emission intensity was proportional to concentration in the measured concentration region. We also tried different solvents including DMF, $CHCl_3$, and toluene, the 590nm peak of IrBPY-MOL was all quenched to certain extent in these solvent (**Figure 3-4b)**.

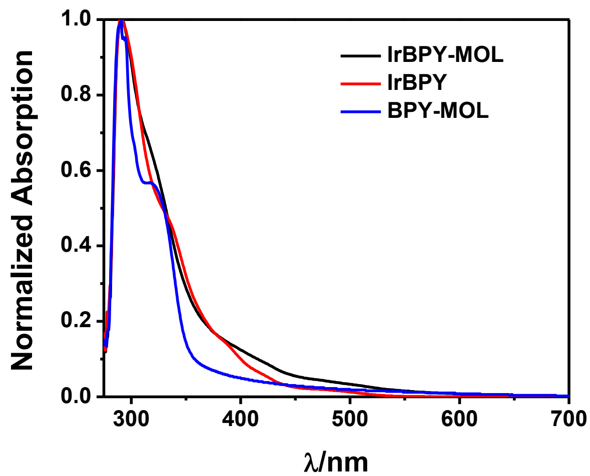

Figure 3-3. UV-vis spectra of IrBPY, BPY-MOL and IrBPY-MOL.

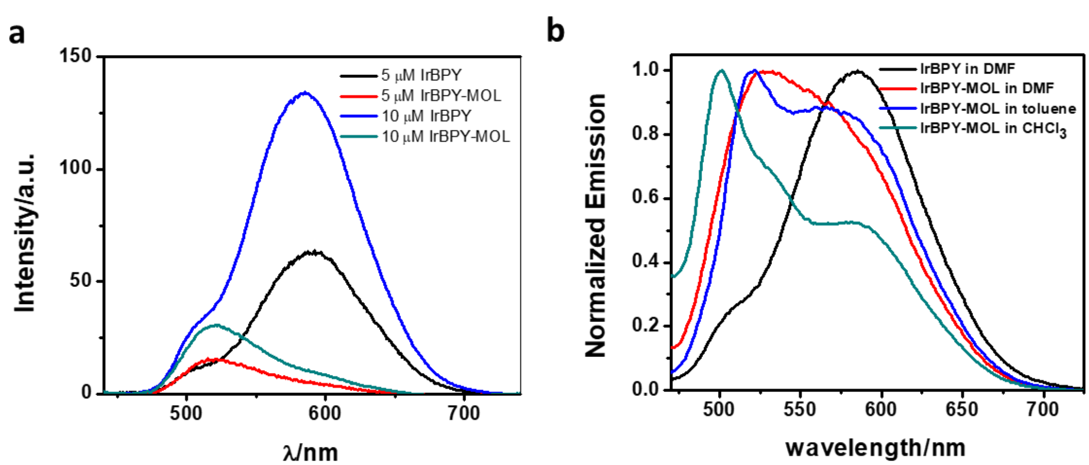

Figure 3-4. (a) Emission spectra of IrBPY and IrBPY-MOL in DMF with different concentration; (b) Emission spectra of IrBPY-MOL in different solvent.

In transient photoluminescence spectroscopy, we observed a mono-exponential decay for the orange band in IrBPY with a lifetime of τ = 246 ns, but bi-exponential decay in IrBPY-MOL with reduced lifetimes of τ' = 125 ns, τ' = 12 ns (**Figure 3-5**). Both the steady-state and transient photoluminescence data indicated the presence of other decay pathways of $^3MLCT_{bpy}$ state in IrBPY-MOL. Considering the redox potentials of Ir(IV)/Ir*(III) ($E_{Ir(IV)/Ir^*(III)}$ = -0.96 V vs SCE)[53] and Hf(IV)/Hf(III) ($E_{Hf(IV)/Hf(III)} < E_{Zr(IV)/Zr(III)}$ = -1.06 V vs SCE)[54,55], the electron transfer from excited-state ligand to Hf cluster is unlikely. This is also supported by electron paramagnetic resonance (EPR) results which showed signals with g = 2.001 corresponding to organic radicals but no signals attributable to Hf(III) from IrBPY-MOL under irradiation (**Figure 3-6**). The organic radical may be ligand-based or from reduction of HCOOH capping agents. This conclusion is consistent with previous investigation on electronic origins of Zr/Hf based UiO-MOF.[56]

a

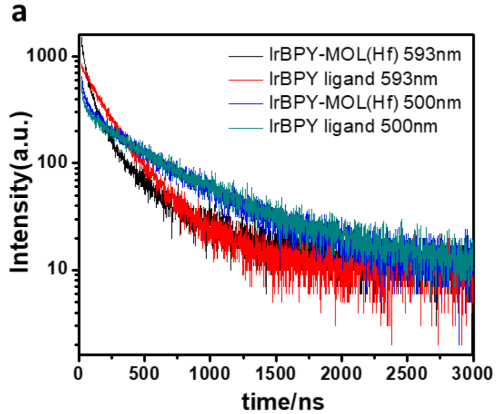

b

Entry	t_1 (ns)	t_2 (ns)
IrBPY-MOL(Hf) 593 nm	125	12
IrBPY ligand 593 nm	246	\
IrBPY-MOL(Hf) 500 nm	509	21
IrBPY ligand 500 nm	552	11

Figure 3-5. Photoluminescence decay transients (a) and lifetime data (b) of IrBPY ligand and IrBPY-MOL.

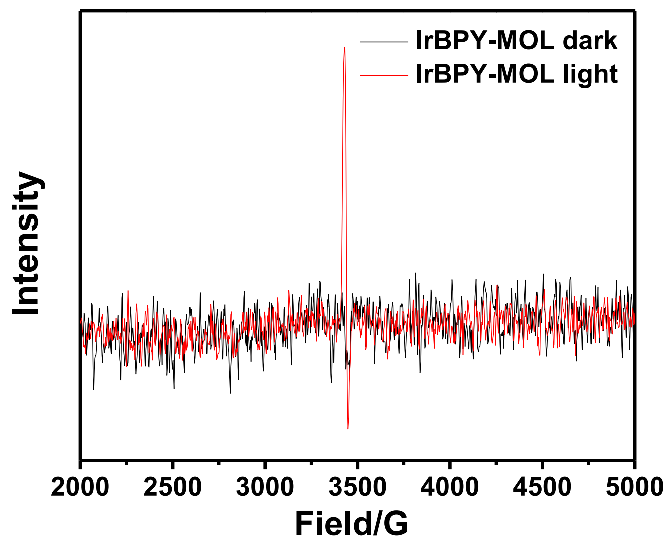

Figure 3-6. EPR spectra of IrBPY-MOL in dark (black) and under light irradiation (red).

3.2.2 Synthesis and Characterization of IrUiO-69

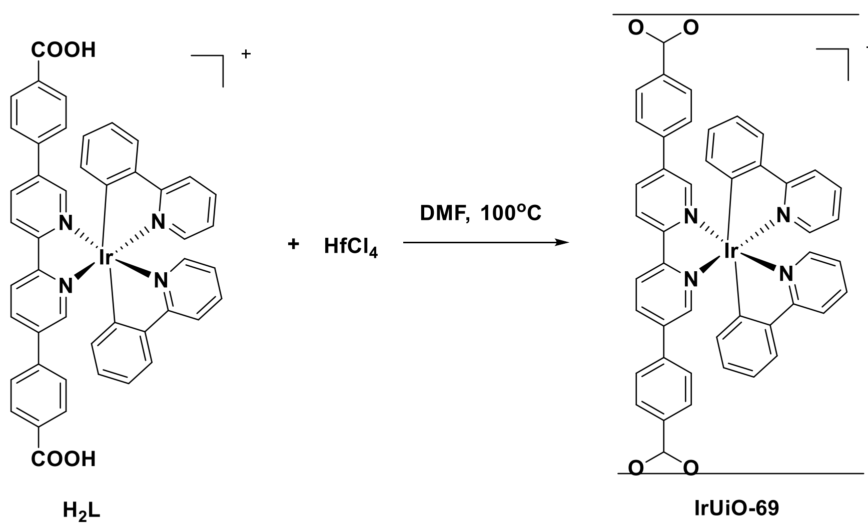

Scheme 3-2. Synthesis of IrUiO-69.

IrUiO-69 was synthesized from ligand H_2L using a modified procedure of previous report.[48] Briefly, H_2L and $HfCl_4$ were dissolved in DMF. Trifluoroacetic acid was added as a modulator. The mixture was kept in a 100 ˚C oven for 4 days to afford the orange product of IrUiO-69. PXRD studies showed that IrUiO-69 adopted a UiO structure with good crystallinity (**Figure 3-7**).

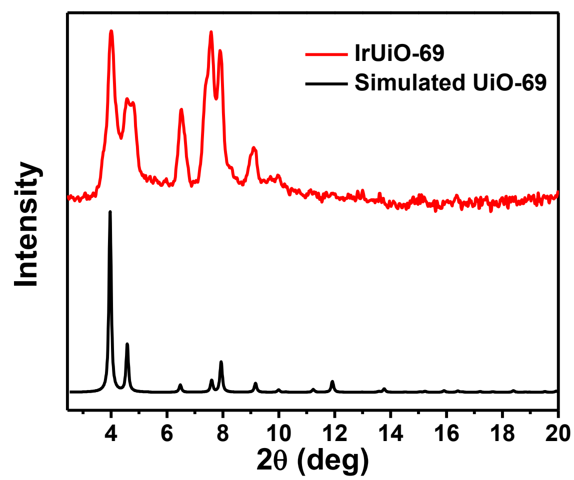

Figure 3-7. PXRD patterns of IrUiO-69 (red) and simulated UiO-69 (black).

3.2.3 IrBPY-MOL Catalyzed Photopolymerization

We studied the photoactivity of IrBPY-MOL in the polymerization of (MMA). A blue 410 nm LED was used as light source. Using a classical ATRP condition,[37] the reaction was performed in DMF with ethyl α-bromophenylacetate (EBP) as co-initiator. The polymerization was believed to be initiated by alkyl radical generated from reduction of EBP by excited state Ir(III)* species (**Scheme 3-3**). The oxidative Ir(IV) complex can then react with the propagating radical to afford initial Ir(III) and a dormant polymer chain with the bromo end group. This process is then repeated to lead to a light-mediated controlled ATRP process.

With 0.02 mol% loading of IrBPY-MOL, poly(methyl methacrylate) (PMMA) was formed after two days in 78% yield, a reasonably high molecular weight (Mn) of 17,100 g/mol (theoretical: 15,600 g/mol) and a low polydispersity index (PDI) of 1.27 (**Table 3-1**, Entry 1a). These results suggested the living nature of the polymerization process in the presence of EBP initiator[57]. Control experiments in the absence of either IrBPY-MOL or light did not afford any polymer (**Table 3-1**, Entry 1b, 1c). We also tested the activity of IrBPY and IrUiO-69 under the same condition; PMMA was obtained with 66% and 40% yield, respectively (**Table 3-1**, Entry 1d, 1e). We further extended the scope of monomer substrate to benzyl methacrylate (BMA) and *tert*-butyl methacrylate (*t*BuMA). In each case the polymer was obtained with high molecular weight (10,500~28,800 g/mol) and relatively uniform MW distribution (PDI = 1.26 -1.46, **Table 3-1**, Entry 2a~2c, 3a~3c). The yields (78%, 64%, and 59%) and Mn's (16,200 g/mol, 25,300 g/mol, and 28,800 g/mol) of the polymers generated by IrBPY-MOL are significantly higher than those by IrUiO-69 (40%, 30%, and 33% in yields and 10,500 g/mol, 15,400 g/mol, and 15,800 g/mol in molecular weights) but similar to those by IrBPY (66%, 47%, and 45% in yields and 15,100g/mol, 25,100 g/mol, and 28,800 g/mol in molecular weights). These results indicate superior photocatalytic activity of IrBPY-MOL over the MOF counterpart in living polymerization, likely due to enhanced reactant diffusion in 2D MOLs.

Table 3-1. Conversion and molecular weight of poly(methyl methacrylate), poly(benzyl methacrylate) and poly(*tert*-butyl methacrylate) with different photocatalysts in the presence of ethyl α-bromophenylacetate coinitiator.*

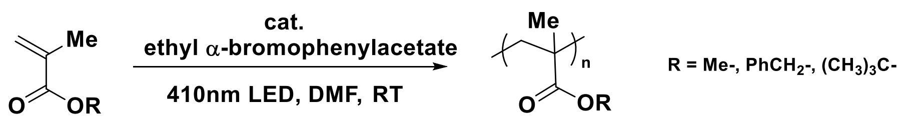

Entry	Monomer	Catalyst	Conversion	Mn	PDI
1a	MMA	IrBPY-MOL	78%	16.2k	1.27
1b**	MMA	none	n.d.	n.a.	n.a.
1c***	MMA	IrBPY-MOL	n.d.	n.a.	n.a.
1d	MMA	IrBPY	66%	15.1k	1.36
1e	MMA	Ir-UiO69	40%	10.5k	1.33
2a	BnMA	IrBPY-MOL	64%	25.3k	1.26
2b	BnMA	IrBPY	47%	25.1k	1.40
2c	BnMA	Ir-UiO69	30%	15.4k	1.27
3a	*t*BuMA	IrBPY-MOL	59%	28.8k	1.34
3b	*t*BuMA	IrBPY	45%	21.1k	1.38
3c	*t*BuMA	Ir-UiO69	33%	15.8k	1.46

*Reaction conditions: MMA (1equiv.), ethyl α-bromophenylacetate (EBP, 0.5% mol), catalyst (IrBPY-MOL, IrBPY, or IrUiO-69, 0.02% mol) in DMF (MMA:DMF = 1:3.5 v/v) at room temperature irradiated with a 410nm LED for 2 days. Light intensity at the reaction vessel was maintained at 5 mW/cm^2. **The reaction was run in the absence of photocatalysts. ***The reaction was run in the absence of light. M_n = number average molecular weight. PDI = polydispersity index. n.d. = not detected. n.a. = not applicable.

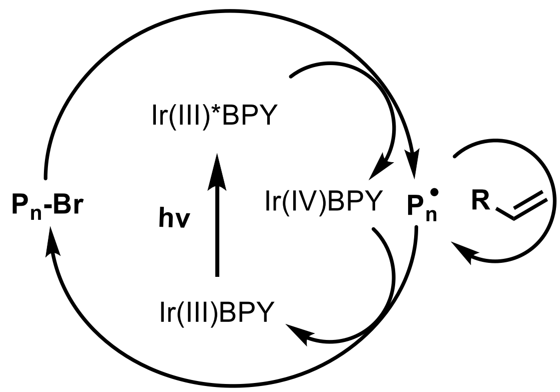

Scheme 3-3. Proposed mechanism for IrBPY-MOL catalyzed living polymerization.

We also demonstrated the recyclability of IrBPY-MOL as a heterogeneous photocatalyst in living polymerization of MMA. After each reaction, IrBPY-MOL was isolated by centrifugation and washed several times to remove reactant residues. As 2D materials, MOLs do not trap contaminant guest molecules. The recovered MOL was directly used as the photocatalyst for the next run. The crystallinity of IrBPY-MOL was retained after at least five cycles as indicated by PXRD patterns (**Figure 3-8**), minimal loss of polymerization yields, and no reduction of molecular weights (**Table 3-2**).

Table 3-2. Recycle and reuse of IrBPY-MOL in photocatalytic MMA polymerization with EBP as coinitiator*

Monomer	Cycle	Conversion	Mn	PDI
MMA	1	78%	16.2k	1.27
	2	72%	15.9k	1.30
	3	64%	14.9k	1.28
	4	68%	14.9k	1.27
	5	64%	14.8k	1.32

*Reaction conditions: MMA (1 equiv.), EBP (0.5 mol%), IrBPY 0.02 mol% in DMF (MMA:DMF=1:3.5 v/v) at room temperature irradiated with a 410nm LED for 2 days. Light intensity at the reaction vessel was maintained at 5 mW/cm^2.

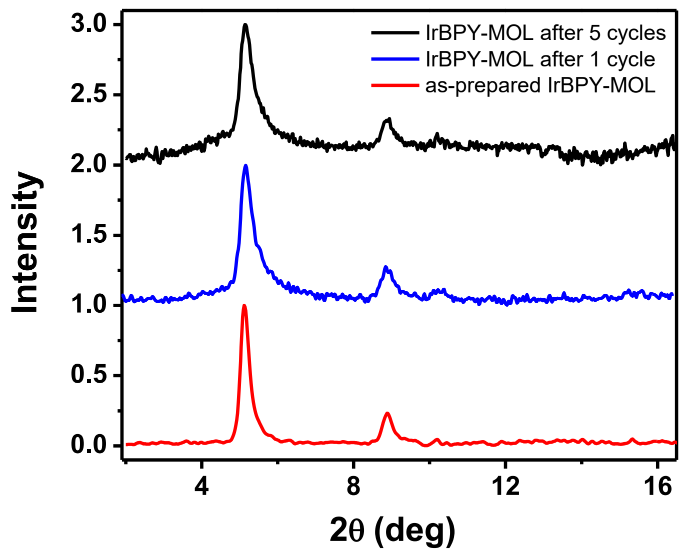

Figure 3-8. PXRD patterns of IrBPY-MOL after five consecutive recycles of photocatalytic MMA polymerization.

Interestingly, we found that the polymerization process still proceeded in the absence of EBP. The photpolymerization in the absence of EBP is an uncontrolled process. We reoptimized the condition by increasing monomer concentration from 1:3 to 1:1 v/v and reducing light intensity from 5 mW/cm^2 to 2 mW/cm^2. Polymers with high molecular weight (59,900 g/mol) and large PDI (1.96) were obtained after two days (**Table 3-3**, Entry 1a). As shown in **Table 3-3**, (Entry 1b, 1c), IrBPY-MOL and light were both essential for the polymerization reaction (**Table 3-3**, Entry 1b, 1c). Interestingly, IrBPY and IrUiO-69 failed to polymerize MMA under the same conditions (**Table 3-3**, Entry 1d, 1e). We also ran the reaction in different organic solvents to gain a better understanding of this polymerization process (**Table 3-3**). Due to its limited solubility, IrBPY could only be tested for polymerization in DMA. IrBPY-MOL catalyzed the photopolymerization in polar solvents such as dimethyl acetamide (DMA), tetrahydrofuran (THF), dioxane, and ethanol,

Table 3-3. Conversion and molecular weight of polymerization of methyl methacrylate in various solvents with different photocatalysts in the absence of ethyl α-bromophenylacetate.*

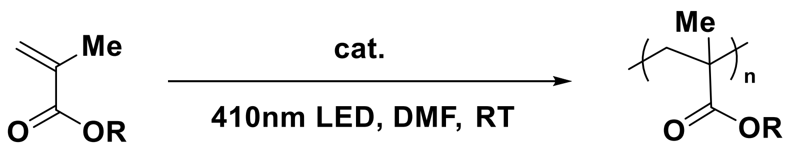

Entry	Catalyst	solvent	Conversion	Mn	PDI
1a	IrBPY-MOL	DMF	65%	59.9k	1.96
1b**	none	DMF	n.d.	n.a.	n.a.
1c***	IrBPY-MOL	DMF	n.d.	n.a.	n.a.
1d	IrBPY	DMF	n.d.	n.a.	n.a.
1e	Ir-UiO69	DMF	n.d.	n.a.	n.a.
2a	IrBPY-MOL	DMA	52%	111k	1.79
2b	IrBPY	DMA	n.d.	n.a.	n.a.
2c	Ir-UiO69	DMA	n.d.	n.a.	n.a.
3a	IrBPY-MOL	THF	81%	91.4k	2.18
3b	Ir-UiO69	THF	13%	14.0k	2.59
4a	IrBPY-MOL	dioxane	42%	78.7k	2.36
4b	Ir-UiO69	dioxane	n.d.	n.a.	n.a.
5a	IrBPY-MOL	toluene	n.d.	n.a.	n.a.
5b	Ir-UiO69	toluene	n.d.	n.a.	n.a.
6a	IrBPY-MOL	EtOH	98%	98.7k	2.25
6b	Ir-UiO69	EtOH	n.d.	n.a.	n.a.
7a****	IrBPY-MOL	\	n.d.	n.a.	n.a.
7b****	Ir-UiO69	\	n.d.	n.a.	n.a.

*Reaction conditions: MMA (1 equiv.), catalysts (IrBPY-MOL, IrBPY or IrUiO-69, 0.02 mol%) in different solvents (MMA:solvent = 1:3.5 v/v) at room temperature irradiated with a 410 nm LED for 2 days. Light intensity at the reaction vessel was maintained at 2 mW/cm^2. **The reaction was run in the absence of photocatalysts. ***The reaction was run in the absence of light. ****The reaction was run in bluk MMA solution. M_n = number average molecular weight. PDI = polydispersity index. n.d. = not detected. n.a. = not applicable.

but did not produce polymers in toluene and in neat MMA. Consequently, the solvent must play a role in the polymerization process. IrBPY and IrUiO-69 did not catalyze the formation of PMMA under the same conditions. IrUiO-69 catalyzed the formation of PMMA in a very low yield conversion of 13% in THF. We also tested the photopolymerization of BMA and obtained similar results as MMA (**Table 3-4**).

Table 3-4. Conversion and molecular weight of polymerization of benzyl methacrylate in various solvent with different photocatalysts in the absence of ethyl α-bromophenylacetate.*

Entry	Catalyst	solvent	Conversion	Mn	PDI
1a	IrBPY-MOL	DMF	45%	173k	1.81
1b	IrBPY	DMF	0	-	-
1c	Ir-UiO69	DMF	0	-	-
2a	IrBPY-MOL	DMA	63%	143k	1.91
2b	IrBPY	DMA	0	-	-
2c	Ir-UiO69	DMA	0	-	-
3a	IrBPY-MOL	THF	98%	137k	1.75
3b	Ir-UiO69	THF	15%	46.8k	3.60
4a	IrBPY-MOL	Dioxane	38%	133k	2.08
4b	Ir-UiO69	Dioxane	0	-	-
5a	IrBPY-MOL	toluene	0	-	-
5b	Ir-UiO69	toluene	0	-	-

*Reaction conditions: BMA (1 equiv.), catalysts (IrBPY-MOL, IrBPY or IrUiO-69, 0.02 mol%) in different solvent (1:1 v/v) at room temperature irradiated with a 410 nm LED for 2 days. Light intensity at the reaction vessel was maintained at 2 mW/cm^2.

As MMA has a very negative reduction potential of -2.1 V and a very positive oxidation potential of 2.0 V vs SCE,[38] Ir*(III) cannot oxidize or reduce the methacrylate monomer directly to initiate the chain reaction ($E_{Ir*(III)/Ir(II)}$ = 0.66~0.97V vs SCE, $E_{Ir(IV)/Ir*(III)}$ = -0.96V vs SCE)[53]. The initiation step likely originates from a SET process between Ir*(III) and impurity residues in solvent, decomposed amine from DMF or dimethylacetamide (DMA), or chelating HCOOH in Hf-clusters to generate active radical species followed by chain propagation. Although the mechanism is not clear yet, IrBPY-MOL is more effective and powerful photocatalyst for the polymerization of MMA and BMA in the absence of EBA than IrBPY and IrUiO-69.

3.3 Conclusion

In this chapter, we reported the synthesis of a photoactive 2D MOL, IrBPY-MOL, by incorporating cylcometalated iridium complex into a BPY-MOL backbone. The $^3MLCT_{bpy}$ emission of IrBPY-MOL was quenched in both static and transient emission spectra. IrBPY-MOL showed high activity for photopolymerization of various monomers, but IrUiO-69 failed to photopolymerize under identical conditions. The drastically different photocatalytic activities between MOLs and MOFs are likely a result of uninhibited diffusion for the 2D MOL structures. The IrBPY-MOL catalyst was also recycled and used for at least five runs without significant loss of activities. This study highlights the potential of MOLs as an outstanding photopolymerization catalyst.

3.4 Methods and Experimental Details

Chemicals and reagents: 2-bromo-5-methylpyridine and 4-carboxybenzaldehyde were purchased from Chem-Impex Int'l Inc. 4'-Methylacetophenone was purchased from Acocado Research Chemicals Ltd. Methyl methacrylate (99%) and pyridine were purchased from Acros Organic. Benzyl methacrylate (98%), dixoane (99%), and $HfCl_4$ were purchased from Alfar Aesar. tert-Butyl methacrylate (98%), *n*-Butyl lithium (2.5 M in hexanes), dimethylacetamide (anhydrous, 99.8%), iodine, and potassium permangnate were purchased from Sigma Aldrich. Tetrahydrofuran (99.9%), dimethylformamide (99.9%), and toluene (99.9%) were purchased from Fisher Scientific. Ethanol (99.9%) was purchased from Decon Labs. Inc. $CDCl_3$ and dimethyl sulfoxide-d_6 were purchased from Cambridge Isotope. $Ir_2(ppy)_4Cl_2$ and iridium ligand H_2L was synthesized as previously reported.[47,48]

Methods and Techniques: ^{1}H NMR spectra were acquired on a Bruker Avance II+ 500 NMR spectrometer. The Hf and Ir content in IrBPY-MOL were determined by inductively coupled plasma mass spectrometry (ICP-MS, Agilent 7700x, USA). The sample was digested by a mixture of concentrated nitric acid, hydrochloric acid, and hydrofluoric acid (90 : 5 : 5 v/v/v) using microwave-assisted digestion (200 ˚C, 30 min, MARS 6 230/60, Matthews. NC, USA). UV-vis spectra were recorded with a Shimadzu UV-2600 UV-vis spectrophotometer. Photoluminescence spectra were recorded with a Shimadzu RF-5301PC spectrofluorophotometer. The photoluminescence decay was measured with a ChromsBH lifetime fluorimeter (ISS, Inc.). A 405 nm laser was used as the excitation source. The time-lapse emission intensity of two different wavelength (500 ± 24 nm and 593 ± 40 nm) were monitored on nanosecond scale, respectively. Transmission electron microscopy (TEM, Tecnai Spirit, FEI, USA) was utilized to confirm the morphology of IrBPY-MOL. Powder X-ray diffraction (PXRD) patterns of the samples were collected on a Bruker D8 Venture, dual microsource (Cu and Mo) diffractometer with a CMOS detector. Cu Kα radiation was used. Electron Paramagnetic Resonance (EPR) Spectroscopy was performed with a Bruker Elexsys 500 X-band EPR spectrometer. The temperature of the samples was held at 15K using an Oxford Systems continuous-flow He Cryostat coupled with a 10K He stinger from Bruker. An external light source (Micro Lite FL3000) with an optical fiber was used to excite IrBPY-MOL during EPR measurements. The polymerization yield was determined by the integration ratio between monomer and polymer in ^{1}HNMR. Molecular weights and PDI of the polymer product were determined by gel permeation chromatography (GPC) with a Waters Associates liquid chromatography equipped with a Waters 510 HPLC pump, a Waters 410 differential refractometer, and a Waters 460 tunable absorbance detector. $CHCl_3$ was used as the eluent and polystyrene as the standard. Photopolymerization experiments were performed under the irradiation of a 410nm blue LED (IM101C121M Potrans power supply). The light intensity was determined by optical power meter (PM100D, Thorlabs).

Synthesis of iridium(III) 4',6'-dibenzoato-(2,2'-bipyridine)-4-carboxylic acid (IrBPY)

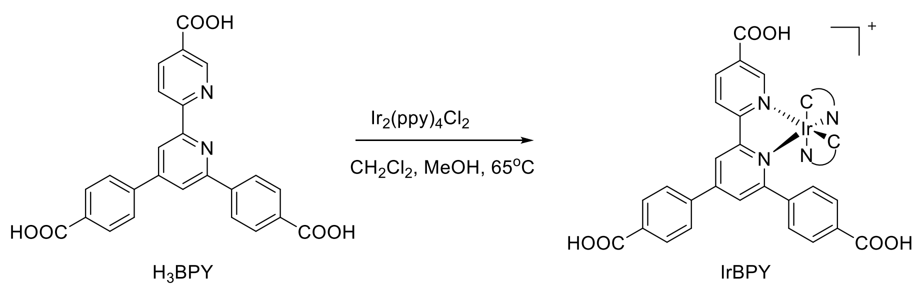

H_3BPY was synthesized according to the procedure in Chapter 2. H_3BPY (202 mg, 0.459 mmol) in CH_2Cl_2 (15 mL) was added to a stirred suspension of $Ir_2(ppy)_4Cl_2$ (246mg, 0.230 mmol) in MeOH (25 mL). The reaction mixture was heated at 68 ^oC with stirring overnight. After cooling to room temperature, the solvent was removed on a rotary evaporator. The residue was dissolved in MeOH and subjected to filtration. The filtrate was collected and concentrated. After adding a large amount of Et_2O, orange precipitate was collected by filtration, washed with Et_2O/MeOH and Et_2O, to afford Ir-BPY as orange solid (328 mg, 0.335 mmol, 73% yield). ^{1}H NMR (500 MHz, DMSO-d^6) δ 12.85 (br, 3H), 9.35 (d, 2H), 8.63 (d, 2H, J = 8.0 Hz), 8.35 (d, 2H, J = 8.5Hz), 8.25 (s, 1H), 8.15-8.11 (m, 5H), 8.05-8.01 (m, 2H), 7.94-7.86 (m, 3H), 7.72 (s, 1H, J = 7.5Hz), 7.35-

7.23 (m, 4H), 7.17 (t, 1H), 6.91 (t, 1H), 6.80 (t, 1H), 6.44 (t, 1H), 6.25 (t, 1H), 5.82 (d, 1H), 5.41 (d,1H). ESI-MS: m/z = 941.4.

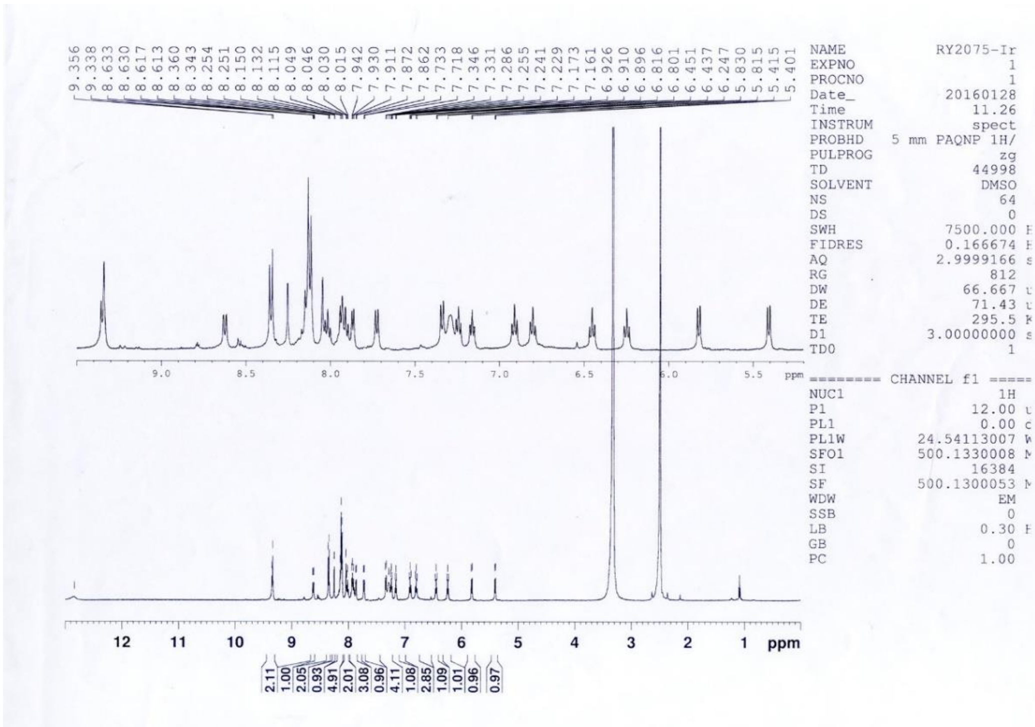

Figure 3-9. ^{1}H-NMR spectrum of IrBPY.

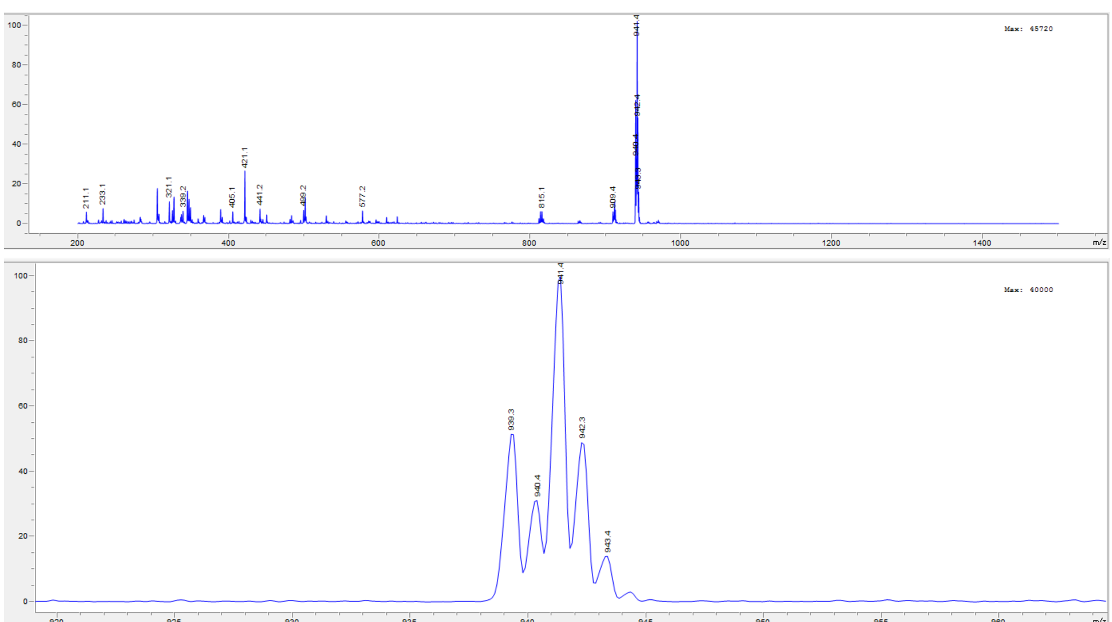

Figure 3-10. Mass spectrum of IrBPY.

Synthesis of BPY-MOL: H_3BPY (69 mg, 157 μmol) and $HfCl_4$ (84 mg, 262 μmol) were added to a solvent mixture of DMF (30 mL), HCOOH (3.0 mL, 79 mmol) and H_2O (4.5 mL, 250 mmol). The reaction mixture was kept in a 120 ^{o}C oven for 1 day. The white powder was collected by centrifugation and washed with DMF three times to afford BPY-MOL.

Synthesis of IrBPY-MOL: The as-prepared BPY-MOL was mixed with $Ir_2(ppy)_4Cl_2$ (100 mg, 92 μmol) and then added to a solution of DMF and MeOH (30 mL, v/v = 1:1). The resulting suspension was kept in a 70 ^{o}C oven for 2 days. Color change from pale yellow to orange indicates the formation of IrBPY-MOL. The product was collected by centrifugation and washed with DMF three times to afford IrBPY-MOL.

Synthesis of IrUiO-69: H_2L (33.9 mg, 43 μmol) and $HfCl_4$ (11.91 mg, 43 μmol) were dissolved in 2.17 mL DMF and 43.5 μL trifluoroacetic acid. The mixture was kept in a 100 ^{o}C oven for 4 days. The orange product was collected by centrifugation and washed with DMF for three times.

Polymerization Setup: Photopolymerization was performed under the irradiation of a 410nm blue LED. Light intensity was adjusted by the distance between the reaction vessel and the light source and determined by an optical power meter. The reaction setup was shown in **Figure 3-12**.

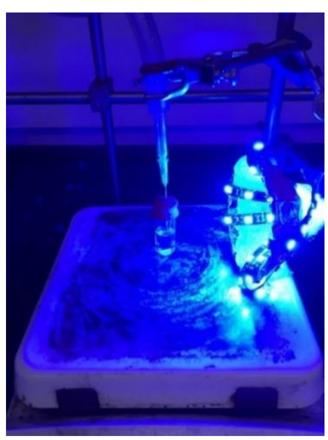

Figure 3-11. Polymerization setup.

General Procedures of MMA Living Polymerization

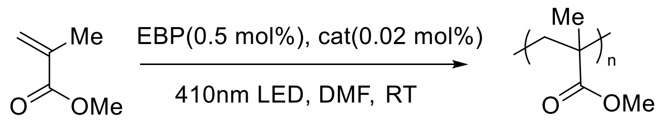

IrBPY-MOL (0.94 μmol) and a small stir bar was loaded into a 4-mL glass vial and added with MMA (500 μL, 4.71 mmol) and DMF (1.75 mL). The solution was degassed with nitrogen for 10 min, followed by addition of ethyl α-bromophenylacetate (4.12 μL, 23.5 μmol). The vial was then sealed with a rubber septum and further degassed by freeze-pump-thaw three times using a Schlenk line system. The reaction mixture was stirred in front of 410 nm LED for two days. The light intensity at the reaction vessel was 5 mW/cm^2. Then the reaction was allowed to stand in dark for 1 h. The conversion percentage was determined by ^{1}HNMR. The catalyst was isolated by centrifugation and washed with DMF several times. The supernatant was poured into a mixture of methanol and water (10:1, 50 mL) with vigorous stirring. The white precipitate formed was collected by centrifugation, taken up in a minimal amount of DMF, and crushed out again with a mixture of methanol and water (10:1, 50 mL). The white precipitate was then collected again and dried to give poly(MMA) and subjected to GPC analysis. The polymerization experiments with IrBPY and IrUiO-69 were carried out following the same protocol. ^{1}H NMR of polyMMA (500 MHz, CDCl3), δ: 3.57 (s, 3H), 1.96 – 1.72 (m, 1.8H), 1.40 (m, 0.16H), 1.16 (m, 0.18H), 1.00 (s, 1H), 0.82 (bs, 2H).

General Procedures of BMA Living Polymerization

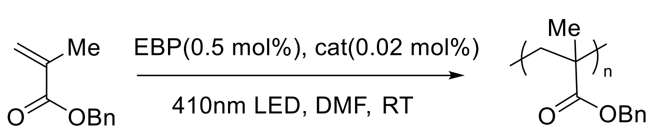

IrBPY-MOL (0.59 μmol) and a small stir bar were loaded into a 4-mL glass vial and added with BMA (500 μL, 2.95 mmol) and DMF (1.75 mL). The solution was degassed with nitrogen for 10 min, followed by addition of ethyl α-bromophenylacetate (2.59 μL, 14.8 μmol). The vial was then sealed with a rubber septum and further degassed by freeze-pump-thaw three times using a Schlenk line system. The reaction mixture was stirred in front of 410 nm LED for two days. The light intensity at the reaction vessel was 5 mW/cm^{-2}. Then the reaction was allowed to stand in dark for 1 h. The conversion percentage was determined by ^{1}HNMR. The catalyst was isolated by centrifugation and washed with DMF several times. The supernatant was poured into a mixture of methanol and water (10:1, 50 mL) with vigorous stirring. The white precipitate formed was collected by centrifugation, taken up in a minimal amount of DMF, and crushed out again with a mixture of methanol and water (10:1, 50 mL). The white precipitate was then collected again and dried to give poly(BMA) and subjected to GPC analysis. The polymerization experiments with IrBPY and IrUiO-69 were carried out following the same protocol. ^{1}H NMR of polyBMA (500 MHz, CDCl3), δ = 4.88 (m, 2H), 1.78 (m, 2.42 H), 1.25 (m, 0.48 H), 0.92 (bs, 1 H), 0.74 (bs, 2H).

General Procedures of *t*BuMA Living Polymerization

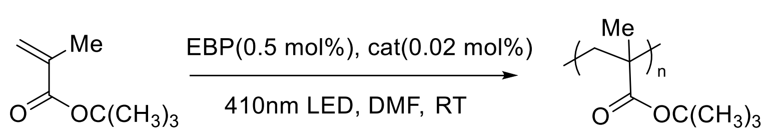

IrBPY-MOL (0.62 μmol) and a small stir bar were loaded into a 4-mL glass vial and added with *t*BuMA (500 μL, 3.08 mmol) and DMF (1.75 mL). The solution was degassed with nitrogen for 10 min, followed by addition of ethyl α-bromophenylacetate (2.70 μL, 15.4 μmol). The vial was then sealed with a rubber septum and further degassed by freeze-pump-thaw three times using a Schlenk line system. The reaction mixture was stirred in front of 410 nm LED for two days. The light intensity at the reaction vessel was 5 mW/cm^{-2}. Then the reaction was allowed to stand in dark for 1 h. The conversion percentage was determined by ^{1}H NMR. The catalyst was isolated by centrifugation and washed with DMF several times. The supernatant was poured into a mixture of methanol and water (10:1, 50 mL) with vigorous stirring. The white precipitate formed was collected by centrifugation, taken up in a minimal amount of DMF, and crushed out again with a mixture of methanol and water (10:1, 50 mL). The white precipitate was then collected again and dried to give poly(*t*BuMA) and subjected to GPC analysis. The polymerization experiments with IrBPY and IrUiO-69 were carried out following the same protocol. ^{1}H NMR of poly(*t*BuMA) (500 MHz, CDCl3), δ 2.1–1.8 (dd, 2H), 1.4 (s, 9H), 1.1–1.0 (d, 3H).

General Procedures of MMA Polymerization in the absence of EBP

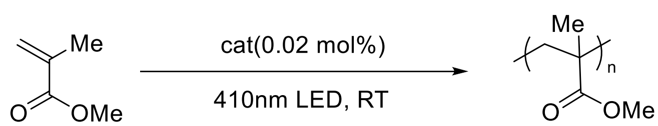

IrBPY-MOL (0.94 μmol) and a small stir bar were loaded into a 4-mL glass vial and added with MMA (500 μL, 4.71 mmol) and DMF (500 μL). The vial was sealed with a rubber septum and degassed by freeze-pump-thaw three times using a Schlenk line system. The reaction mixture was stirred in front of 410 nm LED for two days. The light intensity at the reaction vessel was 2 mW/cm^{-2}. Then the reaction was allowed to stand in dark for 1 h. The conversion percentage was determined by ^{1}H NMR. A small amount of DMF was added to the reaction solution to reduce viscosity if the solution was too viscous. The catalyst was isolated by centrifugation and washed with DMF several times. The supernatant was poured into 100 mL methanol with vigorous stirring. The white precipitate formed was collected by centrifugation, taken up in a minimal amount of DMF, and crushed out again with methanol. The white precipitate was then collected again and dried to give poly(MMA) and subjected to GPC analysis. The polymerization experiments with IrBPY and IrUiO-69 were carried out following the same protocol. This procedure is also applied to other solvents (DMA, THF, dioxane, toluene, EtOH).

General Procedures of BMA Polymerization in the absence of EBP

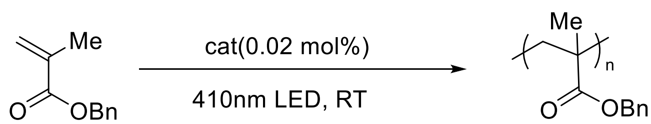

IrBPY-MOL (0.59 μmol) and a small stir bar were loaded into a 4-mL glass vial and added with BMA (500 μL, 2.95 mmol) and DMF (500 μL). The vial was sealed with a rubber septum and degassed by freeze-pump-thaw three times using a Schlenk line system. The reaction mixture was stirred in front of 410 nm LED for two days. The light intensity at the reaction vessel was 2 mW/cm^{-2}. Then the reaction was allowed to stand in dark for 1 h. The conversion percentage was determined by ^{1}HNMR. A small amount of DMF was added to the reaction solution to reduce viscosity if the solution was too viscous. The catalyst was isolated by centrifugation and washed with DMF several times. The supernatant was poured into 100 mL methanol with vigorous stirring. The white precipitate formed was collected by centrifugation, taken up in a minimal amount of DMF, and crushed out again with methanol. The white precipitate was then collected again and dried to give poly(BMA) and subjected to GPC analysis. The polymerization experiments with IrBPY and IrUiO-69 were carried out following the same protocol. This procedure is also applied to other solvents (DMA, THF, dioxane, toluene, EtOH).

3.5 References

(1) Ghobril, C.; Grinstaff, M. W. The chemistry and engineering of polymeric hydrogel adhesives for wound closure: a tutorial. *Chem. Soc. Rev.* **2015**, *44*, 1820-1835.

(2) Klotz, B. J.; Gawlitta, D.; Rosenberg, A. J. W. P.; Malda, J.; Melchels, F. P. W. Gelatin-Methacryloyl Hydrogels: Towards Biofabrication-Based Tissue Repair. *Trends Biotechnol.* **2016**, *34*, 394-407.

(3) Moszner, N.; Salz, U. Recent Developments of New Components for Dental Adhesives and Composites. *Macromol. Mater. Eng.* **2007**, *292*, 245-271.

(4) Samusjew, A.; Kratzer, M.; Moser, A.; Teichert, C.; Krawczyk, K. K.; Griesser, T. Inkjet Printing of Soft, Stretchable Optical Waveguides through the Photopolymerization of High-Profile Linear Patterns. *ACS Appl. Mater. Interfaces.* **2017**, *9*, 4941-4947.

(5) Klein, S.; Barsella, A.; Leblond, H.; Bulou, H.; Fort, A.; Andraud, C.; Lemercier, G.; Mulatier, J. C.; Dorkenoo, K. One-step waveguide and optical circuit writing in photopolymerizable materials processed by two-photon absorption. *Appl. Phys. Lett.* **2005**, *86*, 211118.

(6) Tsujii, Y.; Ohno, K.; Yamamoto, S.; Goto, A.; Fukuda, T. In *Surface-Initiated Polymerization I*; Jordan, R., Ed.; Springer Berlin Heidelberg: Berlin, Heidelberg, 2006, p 1-45.

(7) Gates, B. D.; Xu, Q.; Stewart, M.; Ryan, D.; Willson, C. G.; Whitesides, G. M. New Approaches to Nanofabrication: Molding, Printing, and Other Techniques. *Chem. Rev.* **2005**, *105*, 1171-1196.

(8) Guo, L. J. Nanoimprint Lithography: Methods and Material Requirements. *Adv. Mater.* **2007**, *19*, 495-513.

(9) de Gans, B. J.; Duineveld, P. C.; Schubert, U. S. Inkjet Printing of Polymers: State of the Art and Future Developments. *Adv. Mater.* **2004**, *16*, 203-213.

(10) Crivello, J. V.; Reichmanis, E. Photopolymer Materials and Processes for Advanced Technologies. *Chem. Mater.* **2014**, *26*, 533-548.

(11) Cumpston, B. H.; Ananthavel, S. P.; Barlow, S.; Dyer, D. L.; Ehrlich, J. E.; Erskine, L. L.; Heikal, A. A.; Kuebler, S. M.; Lee, I. Y. S.; McCord-Maughon, D.; Qin, J.; Rockel, H.; Rumi, M.; Wu, X.-L.; Marder, S. R.; Perry, J. W. Two-photon polymerization initiators for three-dimensional optical data storage and microfabrication. *Nature.* **1999**, *398*, 51-54.

(12) Xing, J.-F.; Zheng, M.-L.; Duan, X.-M. Two-photon polymerization microfabrication of hydrogels: an advanced 3D printing technology for tissue engineering and drug delivery. *Chem. Soc. Rev.* **2015**, *44*, 5031-5039.

(13) Voll, D.; Barner-Kowollik, C. Photoinitiators for Polymer Synthesis. Scope, Reactivity, and Efficiency. By Jean-Pierre Fouassier and Jacques Lalavée. *Angew. Chem. Int. Ed.* **2013**, *52*, 3312-3312.

(14) Xiao, P.; Zhang, J.; Dumur, F.; Tehfe, M. A.; Morlet-Savary, F.; Graff, B.; Gigmes, D.; Fouassier, J. P.; Lalevée, J. Visible light sensitive photoinitiating systems: Recent progress in cationic and radical photopolymerization reactions under soft conditions. *Prog. Polym. Sci.* **2015**, *41*, 32-66.

(15) Vana, P.; Barner-Kowollik, C.; Davis Thomas, P.; Matyjaszewski, K. Radical Polymerization. *Encyclopedia of Polymer Science and Technology*. **2003**.

(16) Index. *Dyes and Chromophores in Polymer Science.* **2015**.

(17) Dadashi-Silab, S.; Doran, S.; Yagci, Y. Photoinduced Electron Transfer Reactions for Macromolecular Syntheses. *Chem. Rev.* **2016**, *116*, 10212-10275.

(18) Polymeric Photosensors. *Polymers and Light.* **2007**.

(19) Jakubiak, J.; Allonas, X.; Fouassier, J. P.; Sionkowska, A.; Andrzejewska, E.; Linden, L. Å.; Rabek, J. F. Camphorquinone–amines photoinitating systems for the initiation of free radical polymerization. *Polymer.* **2003**, *44*, 5219-5226.

(20) Akat, H.; Gacal, B.; Balta Demet, K.; Arsu, N.; Yagci, Y. Poly(ethylene glycol)-thioxanthone prepared by Diels–Alder click chemistry as one-component polymeric photoinitiator for aqueous free-radical polymerization. *J. Polym. Sci., Part A: Polym. Chem.* **2010**, *48*, 2109-2114.

(21) Courtecuisse, F.; Cerezo, J.; Croutxé-Barghorn, C.; Dietlin, C.; Allonas, X. Depth characterization by confocal raman microscopy of oxygen inhibition in free radical photopolymerization of acrylates: Contribution of the thiol chemistry. *J. Polym. Sci., Part A: Polym. Chem.* **2012**, *51*, 635-643.

(22) O'Brien Allison, K.; Cramer Neil, B.; Bowman Christopher, N. Oxygen inhibition in thiol–acrylate photopolymerizations. *J. Polym. Sci., Part A: Polym. Chem.* **2006**, *44*, 2007-2014.

(23) Erdur, S.; Yilmaz, G.; Goen Colak, D.; Cianga, I.; Yagci, Y. Poly(phenylenevinylene)s as Sensitizers for Visible Light Induced Cationic Polymerization. *Macromolecules.* **2014**, *47*, 7296-7302.

(24) Zhang, J.; Frigoli, M.; Dumur, F.; Xiao, P.; Ronchi, L.; Graff, B.; Morlet-Savary, F.; Fouassier, J. P.; Gigmes, D.; Lalevée, J. Design of Novel Photoinitiators for Radical and Cationic Photopolymerizations under Near UV and Visible LEDs (385, 395, and 405 nm). *Macromolecules.* **2014**, *47*, 2811-2819.

(25) Lalevee, J.; Blanchard, N.; Tehfe, M.-A.; Peter, M.; Morlet-Savary, F.; Gigmes, D.; Fouassier, J. P. Efficient dual radical/cationic photoinitiator under visible light: a new concept. *Polym. Chem.* **2011**, *2*, 1986-1991.

(26) Zhang, G.; Song, I. Y.; Ahn, K. H.; Park, T.; Choi, W. Free Radical Polymerization Initiated and Controlled by Visible Light Photocatalysis at Ambient Temperature. *Macromolecules.* **2011**, *44*, 7594-7599.

(27) Chen, Y.; Hu, Z.; Xu, D.; Yu, Y.; Tang, X.; Guo, H. Studies of Free Radical Polymerization Initiated by Visible Light Photoredox Catalysis. *Macromol. Chem. Phys.* **2015**, *216*, 1055-1060.

(28) Lalevée, J.; Tehfe, M.-A.; Dumur, F.; Gigmes, D.; Blanchard, N.; Morlet-Savary, F.; Fouassier, J. P. Iridium Photocatalysts in Free Radical Photopolymerization under Visible Lights. *ACS Macro Lett.* **2012**, *1*, 286-290.

(29) Timpe, H. J.; Kronfeld, K. P. Light-induced polymer and polymerization reactions XXXIII: direct photoinitiation of methyl methacrylate polymerization by excited states of ketones. *J. Photochem. Photobiol. A: Chemistry.* **1989**, *46*, 253-267.

(30) Sangermano, M.; Razza, N.; Crivello James, V. Cationic UV-Curing: Technology and Applications. *Macromol. Mater. Eng.* **2014**, *299*, 775-793.

(31) Tar, H.; Sevinc Esen, D.; Aydin, M.; Ley, C.; Arsu, N.; Allonas, X. Panchromatic Type II Photoinitiator for Free Radical Polymerization Based on Thioxanthone Derivative. *Macromolecules.* **2013**, *46*, 3266-3272.

(32) Dadashi-Silab, S.; Bildirir, H.; Dawson, R.; Thomas, A.; Yagci, Y. Microporous Thioxanthone Polymers as Heterogeneous Photoinitiators for Visible Light Induced Free Radical and Cationic Polymerizations. *Macromolecules.* **2014**, *47*, 4607-4614.

(33) Monroe, B. M.; Weed, G. C. Photoinitiators for free-radical-initiated photoimaging systems. *Chem. Rev.* **1993**, *93*, 435-448.

(34) Aguirre-Soto, A.; Lim, C.-H.; Hwang, A. T.; Musgrave, C. B.; Stansbury, J. W. Visible-Light Organic Photocatalysis for Latent Radical-Initiated Polymerization via 2e–/1H+ Transfers: Initiation with Parallels to Photosynthesis. *J. Am. Chem. Soc.* **2014**, *136*, 7418-7427.

(35) Shanmugam, S.; Xu, J.; Boyer, C. Utilizing the electron transfer mechanism of chlorophyll a under light for controlled radical polymerization. *Chem. Sci.* **2015**, *6*, 1341-1349.

(36) Pan, X.; Malhotra, N.; Simakova, A.; Wang, Z.; Konkolewicz, D.; Matyjaszewski, K. Photoinduced Atom Transfer Radical Polymerization with ppm-Level Cu Catalyst by Visible Light in Aqueous Media. *J. Am. Chem. Soc.* **2015**, *137*, 15430-15433.

(37) Fors Brett, P.; Hawker Craig, J. Control of a Living Radical Polymerization of Methacrylates by Light. *Angew. Chem. Int. Ed.* **2012**, *51*, 8850-8853.

(38) Strandwitz, N. C.; Khan, A.; Boettcher, S. W.; Mikhailovsky, A. A.; Hawker, C. J.; Nguyen, T.-Q.; Stucky, G. D. One- and Two-Photon Induced Polymerization of Methylmethacrylate Using Colloidal CdS Semiconductor Quantum Dots. *J. Am. Chem. Soc.* **2008**, *130*, 8280-8288.

(39) Dadashi-Silab, S.; Yar, Y.; Yagci Acar, H.; Yagci, Y. Magnetic iron oxide nanoparticles as long wavelength photoinitiators for free radical polymerization. *Polym. Chem.* **2015**, *6*, 1918-1922.

(40) Teegardin, K.; Day, J. I.; Chan, J.; Weaver, J. Advances in Photocatalysis: A Microreview of Visible Light Mediated Ruthenium and Iridium Catalyzed Organic Transformations. *Org. Process Res. Dev.* **2016**, *20*, 1156-1163.

(41) Koike, T.; Akita, M. Visible-light radical reaction designed by Ru- and Ir-based photoredox catalysis. *Inorg. Chem. Front.* **2014**, *1*, 562-576.

(42) Prier, C. K.; Rankic, D. A.; MacMillan, D. W. C. Visible Light Photoredox Catalysis with Transition Metal Complexes: Applications in Organic Synthesis. *Chem. Rev.* **2013**, *113*, 5322-5363.

(43) Corrigan, N.; Shanmugam, S.; Xu, J.; Boyer, C. Photocatalysis in organic and polymer synthesis. *Chem. Soc. Rev.* **2016**, *45*, 6165-6212.

(44) Treat, N. J.; Fors, B. P.; Kramer, J. W.; Christianson, M.; Chiu, C.-Y.; Read de Alaniz, J.; Hawker, C. J. Controlled Radical Polymerization of Acrylates Regulated by Visible Light. *ACS Macro Lett.* **2014**, *3*, 580-584.

(45) Poelma Justin, E.; Fors Brett, P.; Meyers Gregory, F.; Kramer John, W.; Hawker Craig, J. Fabrication of Complex Three-Dimensional Polymer Brush Nanostructures through Light-Mediated Living Radical Polymerization. *Angew. Chem. Int. Ed.* **2013**, *52*, 6844-6848.

(46) Ma, W.; Chen, D.; Liu, L.; Ma, Y.; Wang, L.; Zhao, C.; Yang, W. Visible light-induced thiol-ene reaction: A new strategy to prepare A,ω-dithiol and A,ω-divinyl telechelic polythiolether oligomers. *J. Polym. Sci., Part A: Polym. Chem.* **2015**, *54*, 740-749.

(47) Wang, C.; Xie, Z.; deKrafft, K. E.; Lin, W. Doping Metal–Organic Frameworks for Water Oxidation, Carbon Dioxide Reduction, and Organic Photocatalysis. *J. Am. Chem. Soc.* **2011**, *133*, 13445-13454.

(48) Wang, C.; deKrafft, K. E.; Lin, W. Pt Nanoparticles@Photoactive Metal–Organic Frameworks: Efficient Hydrogen Evolution via Synergistic Photoexcitation and Electron Injection. *J. Am. Chem. Soc.* **2012**, *134*, 7211-7214.

(49) Kong, X. J.; Lin, Z.; Zhang, Z. M.; Zhang, T.; Lin, W. Hierarchical Integration of Photosensitizing Metal–Organic Frameworks and Nickel-Containing Polyoxometalates for Efficient Visible-Light-Driven Hydrogen Evolution. *Angew. Chem. Int. Ed.* **2016**, *55*, 6411-6416.

(50) Cao, L.; Lin, Z.; Peng, F.; Wang, W.; Huang, R.; Wang, C.; Yan, J.; Liang, J.; Zhang, Z.; Zhang, T.; Long, L.; Sun, J.; Lin, W. Self-Supporting Metal–Organic Layers as Single-Site Solid Catalysts. *Angew. Chem. Int. Ed.* **2016**, *55*, 4962-4966.

(51) Kong, X.-J.; Lin, Z.; Zhang, Z.-M.; Zhang, T.; Lin, W. Hierarchical Integration of Photosensitizing Metal–Organic Frameworks and Nickel-Containing Polyoxometalates for Efficient Visible-Light-Driven Hydrogen Evolution. *Angew. Chem. Int. Ed.* **2016**, *55*, 6411-6416.

(52) Wu, S.-H.; Ling, J.-W.; Lai, S.-H.; Huang, M.-J.; Cheng, C. H.; Chen, I. C. Dynamics of the Excited States of [Ir(ppy)2bpy]+ with Triple Phosphorescence. *J. Phys. Chem. A.* **2010**, *114*, 10339-10344.

(53) Lowry, M. S.; Goldsmith, J. I.; Slinker, J. D.; Rohl, R.; Pascal, R. A.; Malliaras, G. G.; Bernhard, S. Single-Layer Electroluminescent Devices and Photoinduced Hydrogen Production from an Ionic Iridium(III) Complex. *Chem. Mater.* **2005**, *17*, 5712-5719.

(54) Kozak, C. M.; Mountford, P. In *Encyclopedia of Inorganic Chemistry*; John Wiley & Sons, Ltd: 2006.

(55) Wang, C.-C.; Zhang, Y.-Q.; Li, J.; Wang, P. Photocatalytic CO2 reduction in metal–organic frameworks: A mini review. *J. Mol. Struct.* **2015**, *1083*, 127-136.

(56) Nasalevich, M. A.; Hendon, C. H.; Santaclara, J. G.; Svane, K.; van der Linden, B.; Veber, S. L.; Fedin, M. V.; Houtepen, A. J.; van der Veen, M. A.; Kapteijn, F.; Walsh, A.; Gascon, J. Electronic origins of photocatalytic activity in d0 metal organic frameworks. *Sci. Rep.* **2016**, *6*, 23676.

(57) Fors, B. P.; Hawker, C. J. Control of a Living Radical Polymerization of Methacrylates by Light. *Angew. Chem. Int. Ed.* **2012**, *51*, 8850-8853.

CHAPTER 4. Metal-Organic Layer-Supported Chiral Bis(oxazolyl)pyridine-Copper Catalysts for Enantioselective Direct-Addition of Terminal Alkynes to Imines

4.1 Introduction

Enantioselectivity is one of the most important concept in synthetic chemistry. The 1975 Nobel Prize was awarded to J.W. Cornforth and V. Prelog for their research on the stereochemistry of enzyme-catalyzed reactions and organic molecules/reaction. Incorporation of the concept in catalytic process, namely enantioselective catalysis or asymmetric catalysis, has become a major research area in organic chemistry. Since the early works on asymmetric cyclopropanation and hydrogenation in by R. Noyori and W.S. Knowles 1960s and 1970s,[1-4] there has been significant developments on asymmetric catalysis over the past few decades. The scope of asymmetric catalysis has been significantly enlarged to encompass a wide range of reactions, including nucleophilic additions of organometallic reagents to aldehydes, ketones, imines and nitriles,[5-8] conjugate additions,[9-13] aldol reactions,[14-17] allylic alkylations,[18,19] Diels–Alder reactions,[19-21] 1.3-dipolar additions,[22-24] enyne cyclizations,[25,26] olefin-metathesis[27-31] and many others. In 2001, the Nobel Prize in Chemistry was honored to R. Noyori, W.S. Knowles, and K.B. Sharpless for their research on the use of chiral catalysts for highly enantioselective reactions. Nowadays, asymmetric catalysis has become one of the most attractive solutions for synthesizing enantiomerically enriched/pure compounds, providing important starting materials and feedstocks for exploratory synthesis in laboratories and industrial production of natural products, pharmaceuticals, and agricultural chemicals.[32-35]

Although numerous chiral ligands and chiral catalysts have been reported in past few decades, only a handful of them, rooted in a very few core structures, can be regarded as truly successful in demonstrating proficiency in various mechanistically unrelated reactions.[36] These catalysts, termed "privileged chiral catalyst" by Jacobsen,[37] originate in the same manner as some compound classes are active against a number of different biological targets in pharmaceutical research.[38] They are useful not only for the practical synthesis of enantiomerically pure compounds, but also in the sense of exploration and discovery of novel enantioselective methodology in organic synthesis. The essence of these privileged chiral catalysts is their specific scaffolds, which are listed in **Figure 4-1**.

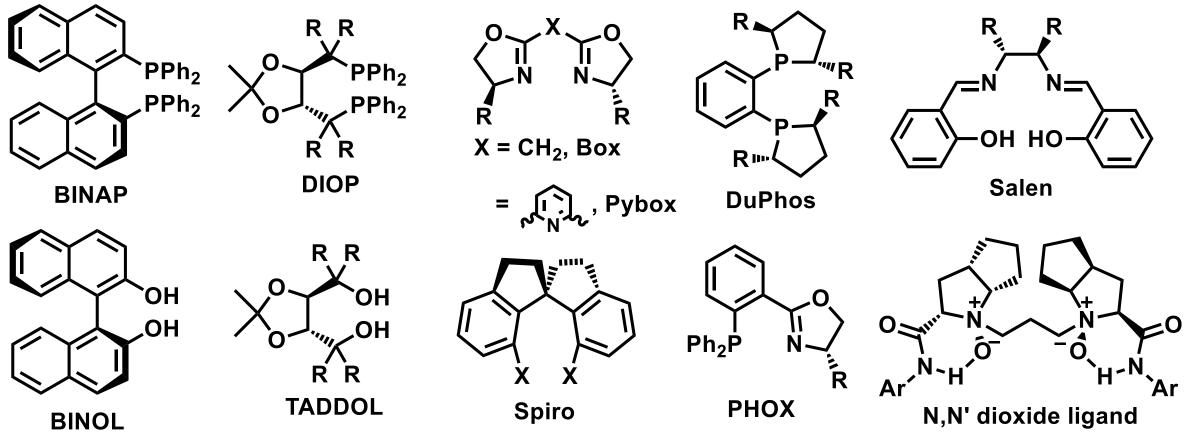

Figure 4-1. Examples of privileged ligands and catalysts.

Among these privileged ligands, bis(oxazoline) (Box) and pyridine-bis(oxazoline) (Pybox) are C_2-symmetric chiral ligands with two oxazoline rings separated by a spacer – a single carbon atom or a pyridine.[39,40] The discovery of bidentate Box dated back to 1991 when D.A. Evans reported asymmetric cyclopropanation of alkenes with Cu(I)-Box[41] and E.J. Corey reported asymmetric Diels-Alder reactions with Fe(III)-Box complexes.[42] Tridentate Pybox was reported by H. Nishiyama in 1989 when he used Rh-Pybox as catalyst for asymmetric hydrosilylation of ketones. All of these reactions showed good yields and high enantioselectivity (with e.e.'s exceeding 90%). Since these early reports, there have been many developments of Box- and Pybox in the field of asymmetric catalysis. In 2002, C.J. Li used Pybox –Cu(I) complex for the direct addition of terminal alkynes to imines (A^3 coupling reaction,[43-45] aldehyde-alkyne-amine) with good yields and high e.e.'s.[46] In this chapter, we used 2-D metal-organic layers to support bis(oxazolyl)pyridine-Cu(I) catalysts for enantioselective direct-addition of terminal alkynes to imines.

As single-site solid-state catalysts, MOFs have shown great potential in heterogeneous catalysis owing to their compositional tunability, high porosity, good thermal/chemical stability and well-defined reaction environments.[47-50] Moreover, MOFs can shut down intermolecular catalyst deactivation via site isolation or synergistically activate substrates by orienting multiple functional groups in specific orientations, affording turnover numbers (TONs) orders of magnitude higher than their homogeneous analogs.[51,52] MOFs are also useful for asymmetric catalysis by incorporating the aforementioned privileged ligands and their metal complexes to afford homochiral MOFs.[53-58] To date, this incorporation strategy for MOF-based asymmetric catalysts has been limited to BINOL, BINAP, Salen, and their related derivatives. The molecular geometry of these privileged ligands allows for the introduction of two or multiple nitrogen or carboxylic groups to form 2 or 4-connected ligands with appropriate symmetry.[52,56,59-62] It would be synthetically challenging or cumbersome to incorporate other privileged chiral ligands into MOF scaffolds. Additionally, due to limited pore size and restricted diffusion through relatively small MOF channels, alternative strategies are needed to prepare single-site solid asymmetric catalysts that can allow the facile incorporation of privileged chiral ligands.

Our group recently developed a method to achieve surface modification of MOLs with monocarboxylic acid.[63] Eight monocarboxylic acids with different chain length and hydrophobicity/hydrophilicity have replaced the original capping formate groups on Hf_6-SBUs under solvothermal conditions. Different from postsynthetic modifications of MOFs, there is no limitation on the size of the monocarboxylate functional groups due to the open space around 2D MOL. Moreover, the catalytic performance of MOF is usually limited by diffusion rates of large reagents within 3D frameworks,[64] which would be obviated in 2D MOLs. We explored the use of MOLs to support asymmetric catalysts in this chapter. We hypothesized that without pore size confinement and diffusion limitation, MOLs can act as a universal platform for incorporating diverse chiral ligands for asymmetric catalysis. We introduced a monocarboxylate group onto Pybox and then anchor it onto MOLs using the capping ligand exchange strategy (**Figure 4-2**) and investigated the application of this functionalized MOF in A^3 coupling reactions.

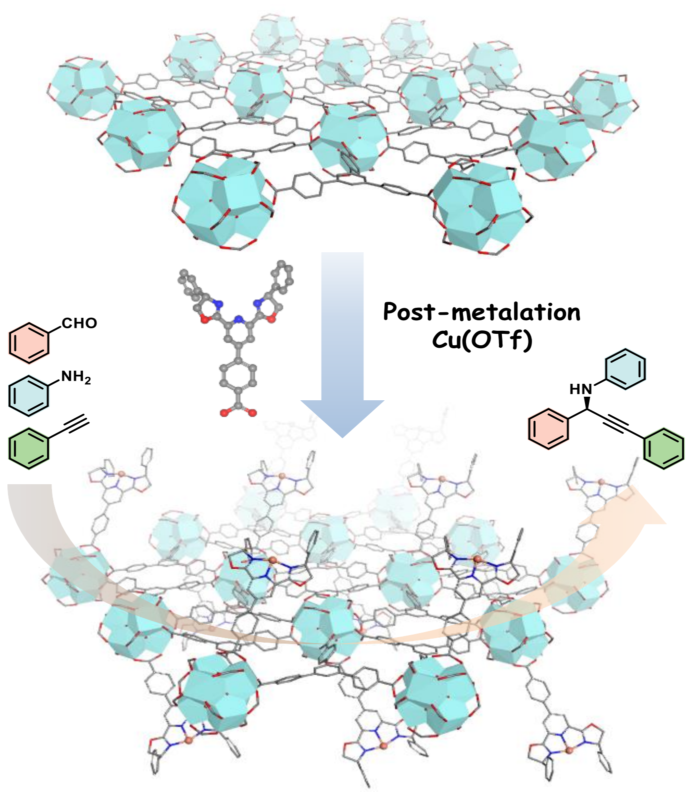

Figure 4-2. Synthesis of Pybox-MOL by replacing capping formate on $Zr_6(\mu_3\text{-}O)_4(\mu_3\text{-}OH)_4(HCO_2)_6$ SBUs with Pybox-CO_2H (**HL_1**). Only one Pybox was shown on each SBU as an illustration.

4.2 Results and Discussion

4.2.1 Synthesis of Pybox-CO_2H (HL_1)

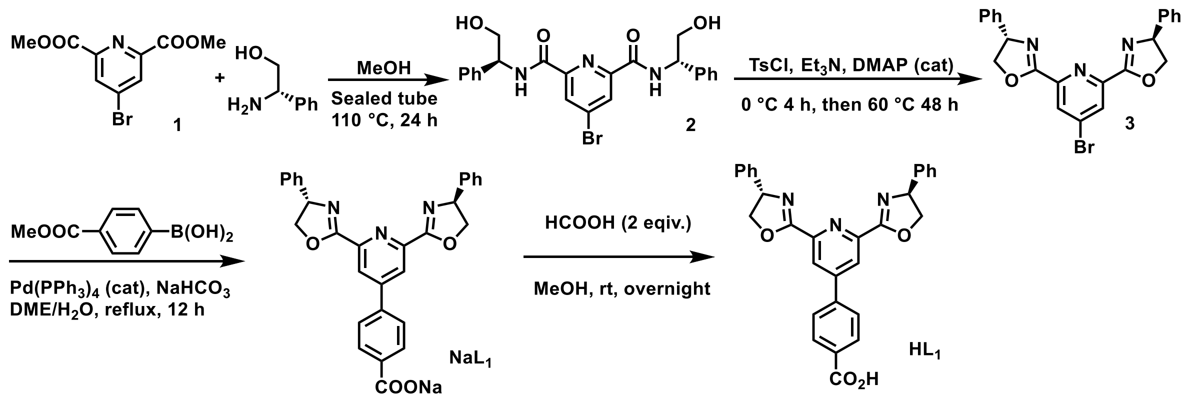

Scheme 4-1. Synthetic route of **HL_1**

We decided to study phenyl-substituted Pybox which showed highest enantioselectivity for A^3 coupling reactions in homogeneous systems.[46] The target ligand **HL_1** was synthesized according to **Scheme 4-1**. Pyridine-2,6-dicarboxylate **1** was reacted with enantiomerically pure (S)-(+)-2-phenylglycinol to give bis(amide) **2** in 83% yield. The ring-closure of hydroxyamide moiety took place under basic condition catalyzed by TsCl/DMAP, affording pyridine-bis(oxazoline) backbone **3**. Incorporation of carboxyl group was achieved by Suzuki coupling between the bromo-substituted Pybox **3** and 4-carboxylate phenyl boronic acid. It is interesting to note that even with very mild bases such as $NaHCO_3$ we observed the hydrolyzed compound **NaL_1** as the main product (87%), which did not occur in previous synthesis of similar ligands.[65-67] We attribute this difference to the electron-deficiency of oxazoline rings in **L_1** which makes ester more prone to a nucleophilic attack. **NaL_1** was insoluble in both the organic phase and the aqueous phase, and was readily separated from the reaction mixture by centrifugation. After careful acidification of **NaL_1** with formic acid, the targeted Pybox-CO_2H **HL_1** was obtained.

4.2.2 Synthesis and Characterization of Pybox-MOL

BTB-MOL was synthesized by mixing BTB and $ZrCl_4$ in a mixture of DMF, HCO_2H, and H_2O at 120 ˚C using a reported procedure.[68] As shown in **Figure 4-1**, the SBUs of the as-synthesized BTB-MOL were then modified by treatment with **HL$_1$** in DMF at 60 °C for 24 h to afford Pybox-MOL as a white solid. Efficient ligand exchange took place between **HL$_1$** and capping formate, proved by HNMR analysis of digested samples (**Figure 4-3**). The stoichiometric ratio of BPY:HCOOH:**HL$_1$** = 2 : 3.2 : 3.2, corresponding to the exchange of 50% formate to **HL$_1$**. Each SBU thus contains three Pybox on average, giving an empirical formula of $Zr_6(\mu_3\text{-}O)_4(\mu_3\text{-}OH)_4(HCO_2)_3(\mathbf{L_1})_3(BPY)_2$. This loading of Pybox on BTB-MOL is quite high. TEM and PXRD confirmed the retention of morphology and crystallinity of Pybox-MOL after the immobilization of **HL$_1$** using this method (**Figure 4-4**).

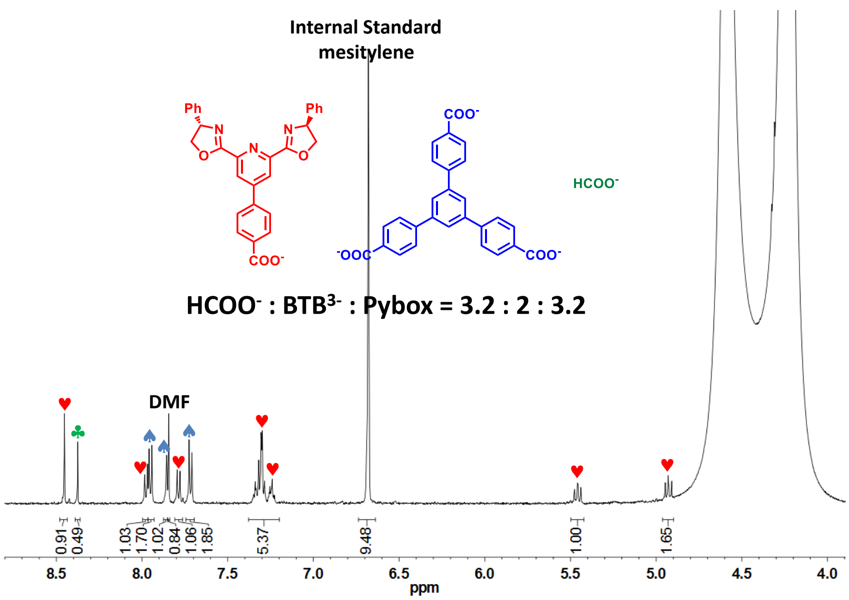

Figure 4-3. ^{1}H NMR spectrum of a digested Pybox-MOL sample (red heart: pybox; blue spade: BTB; green club: formate).

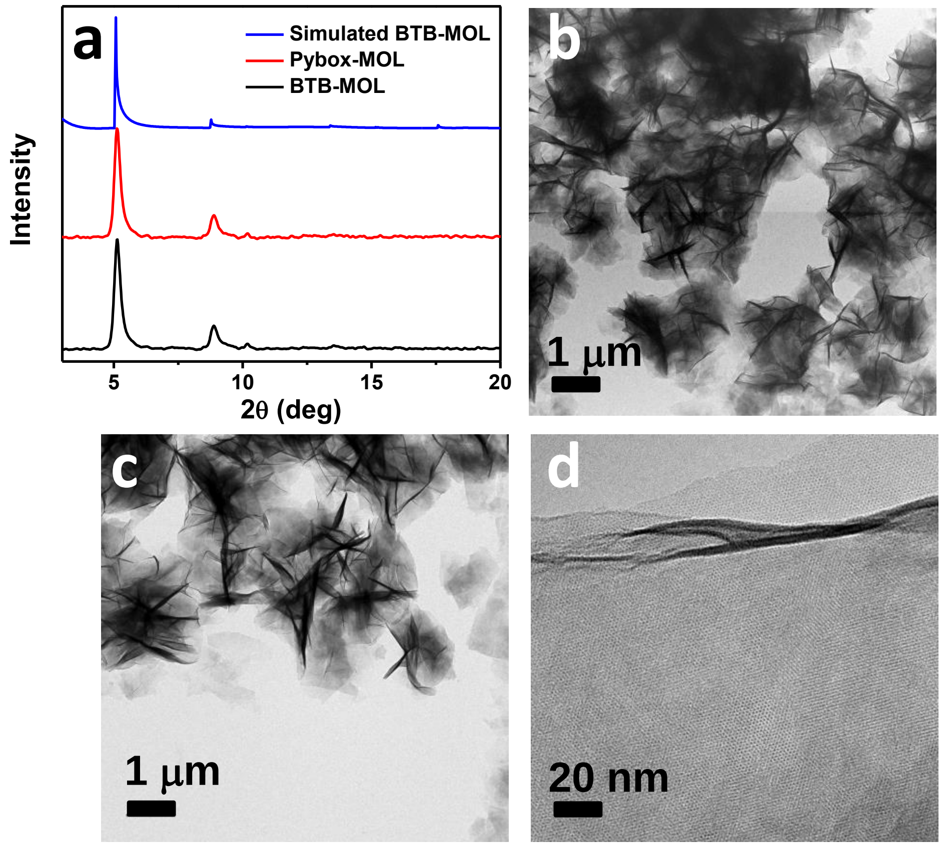

Figure 4-4. Structure and morphology of BTB-MOL and Pybox-MOL. (a) PXRD patterns of BTB-MOL, Pybox-MOL, and simulated BTB-MOL; (b) TEM image of BTB-MOL (scale bar: 1 μm); (c,d) TEM (c) and high resolution TEM (d) image of Pybox-MOL (scale bar: 1 μm).

We also synthesized PCN-128W as a MOF control.[69] PCN-128W is a large-pore MOF comprising 8-connected Zr_6 clusters and H_4ETTC (4′,4‴,4‴ ′ ′,4‴ ′ ‴-(ethene-1,1,2,2-tetrayl) tetrakis(([1,1′-biphenyl]-4-carboxylic acid)), ETTC) linkers (**Figure 4-5**). PCN-128W contains a large 1D hexagonal open channel with a diameter of 4.3 nm and a triangular channel with a diameter of 1.5 nm. PCN-128W also contains a dangling monocarboxylate ligand on the SBUs in a binding motif similar to MOLs. Each Zr_6-SBU is capped with two opposite trifluoacetate anions, which are present as modulators during hydrothermal synthesis process (**Figure 4-6a**).

Considering the strong acidity of trifluoacetic acid, the binding between trifluoacetate and Zr_6-SBUs should be weaker compared with formate in MOLs, which should facilitate the ligand exchange.

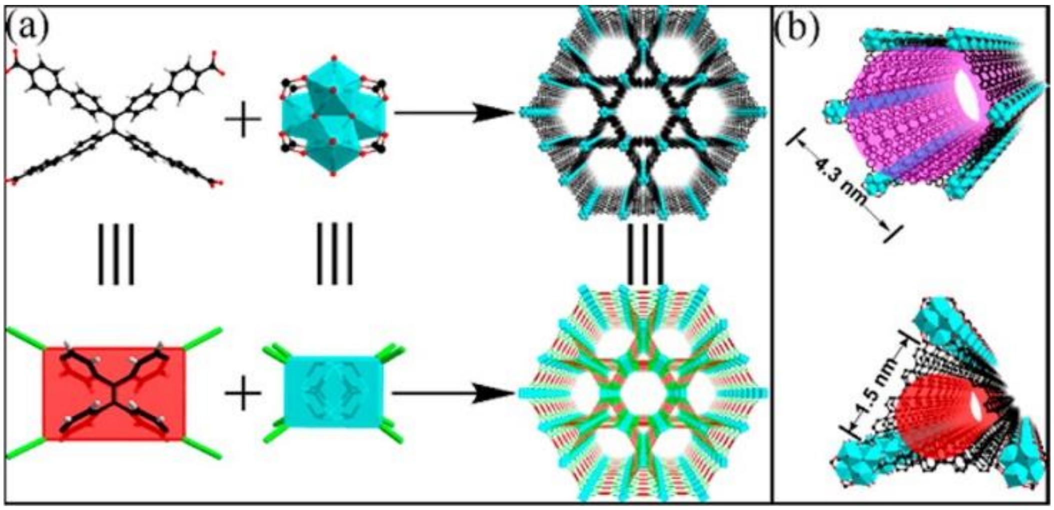

Figure 4-5. (a) Construction of PCN-128W from the ETTC linker and Zr_6 cluster. (b) Two types of 1D channels in PCN-128W, the hexagonal channel (purple pillar) and the triangular channel (red pillar). Reprinted with permission from *J. Am. Chem. Soc.*, **2015**, *137*, 10064–10067. Copyright 2017 American Chemical Society.

We synthesized PCN-128W under hydrothermal conditions using the reported method.[69] The obtained white solid showed good crystallinity by PXRD (**Figure 4-7**). PCN-128W was then treated with **HL$_1$** in DMF to afford Pybox-PCN-128W. After overnight reaction, 24% of trifluoroacetate was replaced by **HL$_1$**, indicated by ^{1}HNMR of digested samples (**Figure 4-8**). This number was significantly lower than that of Pybox-MOL. We attribute this to the limited pore size between the adjacent Zr_6 clusters (**Figure 4-6b**), which exclude the entry of **HL$_1$**. The measured Pybox-COOH after digestion may come from exchange of binding trifluoroacetates located in the large pores due to defects, or those on the MOF surfaces, or occupation of vacant SBU binding sites. This result also demonstrate MOL's geometric advantages in the ligand exchange process.

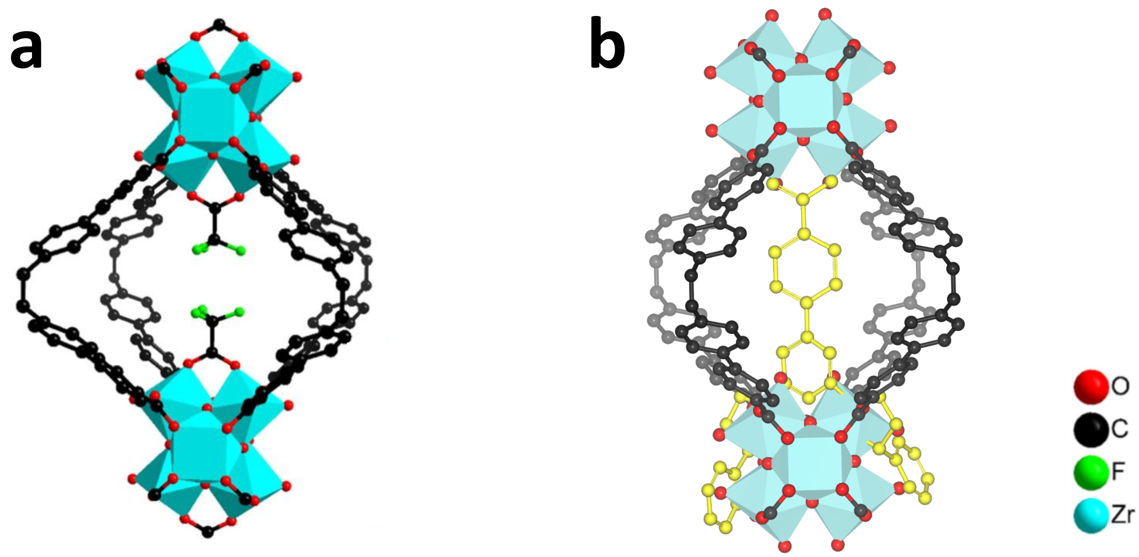

Figure 4-6. (a) Partial structure of PCN-128W showing the trifluoroacetate groups between the Zr_6 clusters. Reprinted with permission from *J. Am. Chem. Soc.*, **2015**, *137*, 10064–10067. Copyright 2017 American Chemical Society. (b) Fitting of Pybox-HOOC molecules (yellow) into the pores between Zr_6 clusters.

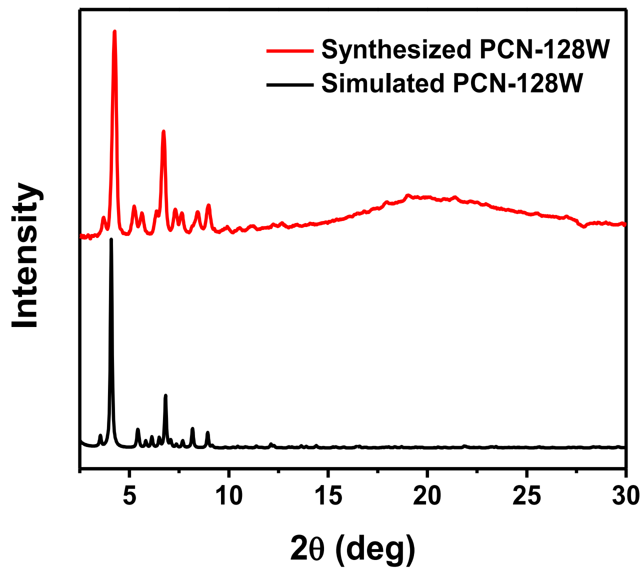

Figure 4-7. PXRD of PCN-128W (red: experimental, black: simulated).

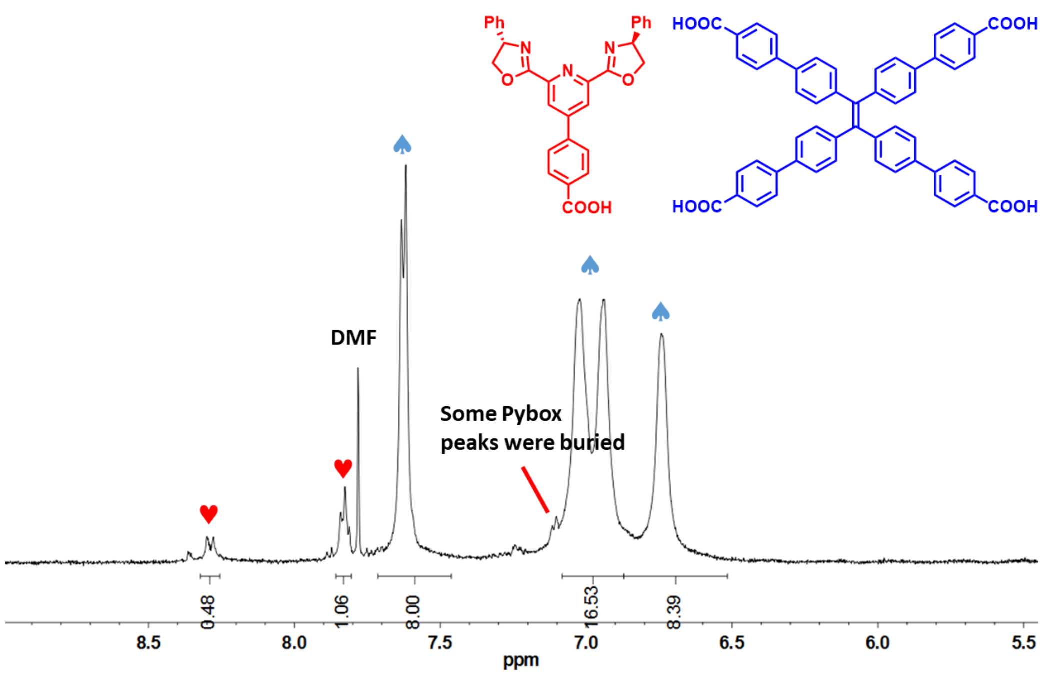

Figure 4-8. ^{1}HNMR of digested Pybox-PCN-128W. (red heart: Pybox; blue spade: ETTC).

4.2.3 Pybox-MOL Catalyzed A^3-coupling Reactions

The efficiency of pybox-MOL catalyst was demonstrated using the A^3-coupling reaction between aldehydes, alkynes, and amines. Cu(OTf) was added to the reaction mixture as catalyst, which can activate the terminal alkyne to Cu(I)-acetylide, followed by nucleophilic addition to imines.[70] In this system, Pybox provides chiral environment for the Cu(I) complex, which decides the stereoselectivity of the final adduct. We first studied the simplest case using non-substituted benzaldehyde, aniline and phenylacetylene; the addition product was formed in 76% yield with good e.e. of 79% after three days of reaction in toluene (**Table 4-1**, entry 1). When BTB-MOL was used instead of Pybox-MOL, the reaction can still proceeded with a lower efficiency (36%) and 0% ee (entry 2). This result is consistent with previous report that Cu(I) itself can catalyze addition between imines and terminal alkyne, [71,72], but the chiral environment provided by Pybox is needed for enantioselectivity. We further investigated the substrate scope for Pybox-MOL catalyzed A^3-coupling reactions (**Table 4-1**, entry 3-9). Pybox-Cu-MOL catalyzed A^3–coupling reactions of different aldehydes, anilines, and amines with good yield (73~85%) and moderate to high stereoselectivity (62-92% e.e.). For example, the reaction of 1.5 equiv. of phenylacetylene with N-(4-chlorobenzylidene)aniline formed in situ in toluene in the presence of 10 mol% Cu(I)-Pybox-MOL at 35 °C under nitrogen atmosphere afforded the target product in 82% yield and 92% ee. These experiments unambiguously demonstrate Pybox-MOL as an efficient asymmetric catalyst in this three-component reaction.

Table 4-1. Pybox-Cu-MOL catalyzed enantioselective direct-addition reactions of terminal alkynes to imines.[a]

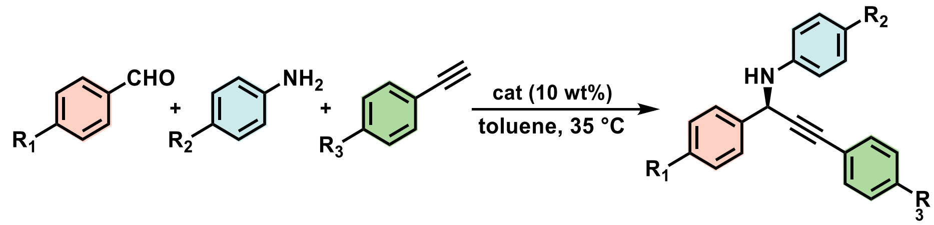

Entry	aldehyde	aniline	alkyne	Yield (%)[b]	ee (%)
1	PhCHO	$PhNH_2$	PhC≡CH	76	79
2[c]	PhCHO	$PhNH_2$	PhC≡CH	36	0
3	PhCHO	4-$ClPhNH_2$	PhC≡CH	82	92
4	PhCHO	4-$BrPhNH_2$	PhC≡CH	85	70
5	4-ClPhCHO	$PhNH_2$	PhC≡CH	81	91
6	4-BrPhCHO	$PhNH_2$	PhC≡CH	74	78
7	4-MeOPhCHO	$PhNH_2$	PhC≡CH	78	65
8	PhCHO	$PhNH_2$	4-MePhC≡CH	77	63
9	4-ClPhCHO	$PhNH_2$	4-MePhC≡CH	73	62

[a]Reaction conditions: 10 mol% pybox-MOL, 10% Cu(OTf), toluene (1 mL), aldehyde (0.2 mmol), aniline (0.24 mmol), alkyne (0.3 mmol), 35 °C, 3 days, under N_2 atmosphere. [b]Isolated yield of analytically pure product. [c]The reaction was run using BTB-MOL as catalyst instead of Pybox-MOL

4.3 Conclusion

In this chapter, we immobilized the enantiopure Pybox ligand onto the SBUs of MOLs through ligand exchange. This metal-organic layer-supported Cu(I) Pybox chiral catalyst exhibits good reactivity and enantioselectivity in asymmetric aldehyde-alkyne-amine (A^3) coupling reactions. Unlike well-studied homochiral MOF-based asymmetric catalysis, there are minimal structural requirements on the chiral catalysts for MOL-catalyzed asymmetric catalysis. Besides Salen and BINOL/BINAP ligands which have been extensively used to grow homochiral MOFs, many other privileged chiral catalysts do not have appropriate geometries to act as bridging ligands for MOF synthesis but can potentially be anchored to MOLs for heterogeneous asymmetric catalysis without constraint of pore size and diffusion limitations. Our result highlights MOLs as an effective platform to immobilize chiral catalysts for asymmetric organic reaction.

4.4 Methods and Experimental Details

4.4.1 General Methods

All starting materials were purchased from Aldrich and Fisher, unless otherwise noted. ^{1}H NMR spectra were recorded on a Bruker NMR 500 DRX spectrometer at 500 MHz and referenced to the proton resonance resulting from incomplete deuteration of the $CDCl_3$ (δ 7.26). ^{13}C NMR spectra were recorded at 125 MHz, and all of the chemical shifts were reported downfield in ppm relative to the carbon resonance of $CDCl_3$ (δ 77.10). TEM data were collected on a Tecnai Spirit (FEI, USA) electron microscope. Powder X-ray diffraction data were collected on a Bruker D8 Venture diffractometer using Cu Kα radiation source (λ = 1.54178 Å). Enantiomeric excess was determined with Shimadzu LC-20AT HPLC equipped with a Danical Chiralcel OD column and 5:95 hexane/ isopropanol as eluent.

Synthesis of BTB-MOL: H_3BTB (50 mg, 113 μmol) and $ZrCl_4$ (40.8 mg, 175 μmol) were mixed in DMF (8.2 mL). To this mixture was added HCOOH (3.5 mL) and H_2O (1.2 mL). The final mixture was dispersed by sonication and kept in a 120 ˚C oven for 24 h. The white precipitate was collected via centrifugation and washed with DMF three times, stored for ligand exchange.

Synthesis of Pybox-MOL: A mixture of BTB-MOLs (10 μmol by HCOOH) and **HL_1** (19.6 mg, 40 μmol) was dispersed in DMF (2 mL) in a glass vial with a small stir bar, kept at 60 ^{o}C and gently stirred overnight. The product was collected via centrifugation and washed with DMF three times.

Pybox-MOL digestion: Pybox–MOL (in DMF, ~5mg) was centrifuged and washed 3 times with MeOH, and then dried under vacuum to remove solvent residues. 100 μL K_3PO_4 (sat. in D_2O) was added. Then DMSO-d_6 was added in small potion and sonicated constantly (over 30 min) until the total volume reaches 500 μL. Next, 400 μL MeOD-d_4 was added and sonicated for another 30 min to help dissolving BTB ligands. 1 μL mesitylene was added as internal standard and the insoluble phosphate salt was removed by centrifugation before the final sample was analyzed by ^{1}HNMR.

Synthesis of PCN-128W: H_4ETTC was synthesized according to literature.[69] In a 4 mL Pyrex vial, $ZrCl_4$ (30.0 mg, 0.13 mmol) and H_4ETTC (15.0 mg, 0.018 mmol) were dissolved in 2 mL DMF and added with 0.2 mL trifluoroacetic acid. The mixture was heated at 120 °C for 2d. A white crystalline material was obtained and washed with DMF three times.

Synthesis of Pybox-PCN-128W: A mixture of PCN-MOLs (10 μmol by H_4ETTC) and **HL_1** (19.6 mg, 40 μmol) was dispersed in DMF (2 mL) and shaked with Dynabeads Sample Mixer overnight. Then it was collected via centrifugation and washed with DMF three times.

Pybox-PCN-128W digestion: Pybox-PCN-128W (in DMF, ~5mg) was centrifuged and washed with MeOH three times and then dried under vacuum to remove solvent residues. A CsF solution was then added (24 mg CsF in 450 μL DMSO/ 250 μL D_2O) and sonicated for 1 h. Zirconium phosphate was then removed by centrifugation before ^{1}H NMR analysis.

4.4.2 Synthesis of HL_1

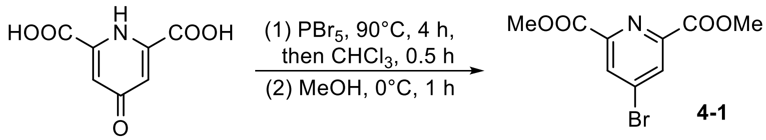

Synthesis of 4-1. In an ice bath, to a vigorously stirred solution of bromine (73.8 mmol, 3.83 mL) in petroleum ether (25 ml) was added PBr_3 (89.4 mmol, 8.5 mL) dropwise. After the mixture was stirred at room temperature for 2 h, PBr_5 was obtained in pure form by removing excess petroleum ether under reduced pressure. Then chelidamic acid (20 mmol, 3.66 g) was added and the resulting solid mixture was heated at 100 ºC for 4 h. The solid mixture melted when temperature was above 85 ºC. After cooling to room temperature, chloroform (50 mL) was added. The mixture was stirred for another 30 min and then filtered. The dark solution was cooled to 0 °C and MeOH (90 mL) was added dropwise. The solid precipitate was filtered off and recrystallized from MeOH to afford **1** as a white solid (4.56 g, 83%). ^{1}H NMR (400 MHz, $CDCl_3$): δ 8.46 (s, 2 H), 4.03 (s, 6 H).

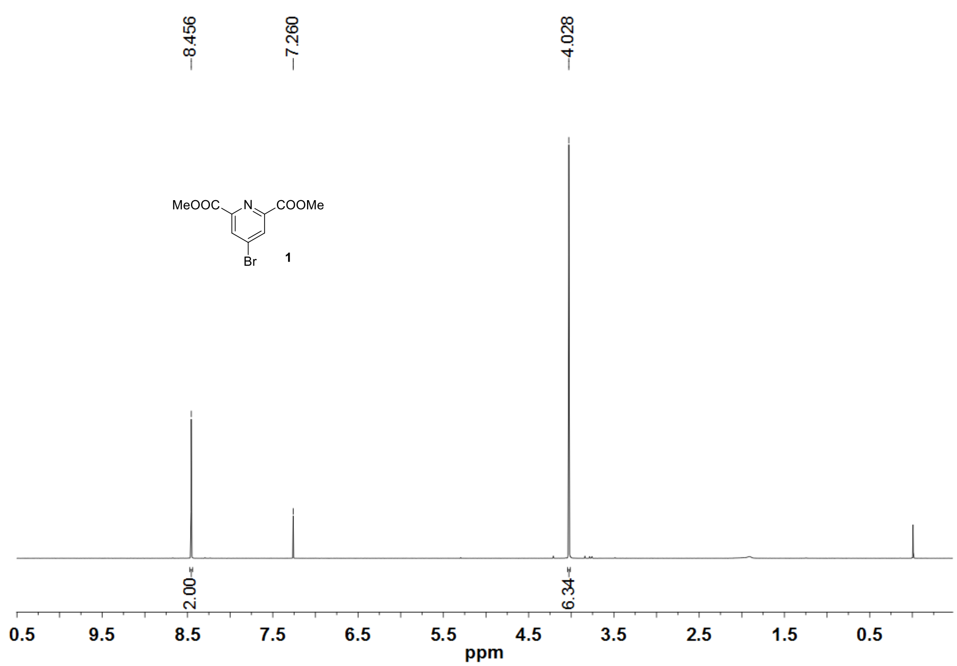

Figure 4-9. ^{1}H NMR spectrum of compound **4-1** (500 MHz) in $CDCl_3$ (10 mM).

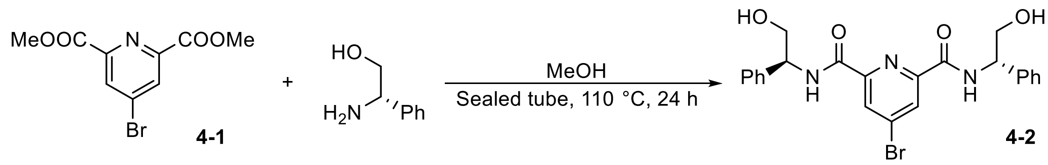

Synthesis of 4-2. A mixture of **4-1** (2.74 g, 10 mmol) and (*S*)-phenylglycinol (3.02 g, 22 mmol) was stirred at 110 °C for 24 h. After cooling to ambient temperature, the solvent was removed under reduced pressure. The crude solid was dissolved in a small amount of CH_2Cl_2 and subjected to column chromatography (SiO_2, CH_2Cl_2/MeOH, 100:1 to 40:1) to give the pure product **4-2** as a white solid (450 mg, 93%). ^{1}H NMR (500 MHz, $CDCl_3$): δ 8.55 (d, J = 7.5 Hz, 2 H), 8.45 (s, 2 H), 7.39–7.30 (m, 10 H), 5.23 (d t, J_1 = 7.5 Hz, J_2 = 5.0 Hz, 2 H), 3.99 (t, J = 5.0 Hz, 4 H), 2.70 (t, J = 6.0 Hz, 2 H).

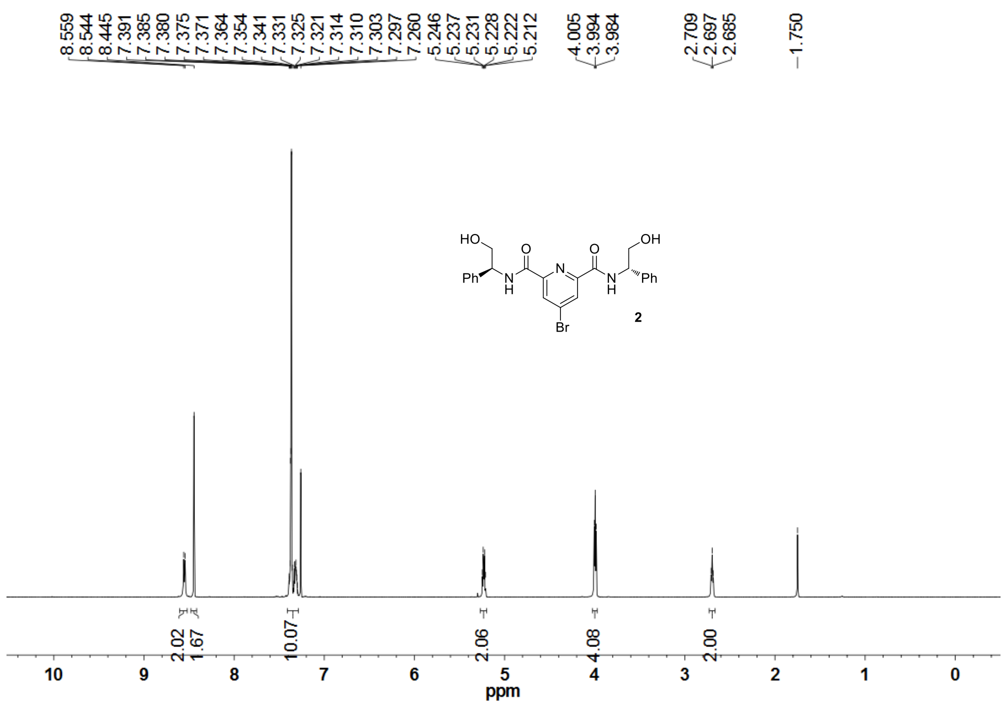

Figure. 4-10 ^{1}H NMR spectrum of compound **4-2** (500 MHz) in $CDCl_3$ (10 mM).

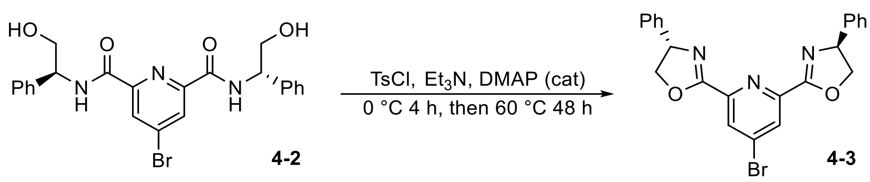

Synthesis of 3. A solution of **4-2** (1.079 g, 2.23 mmol), *p*-toluenesulfonyl chloride (TsCl, 1.058 g, 5.60 mmol), 4-Dimethylaminopyridine (DMAP, 24.2 mg, 0.2 mmol) and NEt_3 (2 mL) in CH_2Cl_2 (10 mL) was placed in a sealed tube. The solution was stirred at 0 °C for 4 h and then heated at 60 °C for 48 h. The mixture was diluted with CH_2Cl_2 (10 mL) and washed with 1 M NaOH (10 mL). The aqueous phase was extracted with CH_2Cl_2 (3 × 10 mL) and the combined organic solutions dried over anhydrous Na_2SO_4. After evaporation, the crude product was washed with ethanol to give **4-3** as a white solid (840 mg, 84%). ^{1}H NMR (500 MHz, $CDCl_3$): δ 8.53 (s, 2 H), 7.39–7.30 (m, 10 H), 5.46 (d d, J_1 = 10.5 Hz, J_2 = 9.0 Hz, 2 H), 4.94 (d d, J_1 = 10.5 Hz, J_2 = 9.0 Hz, 2 H), 4.44 (t, J = 9.0 Hz, 2 H).

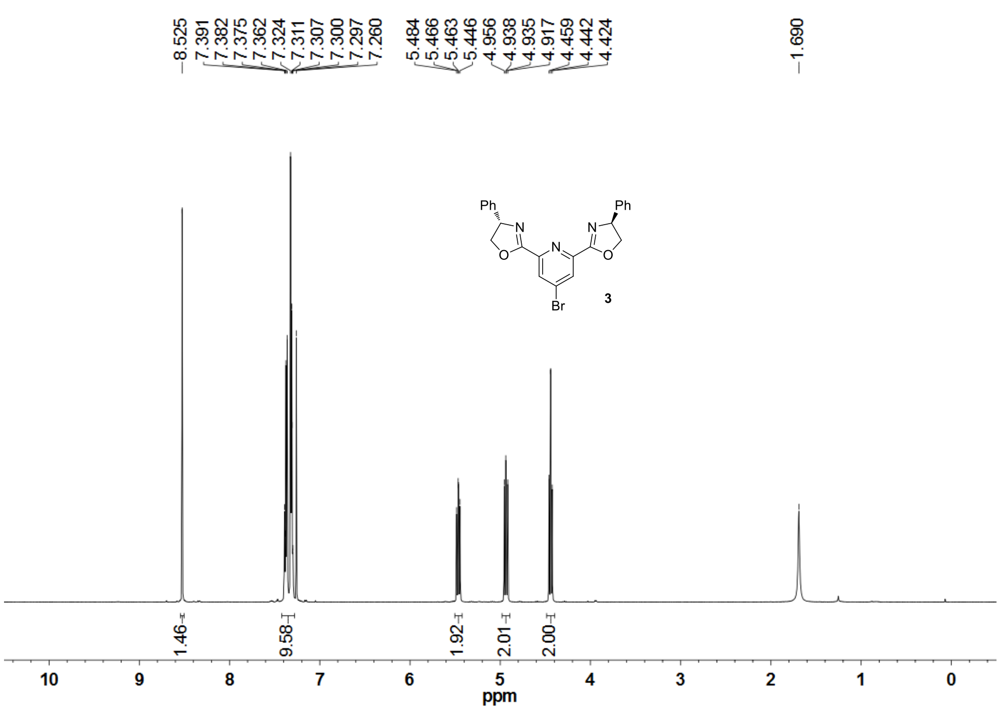

Figure 4-11. ^{1}H NMR spectrum of compound **4-3** (500 MHz) in $CDCl_3$ (10 mM).

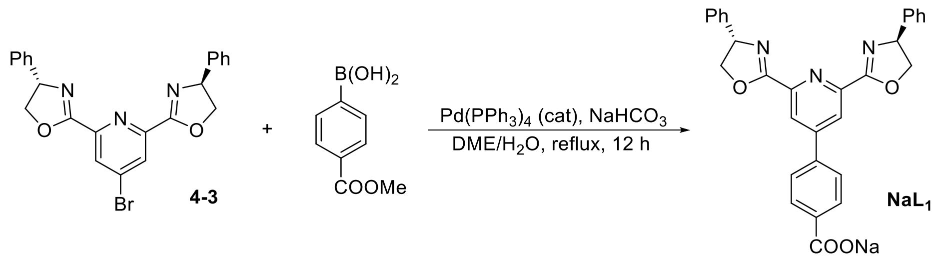

Synthesis of NaL_1. A solution of **4-3** (0.224 g, 0.5 mmol), 4-carboxyphenylboronic acid (0.099 g, 0.55 mmol), $Pd(PPh_3)_4$ (58 mg, 0.05 mmol) and $NaHCO_3$ (0.42 g, 5 mmol) in a mixed solvent of DME (10 mL) and H_2O (7.5 mL) was placed in a flask. After three freeze/pump/thaw cycles, the solution was stirred under reflux for 12 h. After cooling to ambient temperature, the solution was diluted with H_2O (20 mL) and CH_2Cl_2 (20 mL). The aqueous and organic phases can be well separated by adding a small amount of saturated brine. The precipitate was filtrated under reduced pressure and washed with H_2O and CH_2Cl_2 for several times. After drying under vacuum, the pure product was given as a white solid (0.222 g, 87%). ^1H NMR (500 MHz, CD_3OD): δ 8.54 (s, 2 H), 8.12 (d, J = 8.5 Hz, 2 H), 7.87 (d, J = 8.5 Hz, 2 H), 7.38–7.30 (m, 10 H), 5.52 (d d, J_1 = 10.5 Hz, J_2 = 8.5 Hz, 2 H), 5.02 (d d, J_1 = 10.5 Hz, J_2 = 8.5 Hz, 2 H), 4.42 (t, J = 8.5 Hz, 2 H). ^{13}C NMR (500 MHz, CD_3OD): δ 174.3, 165.0, 152.4, 147.6, 142.8, 141.1, 138.7, 131.4, 129.9, 128.9, 127.9, 127.7, 124.6, 77.3, 71.0.

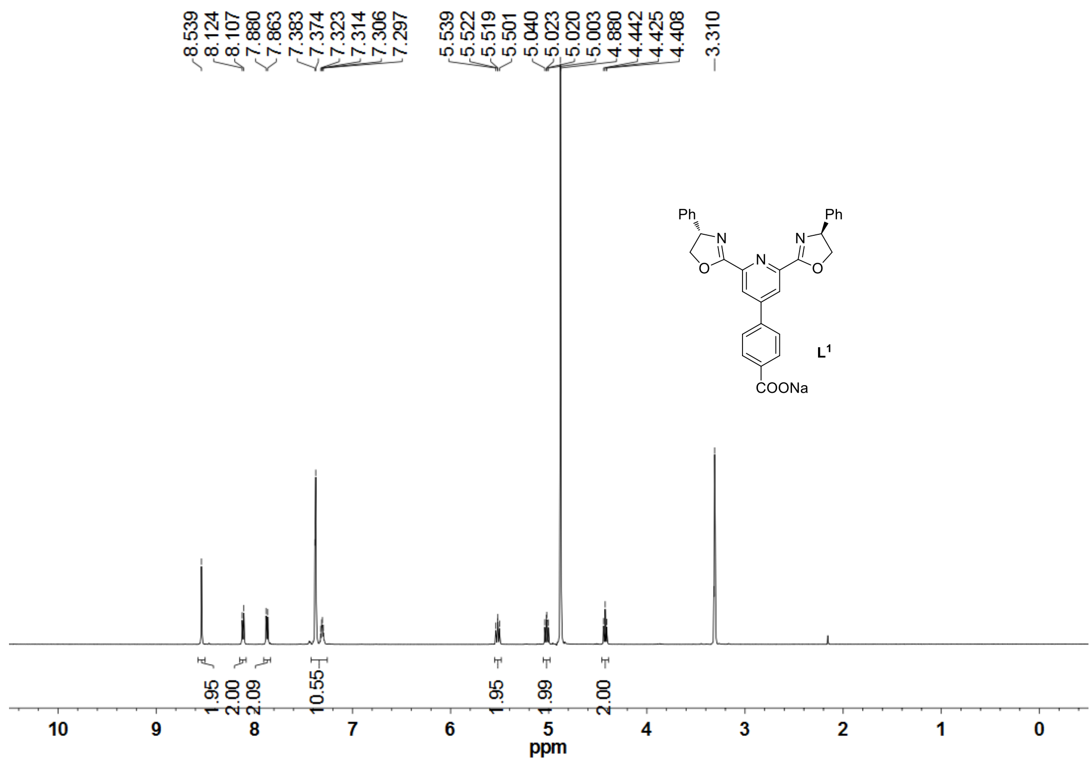

Figure 4-12. ^{1}H NMR spectrum of compound **NaL$_1$** (500 MHz) in CD_3OD (5 mM).

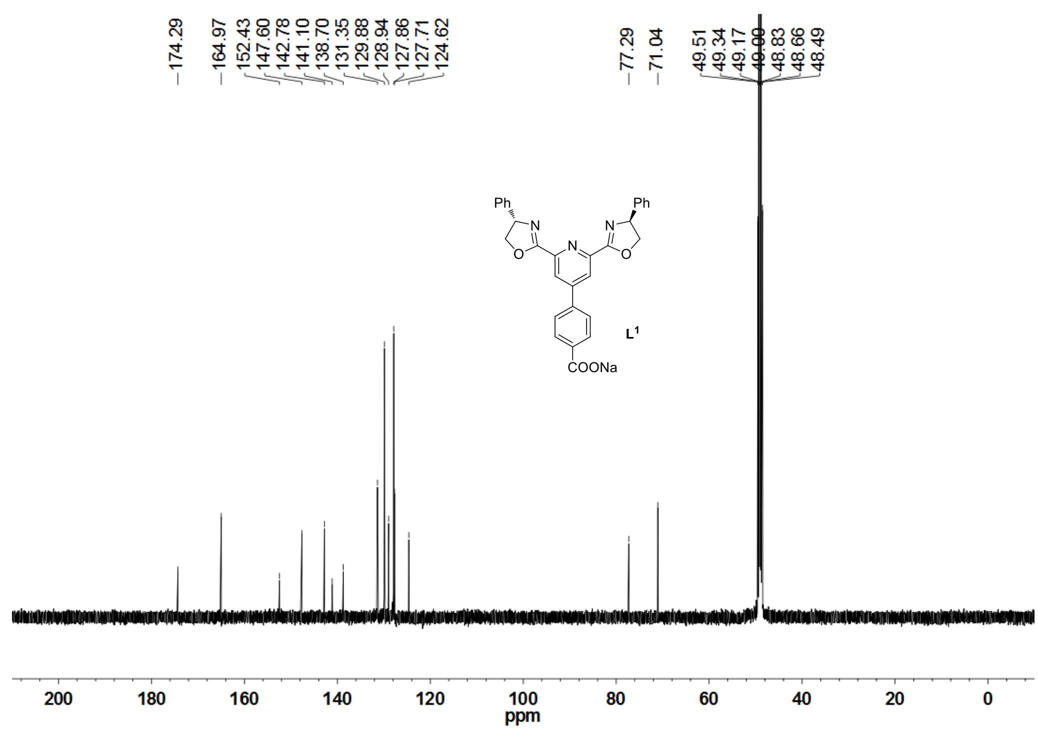

Figure 4-13. ^{13}C NMR spectrum of compound **NaL$_1$** (500 MHz) in CD_3OD (30 mM).

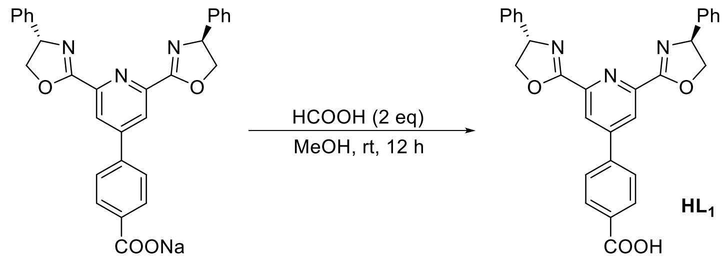

Synthesis of HL_1. NaL_1 (256 mg, 0.5 mmol) was dissolved in methanol (100 mL) and added HCOOH (18.5 μL, 1 mmol). The solution was sealed and undisturbed at room temperature for 12 hours. Colorless needle-like crystals were obtained, yield 232 mg, 95%. ^{1}H NMR (500 MHz, DMSO-d_6): δ 8.53 (s, 2 H), 8.09 (d, J = 8.5 Hz, 2 H), 8.05 (d, J = 8.5 Hz, 2 H), 7.43−7.28 (m, 10 H), 5.53 (d d, J_1 = 10 Hz, J_2 = 8.5 Hz, 2 H), 4.96 (d d, J_1 = 10 Hz, J_2 = 8.5 Hz, 2 H), 4.33 (t, J = 8.5 Hz, 1 H).

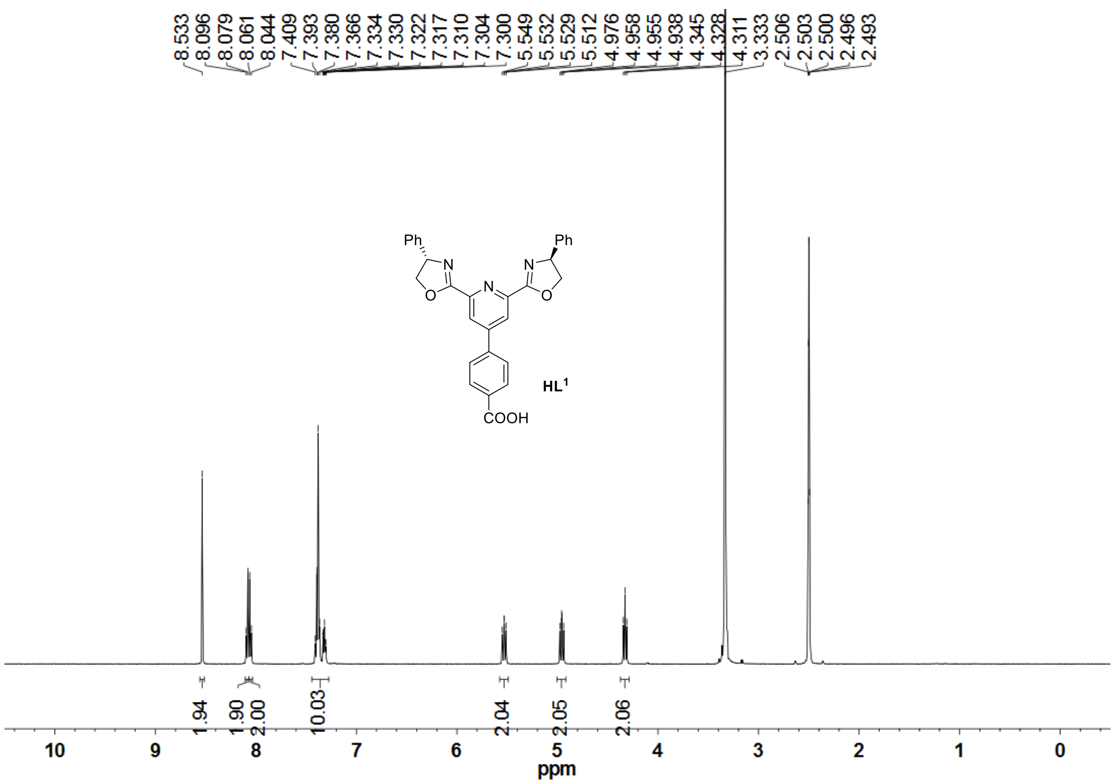

Figure. 4-14. ^{1}H NMR spectrum of compound **HL_1** (500 MHz) in CD_3OD (5 mM).

4.4.3 General Procedure for the Enantioselective Addition of Alkynes to Imines Catalyzed by Pybox-MOL-Cu(OTf) in Toluene.

A mixture of aldehyde (0.1 mmol) and aniline (0.12 mmol) was heated at 60 °C for 2 h. Pybox-MOL (0.01 mol based on pybox, 10 mol%) and Cu(I) triflate toluene complex (5 mg, 0.1 mmol, 10 mol%) were added, followed by alkyne (0.15 mmol) and toluene (0.5 mL) under an inert atmosphere of nitrogen. The mixture was stirred at 35 °C for 3 days. After removal of solvents, the residue was subjected to column chromatography (SiO_2, hexanes/CH_2Cl_2, 2: 1) to yield pure product as yellowish solid.

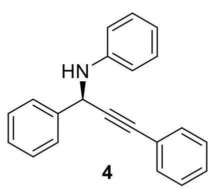

4

***(R)*-N-(1,3-diphenylprop-2-yn-1-yl)aniline (4**). HPLC (Daical Chiralcel OD, hexane/*i*-PrOH = 95:5, flow rate = 0.5 mL/min) t_R = 17.3 min, t_R = 21.0 min, ee = 79%. ^{1}H NMR ($CDCl_3$, 500 MHz): δ 7.67 (d, *J* = 7.5 Hz, 2 H), 7.43–7.40 (m, 4 H), 7.35 (t, *J* = 7.5 Hz, 1 H), 7.30–7.27 (m, 3 H), 7.22 (t, *J* = 7.5 Hz, 2 H), 6.81–6.78 (m, 3 H), 5.51 (d, *J* = 7.5 Hz, 1 H), 4.16 (d, *J* = 7.5 Hz, 1 H).

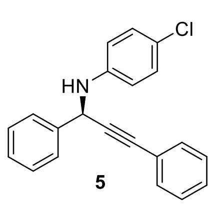

5

***(R)*-4-chloro-N-(1,3-diphenylprop-2-yn-1-yl)aniline (5).** HPLC (Daical Chiralcel OD, hexane/*i*-PrOH = 95:5, flow rate = 0.5 mL/min) t_R = 18.2 min, t_R = 21.3 min, ee = 92%. ^{1}H NMR ($CDCl_3$, 500 MHz): δ 7.65 (d, *J* = 7.5 Hz, 2 H), 7.44–7.41 (m, 4 H), 7.36 (t, *J* = 7.5 Hz, 1 H), 7.31–7.27

(m, 3 H), 7.16 (d, J = 8.5 Hz, 2 H), 6.71 (d, J = 8.5 Hz, 2 H), 5.46 (d, J = 7.5 Hz, 1 H), 4.17 (d, J = 7.5 Hz, 1 H).

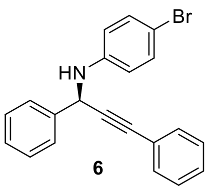

6

(*R*)-4-bromo-N-(1,3-diphenylprop-2-yn-1-yl)aniline (6). HPLC (Daical Chiralcel OD, hexane/*i*-PrOH = 95:5, flow rate = 0.5 mL/min) t_R = 20.5 min, t_R = 23.2 min, ee = 70%. ^{1}H NMR ($CDCl_3$, 500 MHz): δ 7.64 (d, J = 7.0 Hz, 2 H), 7.44–7.41 (m, 4 H), 7.36 (tt, J_1 = 7.5 Hz, J_2 = 2.0 Hz, 1 H), 7.32–7.28 (m, 5 H), 6.66 (dt, J_1 = 9.0 Hz, J_2 = 2.5 Hz, 2 H), 5.46 (d, J = 6.5 Hz, 1 H), 4.19 (d, J = 6.5 Hz, 1 H).

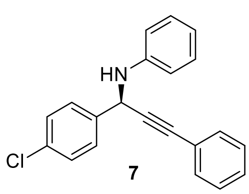

7

***(R)*-N-(1-(4-chlorophenyl)-3-phenylprop-2-yn-1-yl)aniline (7).** HPLC (Daical Chiralcel OD, hexane/*i*-PrOH = 95:5, flow rate = 0.5 mL/min) t_R = 27.7 min, t_R = 31.6 min, *ee* = 91%.^{1}H NMR ($CDCl_3$, 500 MHz): δ 7.60 (dt, J_1 = 8.5 Hz, J_2 = 2.5 Hz, 2 H), 7.42–7.40 (m, 2 H), 7.37 (dt, J_1 = 8.5 Hz, J_2 = 2.5 Hz, 2 H), 7.32–7.27 (m, 3 H), 7.21 (td, J_1 = 8.0 Hz, J_2 = 2.0 Hz, 2 H), 6.80 (t, J = 8.5 Hz, 2 H), 6.75 (d, J = 7.5 Hz, 2 H), 5.48 (d, J = 7.0 Hz, 1 H), 4.16 (d, J = 7.0 Hz, 1 H).

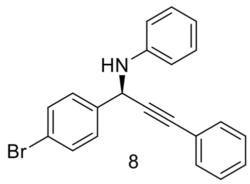

(***R***)**-N-(1-(4-bromophenyl)-3-phenylprop-2-yn-1-yl)aniline (8).** HPLC (Daical Chiralcel OD, hexane/*i*-PrOH = 95:5, flow rate = 0.5 mL/min) t_R = 26.6 min, t_R = 32.6 min, *ee* = 78%. ^{1}H NMR ($CDCl_3$, 500 MHz): δ 7.55–7.52 (m, 4 H), 7.42–7.40 (m, 2 H), 7.33–7.27 (m, 3 H), 7.24–7.20 (m, 2 H), 6.81 (t, *J* = 7.5 Hz, 1 H), 6.75 (d, *J* = 7.5 Hz, 2 H), 5.46 (br, 1 H), 4.17 (br, 1 H).

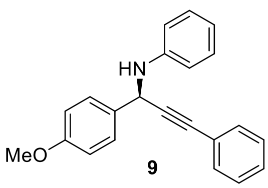

(***R***)**-N-(1-(4-methoxyphenyl)-3-phenylprop-2-yn-1-yl)aniline (9).** ^{1}H NMR ($CDCl_3$, 500 MHz): δ 7.68 (J_1 = 7.5 Hz, J_2 = 1.5 Hz, 1 H), 7.42–7.38 (m, 2 H), 7.32 (td, J_1 = 7.5 Hz, J_2 = 1.5 Hz, 1 H), 7.28–7.26 (m, 3 H), 7.22–7.18 (m, 2 H), 7.00 (td, J_1 = 7.5 Hz, J_2 = 1.0 Hz, 1 H), 6.95 (d, J = 8.0 Hz, 1 H), 6.80 (dd, J_1 = 8.0 Hz, J_2 = 1.0 Hz, 1 H), 6.76 (t, *J* = 7.5 Hz, 1 H), 5.80 (br, 1 H), 4.25 (br, 1 H), 3.90 (s, 3 H).

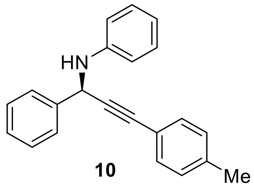

***(R)*-N-(1-phenyl-3-(*p*-tolyl)prop-2-yn-1-yl)aniline (10).** HPLC (Daical Chiralcel OD, hexane/*i*-PrOH = 95:5, flow rate = 0.5 mL/min) t_R = 15.3 min, t_R = 19.1 min, *ee* = 77%. ^{1}H NMR ($CDCl_3$, 500 MHz): δ 7.66 (d, *J* = 7.5 Hz, 2 H), 7.41 (t, *J* = 7.5 Hz, 2 H), 7.34 (t, *J* = 7.5 Hz, 1 H), 7.31 (d, *J* = 7.5 Hz, 2 H), 7.21 (t, *J* = 7.5 Hz, 2 H), 7.09 (d, *J* = 7.5 Hz, 2 H), 6.80–6.78 (m, 3 H), 5.50 (br, 1 H), 4.16 (br, 1 H), 2.34 (s, 3 H).

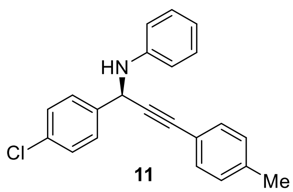

11

***(R)*-N-(1-(4-chlorophenyl)-3-(*p*-tolyl)prop-2-yn-1-yl)aniline (11).** HPLC (Daical Chiralcel OD, hexane/*i*-PrOH = 95:5, flow rate = 0.5 mL/min) t_R = 22.7 min, t_R = 28.0 min, *ee* = 64%. ^{1}H NMR ($CDCl_3$, 500 MHz): δ 7.59 (d, *J* = 8.5 Hz, 2 H), 7.37 (d, *J* = 8.5 Hz, 2 H), 7.30 (d, *J* = 8.0 Hz, 2 H), 7.21 (t, *J* = 7.5 Hz, 2 H), 7.10 (d, *J* = 8.0 Hz, 2 H), 6.80 (t, *J* = 7.5 Hz, 1 H), 6.74 (d, *J* = 7.5 Hz, 2 H), 5.46 (br, 1 H), 4.16 (br, 1 H), 2.34 (s, 3 H).

4.5 References

(1) Nozaki, H.; Moriuti, S.; Takaya, H.; Noyori, R. Asymmetric induction in carbenoid reaction by means of a dissymmetric copper chelate. *Tetrahedron Lett.* **1966**, *7*, 5239-5244.

(2) Nozaki, H.; Takaya, H.; Moriuti, S.; Noyori, R. Homogeneous catalysis in the decomposition of diazo compounds by copper chelates: Asymmetric carbenoid reactions. *Tetrahedron.* **1968**, *24*, 3655-3669.

(3) Knowles, W. S.; Sabacky, M. J. Catalytic asymmetric hydrogenation employing a soluble, optically active, rhodium complex. *Chem. Commun. (London).* **1968**, 1445-1446.

(4) Knowles, W. S.; Sabacky, M. J.; Vineyard, B. D. Catalytic asymmetric hydrogenation. *J. Chem. Soc., Chem. Commun.* **1972**, 10-11.

(5) Soai, K.; Niwa, S. Enantioselective addition of organozinc reagents to aldehydes. *Chem. Rev.* **1992**, *92*, 833-856.

(6) Noyori, R.; Kitamura, M. Enantioselective Addition of Organometallic Reagents to Carbonyl Compounds: Chirality Transfer, Multiplication, and Amplification. *Angew. Chem. Int. Ed.* **2003**, *30*, 49-69.

(7) Enders, D.; Reinhold, U. Asymmetric synthesis of amines by nucleophilic 1,2-addition of organometallic reagents to the CN-double bond. *Tetrahedron: Asymmetry.* **1997**, *8*, 1895-1946.

(8) Tirayut, V.; Worawan, B.; Yongsak, S.-A. Recent Advances in Catalytic Asymmetric Addition to Imines and Related C=N Systems. *Curr. Org. Chem.* **2005**, *9*, 1315-1392.

(9) Rossiter, B. E.; Swingle, N. M. Asymmetric conjugate addition. *Chem. Rev.* **1992**, *92*, 771-806.

(10) Hawner, C.; Alexakis, A. Metal-catalyzed asymmetric conjugate addition reaction: formation of quaternary stereocenters. *Chem. Commun.* **2010**, *46*, 7295-7306.

(11) Rueping, M.; Nachtsheim Boris , J.; Moreth Stefan , A.; Bolte, M. Asymmetric Brønsted Acid Catalysis: Enantioselective Nucleophilic Substitutions and 1,4-Additions. *Angew. Chem. Int. Ed.* **2007**, *47*, 593-596.

(12) Tsogoeva Svetlana, B. Recent Advances in Asymmetric Organocatalytic 1,4-Conjugate Additions. *Eur. J. Org. Chem.* **2007**, *2007*, 1701-1716.

(13) P. Sibi, M.; Manyem, S. Enantioselective Conjugate Additions. *Tetrahedron.* **2000**, *56*, 8033-8061.

(14) Evans, D. A.; Bartroli, J.; Shih, T. L. Enantioselective aldol condensations. 2. Erythro-selective chiral aldol condensations via boron enolates. *J. Am. Chem. Soc.* **1981**, *103*, 2127-2129.

(15) Saito, S.; Yamamoto, H. Design of Acid−Base Catalysis for the Asymmetric Direct Aldol Reaction. *Acc. Chem. Res.* **2004**, *37*, 570-579.

(16) Machajewski Timothy, D.; Wong, C. H. The Catalytic Asymmetric Aldol Reaction. *Angew. Chem. Int. Ed.* **2000**, *39*, 1352-1375.

(17) Northrup, A. B.; MacMillan, D. W. C. The First Direct and Enantioselective Cross-Aldol Reaction of Aldehydes. *J. Am. Chem. Soc.* **2002**, *124*, 6798-6799.

(18) Trost, B. M.; Van Vranken, D. L. Asymmetric transition metal-catalyzed allylic alkylations. *Chem. Rev.* **1996**, *96*, 395-422.

(19) Trost, B. M.; Crawley, M. L. Asymmetric transition-metal-catalyzed allylic alkylations: applications in total synthesis. *Chem. Rev.* **2003**, *103*, 2921-2944.

(20) Ahrendt, K. A.; Borths, C. J.; MacMillan, D. W. C. New strategies for organic catalysis: the first highly enantioselective organocatalytic diels− alder reaction. *J. Am. Chem. Soc.* **2000**, *122*, 4243-4244.

(21) Corey, E. J. Catalytic enantioselective Diels–Alder reactions: methods, mechanistic fundamentals, pathways, and applications. *Angew. Chem. Int. Ed.* **2002**, *41*, 1650-1667.

(22) Gothelf, K. V.; Jørgensen, K. A. Asymmetric 1,3-Dipolar Cycloaddition Reactions. *Chem. Rev.* **1998**, *98*, 863-910.

(23) Pellissier, H. Asymmetric 1,3-dipolar cycloadditions. *Tetrahedron.* **2007**, *63*, 3235-3285.

(24) Hashimoto, T.; Maruoka, K. Recent Advances of Catalytic Asymmetric 1,3-Dipolar Cycloadditions. *Chem. Rev.* **2015**, *115*, 5366-5412.

(25) Fairlamb Ian, J. S. Asymmetric Cycloisomerization of 1,6- and 1,7-Enynes by Transition-Metal Catalysts. *Angew. Chem. Int. Ed.* **2004**, *43*, 1048-1052.

(26) Muñoz, M. P.; Adrio, J.; Carretero, J. C.; Echavarren, A. M. Ligand effects in gold-and platinum-catalyzed cyclization of enynes: Chiral gold complexes for enantioselective alkoxycyclization. *Organometallics.* **2005**, *24*, 1293-1300.

(27) Scholl, M.; Ding, S.; Lee, C. W.; Grubbs, R. H. Synthesis and activity of a new generation of ruthenium-based olefin metathesis catalysts coordinated with 1, 3-dimesityl-4, 5-dihydroimidazol-2-ylidene ligands. *Org. Lett.* **1999**, *1*, 953-956.

(28) Van Veldhuizen, J. J.; Garber, S. B.; Kingsbury, J. S.; Hoveyda, A. H. A recyclable chiral Ru catalyst for enantioselective olefin metathesis. Efficient catalytic asymmetric ring-opening/cross metathesis in air. *J. Am. Chem. Soc.* **2002**, *124*, 4954-4955.

(29) Hoveyda, A. H.; Zhugralin, A. R. The remarkable metal-catalysed olefin metathesis reaction. *Nature.* **2007**, *450*, 243.

(30) Hoveyda, A. H.; Schrock, R. R. Catalytic asymmetric olefin metathesis. *Chem. Eur. J.* **2001**, *7*, 945-950.

(31) Fürstner, A. Olefin metathesis and beyond. *Angew. Chem. Int. Ed.* **2000**, *39*, 3012-3043.

(32) Yoon, T. P. Strategies in asymmetric catalysis. *Beilstein J. Org. Chem.* **2017**, *13*, 63-64.

(33) Goldfuß, B. *Enantioselective Catalysis, From Principles to Industrial Production*, 2019.

(34) Bolm, C.; Gladysz, J. A. Introduction: Enantioselective Catalysis. *Chem. Rev.* **2003**, *103*, 2761-2762.

(35) Halpern, J.; Trost, B. M. Asymmetric Catalysis. *Proc. Natl. Acad. Sci. U.S.A.* **2004**, *101*, 5347-5347.

(36) Zhou, Q.-L. *Privileged chiral ligands and catalysts*; John Wiley & Sons, 2011.

(37) Yoon, T. P.; Jacobsen, E. N. Privileged Chiral Catalysts. *Science.* **2003**, *299*, 1691.

(38) Evans, B. E.; Rittle, K. E.; Bock, M. G.; DiPardo, R. M.; Freidinger, R. M.; Whitter, W. L.; Lundell, G. F.; Veber, D. F.; Anderson, P. S.; Chang, R. S. L.; Lotti, V. J.; Cerino, D. J.; Chen, T. B.; Kling, P. J.; Kunkel, K. A.; Springer, J. P.; Hirshfield, J. Methods for drug discovery: development of potent, selective, orally effective cholecystokinin antagonists. *J. Med. Chem.* **1988**, *31*, 2235-2246.

(39) Desimoni, G.; Faita, G.; Jørgensen, K. A. C2-Symmetric Chiral Bis(Oxazoline) Ligands in Asymmetric Catalysis. *Chem. Rev.* **2006**, *106*, 3561-3651.

(40) Desimoni, G.; Faita, G.; Quadrelli, P. Pyridine-2,6-bis(oxazolines), Helpful Ligands for Asymmetric Catalysts. *Chem. Rev.* **2003**, *103*, 3119-3154.

(41) Evans, D. A.; Woerpel, K. A.; Hinman, M. M.; Faul, M. M. Bis(oxazolines) as chiral ligands in metal-catalyzed asymmetric reactions. Catalytic, asymmetric cyclopropanation of olefins. *J. Am. Chem. Soc.* **1991**, *113*, 726-728.

(42) Corey, E. J.; Imai, N.; Zhang, H. Y. Designed catalyst for enantioselective Diels-Alder addition from a C2-symmetric chiral bis(oxazoline)-iron(III) complex. *J. Am. Chem. Soc.* **1991**, *113*, 728-729.

(43) Sakaguchi, S.; Kubo, T.; Ishii, Y. A Three-Component Coupling Reaction of Aldehydes, Amines, and Alkynes. *Angew. Chem.* **2001**, *113*, 2602-2604.

(44) Fischer, C.; Carreira, E. M. Direct addition of TMS-acetylene to aldimines catalyzed by a simple, commercially available Ir(I) complex. *Org. Lett.* **2001**, *3*, 4319-4321.

(45) Li, C.-J.; Wei, C. Highly efficient Grignard-type imine additions via C–H activation in water and under solvent-free conditions. *Chem. Commun.* **2002**, 268-269.

(46) Wei, C.; Li, C.-J. Enantioselective Direct-Addition of Terminal Alkynes to Imines Catalyzed by Copper(I)pybox Complex in Water and in Toluene. *J. Am. Chem. Soc.* **2002**, *124*, 5638-5639.

(47) Lee, J.; Farha, O. K.; Roberts, J.; Scheidt, K. A.; Nguyen, S. T.; Hupp, J. T. Metal-organic framework materials as catalysts. *Chem. Soc. Rev.* **2009**, *38*, 1450-1459.

(48) Chughtai, A. H.; Ahmad, N.; Younus, H. A.; Laypkov, A.; Verpoort, F. Metal-organic frameworks: versatile heterogeneous catalysts for efficient catalytic organic transformations. *Chem. Soc. Rev.* **2015**, *44*, 6804-6849.

(49) Zhao, M.; Ou, S.; Wu, C.-D. Porous Metal–Organic Frameworks for Heterogeneous Biomimetic Catalysis. *Acc. Chem. Res.* **2014**, *47*, 1199-1207.

(50) Corma, A.; García, H.; Llabrés i Xamena, F. X. Engineering Metal Organic Frameworks for Heterogeneous Catalysis. *Chem. Rev.* **2010**, *110*, 4606-4655.

(51) Zhang, T.; Manna, K.; Lin, W. Metal–Organic Frameworks Stabilize Solution-Inaccessible Cobalt Catalysts for Highly Efficient Broad-Scope Organic Transformations. *J. Am. Chem. Soc.* **2016**, *138*, 3241-3249.

(52) Falkowski, J. M.; Sawano, T.; Zhang, T.; Tsun, G.; Chen, Y.; Lockard, J. V.; Lin, W. Privileged Phosphine-Based Metal–Organic Frameworks for Broad-Scope Asymmetric Catalysis. *J. Am. Chem. Soc.* **2014**, *136*, 5213-5216.

(53) Yoon, M.; Srirambalaji, R.; Kim, K. Homochiral Metal–Organic Frameworks for Asymmetric Heterogeneous Catalysis. *Chem. Rev.* **2012**, *112*, 1196-1231.

(54) Wu, C.-D.; Hu, A.; Zhang, L.; Lin, W. A homochiral porous metal− organic framework for highly enantioselective heterogeneous asymmetric catalysis. *J. Am. Chem. Soc.* **2005**, *127,* 8940-8941.

(55) Ma, L.; Abney, C.; Lin, W. Enantioselective catalysis with homochiral metal–organic frameworks. *Chem. Soc. Rev.* **2009**, *38*, 1248-1256.

(56) Ma, L.; Falkowski, J. M.; Abney, C.; Lin, W. A series of isoreticular chiral metal–organic frameworks as a tunable platform for asymmetric catalysis. *Nat. chem.* **2010**, *2*, 838.

(57) Liu, Y.; Xuan, W.; Cui, Y. Engineering homochiral metal-organic frameworks for heterogeneous asymmetric catalysis and enantioselective separation. *Adv. Mater.* **2010**, *22,* 4112-4135.

(58) Dang, D.; Wu, P.; He, C.; Xie, Z.; Duan, C. Homochiral metal− organic frameworks for heterogeneous asymmetric catalysis. *J. Am. Chem. Soc.* **2010**, *132,* 14321-14323.

(59) Peng, Y.; Gong, T.; Zhang, K.; Lin, X.; Liu, Y.; Jiang, J.; Cui, Y. Engineering chiral porous metal-organic frameworks for enantioselective adsorption and separation. *Nat. commun.* **2014**, *5*, 4406.

(60) Tanaka, K.; Oda, S.; Shiro, M. A novel chiral porous metal-organic framework: asymmetric ring opening reaction of epoxide with amine in the chiral open space. *Chem. Commun.* **2008**, 820-822.

(61) Tanaka, K.; Otani, K.-i. Asymmetric alcoholytic kinetic resolution of styrene oxide catalysed by chiral metal-organic framework crystals. *New J. Chem.* **2010**, *34*, 2389-2391.

(62) Mo, K.; Yang, Y.; Cui, Y. A Homochiral Metal–Organic Framework as an Effective Asymmetric Catalyst for Cyanohydrin Synthesis. *J. Am. Chem. Soc.* **2014**, *136*, 1746-1749.

(63) Shi, W.; Cao, L.; Zhang, H.; Zhou, X.; An, B.; Lin, Z.; Dai, R.; Li, J.; Wang, C.; Lin, W. Surface Modification of Two-Dimensional Metal–Organic Layers Creates Biomimetic Catalytic Microenvironments for Selective Oxidation. *Angew. Chem. Int. Ed.* **2017**, *56*, 9704-9709.

(64) Wang, C.; Zheng, M.; Lin, W. Asymmetric Catalysis with Chiral Porous Metal–Organic Frameworks: Critical Issues. *J. Phys. Chem. Lett.* **2011**, *2*, 1701-1709.

(65) Wang, C.; deKrafft, K. E.; Lin, W. Pt Nanoparticles@Photoactive Metal–Organic Frameworks: Efficient Hydrogen Evolution via Synergistic Photoexcitation and Electron Injection. *J. Am. Chem. Soc.* **2012**, *134*, 7211-7214.

(66) Thacker, N. C.; Lin, Z.; Zhang, T.; Gilhula, J. C.; Abney, C. W.; Lin, W. Robust and Porous β-Diketiminate-Functionalized Metal–Organic Frameworks for Earth-Abundant-Metal-Catalyzed C–H Amination and Hydrogenation. *J. Am. Chem. Soc.* **2016**, *138*, 3501-3509.

(67) Xu, R.; Wang, Y.; Duan, X.; Lu, K.; Micheroni, D.; Hu, A.; Lin, W. Nanoscale Metal–Organic Frameworks for Ratiometric Oxygen Sensing in Live Cells. *J. Am. Chem. Soc.* **2016**, *138*, 2158-2161.

(68) Cao, L.; Lin, Z.; Peng, F.; Wang, W.; Huang, R.; Wang, C.; Yan, J.; Liang, J.; Zhang, Z.; Zhang, T.; Long, L.; Sun, J.; Lin, W. Self-Supporting Metal–Organic Layers as Single-Site Solid Catalysts. *Angew. Chem. Int. Ed.* **2016**, *128*, 5046-5050.

(69) Zhang, Q.; Su, J.; Feng, D.; Wei, Z.; Zou, X.; Zhou, H.-C. Piezofluorochromic Metal–Organic Framework: A Microscissor Lift. *J. Am. Chem. Soc.* **2015**, *137*, 10064-10067.

(70) Li, J. J. *Name reactions: a collection of detailed mechanisms and synthetic applications*; Springer Science & Business Media, 2010.

(71) Syeda Huma, H. Z.; Halder, R.; Singh Kalra, S.; Das, J.; Iqbal, J. Cu(I)-catalyzed three component coupling protocol for the synthesis of quinoline derivatives. *Tetrahedron Lett.* **2002**, *43*, 6485-6488.

(72) Choi, Y. J.; Jang, H. Y. Copper-Catalyzed A^3-Coupling: Synthesis of 3-Amino-1,4-diynes. *Eur. J. Org. Chem.* **2016**, *2016*, 3047-3050.